



**University of  
Nottingham**

UK | CHINA | MALAYSIA

**Master Thesis 2023-2024**

**Substrate design and aluminium droplet  
morphology study of a new 3D printing  
technique**

Student: Wang Yidong

Student ID: 20513634

Lead supervisor: Adam Rushworth

Second supervisor: Hao Chen

Third supervisor: Guang Li

Fourth supervisor: Yi Nie

## **Acknowledgements**

The author would like to thank the lead supervisor, Dr Adam Rushworth, for his advice about the project and his suggestions for this thesis. The author would like to thank other supervisors, Dr Hao Chen, Dr Guang Li, and Dr Yi Nie, for their ideas for the project. The author is grateful to Master Ricardo Castro for his help with the printhead set and the guide of droplet production parameters. The material preparation and equipment buying is supported by the technician John Zhu and the University of Nottingham Ningbo, China.

# Abstract

In recent years, additive manufacturing (AM) techniques have been developed quickly, attracting industry and home user attention. The AM market also expands and creates much economic effectiveness. To avoid the drawbacks of common technologies (high cost and dangerous work environment) and allow home users to print metal products, a new technique named Metal Droplet Extrusion (MDE) was developed at the University of Nottingham Ningbo China (UNNC) and supervised by Dr Adam Rushworth. For this technique, the previous researchers have successfully designed a print head and produced the controllable aluminium 6061 alloy droplets in the water base. However, a substrate system, generally made by a heater, a plate and a support structure that allows the droplets to stay and remelt to form an object, is required to provide a complete printer prototype and study the droplet impact behaviour. When droplets impact the substrate, they will have different morphology of the final product because of the distance, temperature and roughness; the final product morphology will affect the further remelting of the droplets and, hence, influence the final surface quality and structure strength of the printed products.

To design the substrate system and have a good understanding of the droplets' impact behaviour on the solid surface, this thesis will finish 2 main objectives – substrate system and prototype design, and the experiments about four parameters that affect the droplet contact angle.

At first, 8 requirements of designing a substrate system have been outputted based on the previous literature review and the recent equipment in the lab. The whole design of the substrate system has been developed and changed 3 times in digital software. Different substrate plate materials or material sets have been tested by conducting high-temperature experiments to

reach the maximum temperature requirement. After the substrate was manufactured and the feasibility tested, a printer prototype was assembled for further behaviour study. The prototype has also been tested for the possibility of printing simple one-layer and multiple-layer products. As for the droplet behaviour study, three factors that will affect the impact behaviour of droplets were examined by conducting different experiments, including different distances between the nozzle and plate, different substrate surface temperatures and surface roughness. After the experiments have been done, the pictures of the droplets will be taken and calibrated in the MATLAB program. Then, the contact angles of droplets will be measured by a software called camera measure. The contact angle results will be analysed to show how these factors affect the contact angle of the droplets and determine the best material for the substrate plate for the technique.

According to all experiments in this thesis, 95 aluminium oxide ceramics with a Mika cover to help accumulate heat are the best materials for the future study of this technique. This set of materials produces the highest temperature in the substrate system temperature experiments (532.4°C). It can produce 90° contact angle droplets with 165°C with a roughness of 1.241µm and 1µm of the roughness when the temperature is room temperature. 304 stainless steel cannot provide 90° contact angle droplets; all the droplets' contact angles were larger than 120°. As for the copper plate, 150 degrees of plate temperature and 1.8µm surface roughness will bring 90° of the droplet's contact angle. Meanwhile, the rise in distance between the nozzle and the substrate surface will cause more splashed droplets. The contact angle of impacting droplets will increase with the increase of the surface roughness but decrease with the rise of the surface temperature.

# Table of Contents

Acknowledgements.....	i
Abstract.....	ii
Table of Contents.....	iv
Table of Tables .....	vii
Table of Figures .....	viii
Abbreviations.....	xiii
Chapter 1 Introduction.....	1
1.1. Background.....	1
1.2. Introduction of the Project .....	3
1.3. Aim and Objectives .....	4
1.3.1. Aim .....	4
1.3.2. Objectives .....	4
1.3.3. Proposed Deliverables/Outcomes for the Project.....	4
Chapter 2 Literature Review .....	5
2.1. Introduction.....	5
2.2. Additive Manufacture (3D printing technique) .....	5
2.2.1. Material Jetting .....	8
2.2.2. Different methods of Metal material jetting .....	13
2.3. The substrate system selection of the metal 3D printing.....	21
2.3.1. Introduction.....	21

2.3.2. The Classification of the Substrate System in the Articles	22
2.4. Droplet Morphology Consideration	33
2.4.1. Introduction	33
2.4.2. The Impact of the Droplet	33
2.4.3. Splash Shape	42
2.4.4. Sphere-like Shape	48
2.5. Conclusion	55
Chapter 3 Methodology	56
3.1. Substrate System Design Development and Testing	56
3.1.1. Introduction	56
3.1.2. Requirements	57
3.1.3. Substrate Design Development	59
3.2. Whole Prototype Design	69
3.3. Calculations and Predictions of the Experiments	74
3.4. Experiment arrangement	79
3.4.1. Introduction	79
3.4.2. Material Preparation	79
3.4.3. Equipment Preparation	83
3.4.4. Experiment Plan	85
Chapter 4 Results and Analysis	91
4.1. Substrate temperature experiment	91

4.1.1. Substrate System Test and System Adjustment .....	91
4.1.2. Comparison of different substrate materials.....	102
4.1.3. Conclusion of the substrate system.....	106
4.2. Distance Experiment.....	106
4.3. Temperature Experiment .....	110
4.4. Roughness Experiment .....	113
4.5. Conclusion .....	117
Chapter 5 Conclusion .....	118
5.1. Conclusion .....	118
5.2. Future Expectations .....	119
Chapter 6 References.....	120
Chapter 7 Appendix.....	143

# Table of Tables

Table 1: Introduction and commonly used material of 7 different groups of additive manufacture .....	7
Table 2: Data collection from 35 articles .....	23
Table 3: The data collection of substrate surface roughness and the distance between the nozzle and the substrate.....	27
Table 4: Outcomes of the droplet impact process [111], [112] .....	44
Table 5: Description and definition of different contact angles [125], [126], [127].....	49
Table 6: Design requirements and the descriptions.....	58
Table 7: Wire movement, theoretical sphere volume, theoretical sphere radius and the initial nozzle velocity based on steps .....	76
Table 8: Different types of material plate preparation.....	80
Table 9: Detailed elements of the material .....	81
Table 10: Surface roughness of the sample plates with different post-processing methods and materials .....	83
Table 11: The table of the status and the details about the achieved requirement.....	106
Table 12: Surface roughness, the measured contact angle and the roughness factor r.....	116

## Table of Figures

Figure 1: Classification of the material jetting [32].....	9
Figure 2: Schematic diagram of (a) continuous jet print, (b) thermal inkjet nozzle for DoD, and (c) a piezoelectric inkjet nozzle for DoD from Ansell et al. [37] .....	10
Figure 3:Schematic diagram of Pneumatic jetting from [32] .....	11
Figure 4: Schematic diagram of Magneto hydrodynamic Jetting technique from [32].....	12
Figure 5:Schematic diagram of Push-mode jetting technique from [37] .	13
Figure 6: The diagram of the Patent from Gottwald [40].....	14
Figure 7: Schematic diagram of three different types of Piezoelectric Drop-on-Demand Printing techniques from Ansell et al. [37].....	16
Figure 8: Schematic diagram of Electrohydrodynamic (EHD) printing technique from Ansell et al. [37]. .....	17
Figure 9: Schematic diagram of Magneto hydrodynamic (MHD) printing technique from Ansell et al. [37]. .....	17
Figure 10: Schematic diagram of low-temperature Pneumatic Drop-on-Demand printing technique from Ansell et al. [37].....	18
Figure 11: Figures about the StarJet technique from Ansell et al. [37]: (a) Diagram of the StarJet printhead and (b) an SEM micrograph of the nozzle .....	19
Figure 12: Schematic diagram of Impact-Driven Drop-on-Demand printing technique from Ansell et al. [37]. .....	20
Figure 13: Schematic diagram of Laser-assisted Forward Transfer (LIFT)	

technique from Ansell et al. [37].	21
Figure 14: Classification of the droplet materials in Articles	29
Figure 15: Classification of the substrate materials in Articles	29
Figure 16: Schematic droplet generator from Mehdizadeh et al. [102]	34
Figure 17: Impacting stage [90]	35
Figure 18: Spreading stage [90]	35
Figure 19: Rebounding and equilibrium stage [90]	35
Figure 20: Heat transferring and solidifying stage [90]	36
Figure 21: Two types of droplets from Yang et al. [103]	36
Figure 22: Computer-generated images compared with photographs of a 2mm diameter water droplet impacting a stainless steel surface with a velocity of 1 m/s from Pasandideh-Fard et al. [92].	38
Figure 23: Schematic diagram of the collision behaviour of aluminium droplets covered with an oxide layer in an air environment from Yang et al. [103].	41
Figure 24: Schematic view of splash droplet from Mundo et al. [94].	42
Figure 25: The graph of the comparison of measured and calculated contact angles affected by temperature from Bao et al. [129]	51
Figure 26: (a) Wenzel model and (b) Cassie model [124]	53
Figure 27: Explosion view of the original design	59
Figure 28: Final version of the substrate system without the PID controller .....	61
Figure 29: Explosion view of Heater part	62

Figure 30: Assembly view of the plate support .....	63
Figure 31: Explosion view of the plate support.....	64
Figure 32: Assembly view of the heater support .....	65
Figure 33: Explosion view of the heater support.....	65
Figure 34: Assembly view of the cooling part.....	66
Figure 35: Explosion view of the cooling part .....	66
Figure 36: Manufactured and assembled substrate system with 4mm stainless steel plate and waiting for temperature testing .....	68
Figure 37: Schematic of the whole prototype system.....	70
Figure 38: Manufactured prototype .....	71
Figure 39: Connection of all equipment of the prototype.....	72
Figure 40: Printed products with the mica ceramic substrate system.....	73
Figure 41: Prediction of the K parameter changed by droplet sizes, the distance and the droplet temperature .....	78
Figure 42: Sample copper and stainless steel plates with different surface roughness .....	82
Figure 43: Flow chart of the experiment .....	86
Figure 44: The experiment set and results graph of the T2 copper plate temperature test.....	93
Figure 45: The experiment set and results graph of the 304 stainless steel plate temperature test.....	94
Figure 46: The experiment set and results graph of the 95 Aluminium oxide ceramic plate temperature test .....	95

Figure 47: The experiment set and results graph of the pieced ceramic temperature test.....	97
Figure 48: The experiment set and results graph of the pieced ceramic and cooper in the middle-temperature test .....	98
Figure 49: The experiment set and results graph of the Ceramic and manufactured copper plate temperature test.....	100
Figure 50: The experiment set and results graph of the Mica cover with ceramic plate temperature test .....	101
Figure 51: The experiment set of four materials for the comparison experiments: A) The big copper plate set; B) The big stainless steel plate set; C) The ceramic plate with manufactured copper; D) The ceramic plate with Mika cover .....	103
Figure 52: The heater temperature of different material experiments....	104
Figure 53: The plate centre temperature of different material experiments. ....	104
Figure 54: The temperature graph of the Ceramic-Mika plate without PID control.....	105
Figure 55: Splash droplet number and sphere-like droplet percentage change with the increase in the distance.....	108
Figure 56: Average contact angles of the droplets on all three materials change with increasing substrate plate temperature lower than 160 degrees with photos of droplets .....	110
Figure 57: Average contact angle of droplets on ceramic changes by the increasing substrate surface temperature until 313.3 degrees with the photos of the droplets.....	111

Figure 58: Average contact angles of the droplets on stainless steel and copper plates change by different surface roughness ..... 114

Figure 59: Average contact angles of droplets on a ceramic plate change by different surface roughness..... 114

## Abbreviations

AM	Additive manufacture
MDE	Metal droplet deposition
UNNC	University of Nottingham Ningbo China
CAD	Computer-Aided Design
3D	3 dimensional
DoD	Droplet on demand
EU	European Union
DoDjet	Drop-on-demand jetting
EHD	Electrohydrodynamic
PZT	Lead zirconate titanate
LIFT	Laser-assisted forward transfer
PDM	precision droplet-based net-form manufacturing
DTm	The decreasing trend model
UTm	The Unsymmetrical trend model
CNC	Computerised Numerical Control
PID	Proportion Integration Differentiation
NI	National Instruments

# Chapter 1 Introduction

## 1.1. Background

In recent years, additive manufacturing (AM) techniques have developed at a quick speed since they were used in the 1980s [1]. In 2011, a revenue estimated at \$642.6 million was recorded for global additive manufactured goods [2]. The researchers also predicted the industry would expand to \$100 billion between 2031 and 2044 [3]. AM is also regarded as a cornerstone of realising Industry 4.0 [3]. Industry 4.0, which is called the fourth industrial revolution, is a new paradigm of smart and autonomous manufacturing that combines manufacturing operations systems with communication, information, and intelligence technologies [4]. Europe created 1.6 million jobs, which accounts for 11% of total EU manufacturing production (30 million) [3]. Meanwhile, based on the development of different types of AM techniques, additive manufacturing has been used in a wide range of fields, including the automotive [5], aerospace [6], biomedical [7], pharmaceutical [8], sports [9] and construction [10]. Compared to traditional manufacturing (subtractive manufacturing), AM has these advantages:

- 1) High design ability: The complex structure design for customer requirements, which is hard for traditional manufacturing, can be achieved by AM techniques [11], [12], [13], [14].
- 2) Reduced waste: AM only uses the precise amount of material needed to produce a product [11], [12], [13].
- 3) Improved resource efficiency: The adjustments and improvements can be easily accomplished during the manufacturing and use phase, and products can be redesigned for AM techniques [11], [12], [13],

[15].

- 4) Reconfigured value chains: AM can shorten the supply chain, reduce the inventory, and decentralise manufacturing for localised production, which decreases the cost [14], [15], [16].

These advantages mean that AM technology allows people to produce products with low production volumes, high design complexity, and frequent design changes required at a relatively low price and with high efficiency compared to traditional manufacturing (subtractive manufacturing) [17]. This attracts both industry and home users. However, there are limitations to the AM techniques:

1. Material Limitations: Different parameters of materials need to be optimised for different types of AM techniques [14], [18], [19]
2. Technological Feasibility Limitations: New skills in designing and engineering are required for the AM techniques [15], [20]
3. Volume production: AM is less cost-effective and efficient for the mass production of simple parts compared to traditional manufacturing [11], [18]

Especially for metal 3D printing techniques, the danger and post-processing of the raw material, the high energy consumption and the high cost of the machine are apparent problems in the recent commercial metal 3D printing techniques [21]. It is challenging to transform metal into a powder state, and metal powder is dangerous because it may cause lung sicknesses, such as pneumoconiosis or pneumonia after humans breathe it during work. Also, it will easily cause a big explosion if it is not stored well. Because this technique uses a laser beam, the relatively high energy consumption will be 14.5 kWh/kg, which is equal to 52.2 kJ/kg [22].

## 1.2. Introduction of the Project

A new technique, called Metal Droplet Extrusion (MDE), has been developed at the University of Nottingham Ningbo, China, supervised by Dr Adam Rushworth, since 2017. This technique uses an induction heater to melt metal filaments to create metal droplets to form the product. The prototype has the following advantages:

1. High achievable temperatures higher than 1600 degrees
2. Low-cost feedstock
3. Safe feedstock material for handling
4. Ability to selectively control droplet size during the printing process
5. Applicable to a wide variety of materials

A prototype printhead without the heating substrate system has been assembled and tested for its feasibility. The minimum size of 0.5 $\mu$ m diameter droplets could be produced, and the parameter of the 1mm diameter size droplet for continuous printing has been created and verified. However, this prototype uses a special type of substrate to catch the sample droplets, which can only catch single droplets rather than being able to combine the droplets to create a completely printed sample. Hence, a substrate system is required to allow the droplets to solidify on it and remelt together to create the final product. Meanwhile, the substrate system should be able to heat the substrate plate to facilitate the remelting of the droplets. The control of the temperature of the substrate plate is also needed for further study of the morphology and the remelting of the droplets. Besides, the substrate system should be suitable for the existing 3D moving platform and can move 150mm in the XY-axis and 60mm in the Z-axis.

## **1.3. Aim and Objectives**

### **1.3.1. Aim**

To better understand the behaviour of the droplets impacting the substrate.

### **1.3.2. Objectives**

- 1) Research other substrate systems used in metal 3D printers and find the relationship between different factors and the behaviour of the impact droplets.
- 2) Design and manufacture a substrate system with controlled heating and prepare substrates made of different materials with different roughness.
- 3) Measure and compare the contact angles of droplets on the manufactured substrate system with different types of plate materials, different plate surface roughness and different plate surface temperatures.

### **1.3.3. Proposed Deliverables/Outcomes for the Project**

- 1) A better understanding of the relationship between droplets and the substrate system.
- 2) Manufactured and tested the substrate system.
- 3) A more comprehensive understanding of droplet's behaviour at different temperatures, substrate material, and surface roughness for further product printing.

# Chapter 2 Literature Review

## 2.1. Introduction

This literature review will first go through the additive manufacture and different printing types of additive manufacture. The following section will explain what material jetting is and show how material jetting will work. Then, the metal material jetting will be discussed briefly, and the different printing types of material jetting will be introduced.

After introducing additive manufacturing and metal 3D printing, this section will briefly review the vital information about substrate system design in 35 different papers. It will also explain the consideration of the chosen substrate material. Finally, the first consideration of the design of the substrate system will be briefly indicated at the end of the section.

The droplet morphology follows the substrate-chosen section, which introduces the droplet impact and discusses the final shape of the droplet absorbed by the substrate (splash or sphere-like shape). This part also gives the equations of dynamic analysis and shape prediction and discusses the factors that affect the impact process, the splash, and the contact angle.

## 2.2. Additive Manufacture (3D printing technique)

The additive manufacturing technique is defined by Gupta et al. [23] as the production technology that produces the 3D product in solidification by either solid or liquid starting material and is controlled by an automated computer program.

Compared to traditional subtractive manufacturing, which is defined as

the reduction of a block of material to the required shape and size, it has some advantages [24]: increasing in part complexity, virtual design and manufacture, free manufacture (no need for particular designed mould or tools), instant global production (world-wide and instant producing by ready-designed model) and reducing in material waste.

However, additive manufacturing still has disadvantages based on technology limitations [25], [26]: unstable mechanical property prediction (based on the print method and orientation), unequal accuracy (impacted by material, post-processing and CAD software) and limitations in size as well as material.

Shahrubudin et al. [27] mentioned that additive manufacturing could be divided into seven major groups based on their printing methodology: binder jetting, directed energy deposition, material extrusion, material jetting, powder bed fusion, sheet lamination and vat photo-polymerisation. Table 1: Introduction and commonly used material of 7 different groups of additive manufacture below shows the simple work process and widely used material.

Table 1: Introduction and commonly used material of 7 different groups of additive  
manufacture

	Process	Material
Binder jetting	A liquid bonding agent is selectively deposited	Metals, sands, polymers, hybrid and ceramics
Directed energy deposition	Focused thermal energy is used to fuse materials by melting as the material is deposited.	Metals and metal-based hybrids, ceramics and polymers
Material extrusion	A material is selectively dispensed through a nozzle or orifice	Plastics, food or living cells
Material jetting	Droplets of build material are selectively deposited	Polymers, ceramics, composites, biologicals and hybrid
Powder bed fusion	Thermal energy selectively fuses regions of a powder bed	Metals, ceramics, polymers, composite and hybrid
Sheet lamination	Sheets of material are bonded to form an object	Metals, papers and plastics
Vat photo-polymerisation	Liquid photopolymer in a vat is selectively cured by light-activate polymerisation.	Light-curable resins

The material is the key to achieving the full function of a product [19]. Based on material, a suitable additive manufacturing method could print complex geometrical and architectural designs that are difficult or impossible to produce in conventional manufacturing. Because of metal's excellent physical properties and ability to be a complex manufacturer, Metal 3D printing has absorbed attention in a wide area, from human organs to aircraft [28]. For example, titanium alloys produce aerospace components using powder bed fusion and biomedical components using powder bed fusion or directed energy deposition [29].

The following section will introduce details about material jetting based on the development of this technique.

### 2.2.1. Material Jetting

Silva et al. [30] state that material jetting is one of the oldest additive manufacturing technologies because it is derived from the typewriter's inkjet printing, invented in the 1950s. However, inkjet printing has become popular in families or offices since the 1980s because leading manufacturing companies like Hewlett-Packard (HP) developed desktop inkjet printers, which cause less noise and power consumption [30]. The new printer is actuated by micro-electro-mechanical actuators, which are non-impact and have digital control.

Material jetting is a process of generating and solidifying droplets layer by layer. Liquid materials like photopolymers, metals, or wax will first be collected in a chamber [31]. Then, it is jetted by tiny nozzles, which control the volume, velocity, and frequency and turn them into desired coordinates on the build platform. At the same time, the droplet will be solidified to form a part layer when exposed to light or heat, such as stereolithography [32].

This technique has several advantages: high resolution, dimensional and geometric rigour, multi-material enabling, and high printing speed [33]. Because the diameters of nozzles are typically less than 100 $\mu$ m. And there are many nozzles in one printing head [30]. Each printer has several print heads which can contain different materials; the machine Connex Objet500™ (Stratasys, Minneapolis, MN, USA) has eight printheads and can print three materials: four heads dedicated to the support material, the other four allowing the use of two different construction materials.

Although material jetting has benefits, it still has some drawbacks: poor mechanical properties, material limitations and high cost. Tray location, post-processing, material type, layer thickness, surface finish, and build orientation affect the final part's mechanical properties and the material, like

photopolymers, which will lose their strength over time [34]. Photopolymers, casting wax, and several types of metals are used in jetting materials. The 3D printer for material jetting requires a high price. For example, a ProJet MJP 5600 from 3D Systems would cost over \$100,000 [35], which is nearly thirty times more expensive than the basic Bambu Lab A1 mini 3D Printer with the printing filaments, which is only \$329 [36].

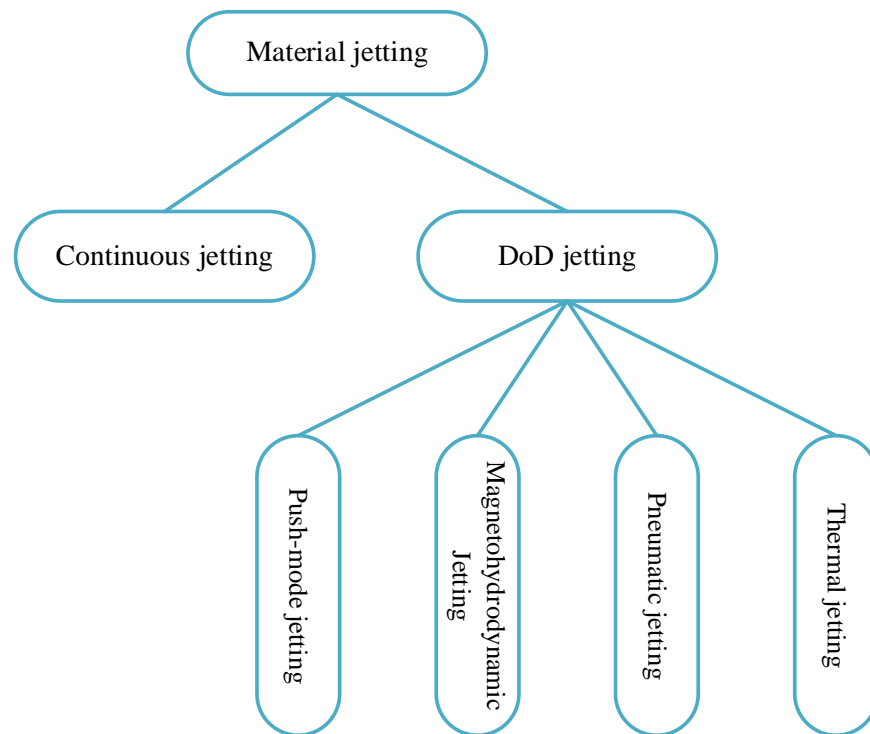


Figure 1: Classification of the material jetting [32]

As shown in Figure 1, there are two main types of material jetting: continuous jetting and drop-on-demand jetting (DoDjet). For continuous jetting, ink is divided into drops via an ultrasonic generator and charged by the electrodes. Then, it will be deflected electrostatically by high-voltage deflection plates to the desired position (Figure 2 (a)). However, as the name

means, ink is ejected only when needed in DoDjet (Figure 2 (b) and (c)) [37].

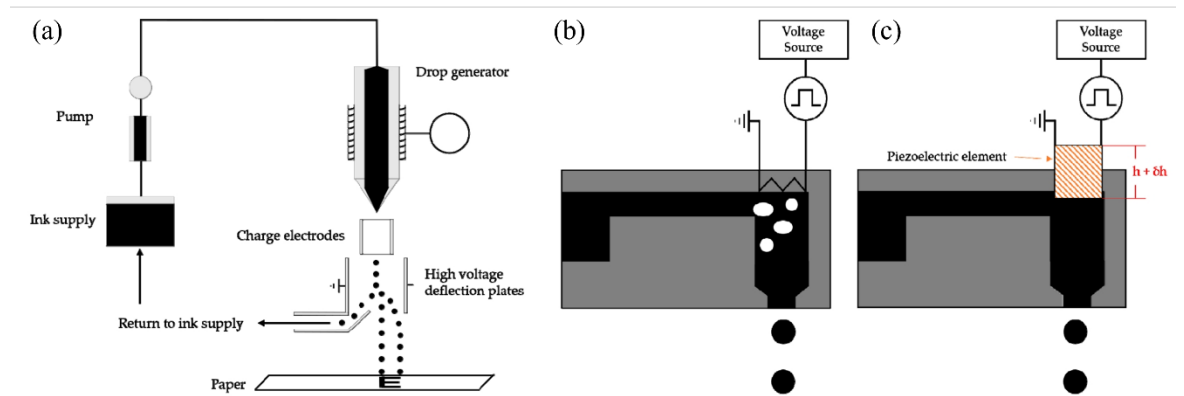


Figure 2: Schematic diagram of (a) continuous jet print, (b) thermal inkjet nozzle for DoD, and (c) a piezoelectric inkjet nozzle for DoD from Ansell et al. [37]

Compared to the two types of material jetting, DoD is more realistic than continuous jetting when used in real life, according to Korkut and Yavuz [32]. Droplets in DoD can be controlled in size, velocity and other crucial droplet parameters, which allows homogeneity between all droplets, resulting in more consistent deposition characteristics. However, in continuous jetting, droplets are ejected with high frequency and solidify quickly to form the part consisting of partially combined but heterogeneous droplets [32].

The following explains the detailed mechanisms of four different common types of DoD jet technologies.

1. Thermal jetting (Figure 2 (c)) uses resistive wire (heat up) or a couple of probes (electrical spark generation) to heat the liquid material locally to vaporise to create a gas bubble inside the material reservoir. Then, the bubble will push the same volume of material out of the nozzle. Its limitations include precise control of electrical inputs, change of liquid chemical composition and unequal volume of ejected bubbles [32], [38].

2. Pneumatic jetting (Figure 3) generates droplets by pushing liquid out of the orifice with precisely controlled pneumatic pressure. However, the pressure level may fluctuate because of the compressibility of the gas. Also, it has a low ejection frequency, which means it has a low printing speed [32], [39].

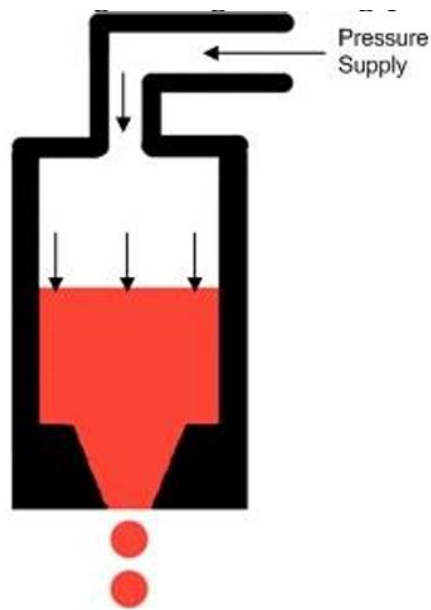


Figure 3: Schematic diagram of Pneumatic jetting from [32]

3. Magnetohydrodynamic Jetting (Figure 4) uses Lorentz force generated from conductive material in the electric and magnetic fields to drive droplets without direct contact. It can use high melting point metals. Nevertheless, the available metal is limited, and the correct magnetic and electric field position is required. At the same time, this type of printer will cost high energy and intensive simulation [32].

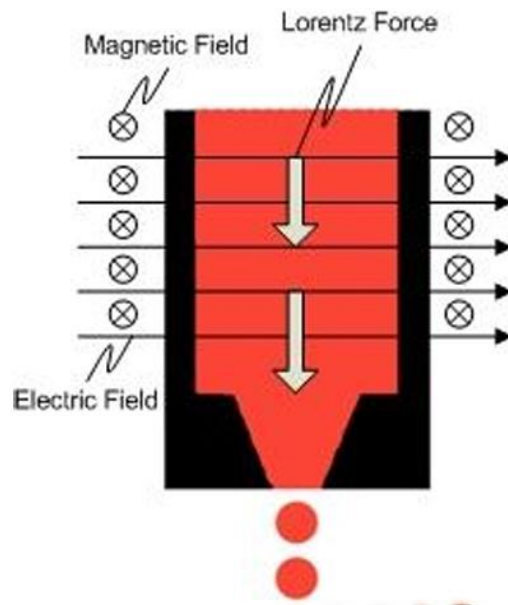


Figure 4: Schematic diagram of Magnetohydrodynamic Jetting technique from [32]

4. Push-mode jetting (Figure 5) squeezes the liquid by an actuator that can move in a certain displacement. Two primary actuators will be selected: piezoelectric transducers and solenoid coils. Compared to other mechanisms, it can provide high depositing rates and the final product's high resolution and surface quality. However, all mechanical system parts should be micro-manufactured precisely, and the operation temperature is relatively low at the current technical level [32].

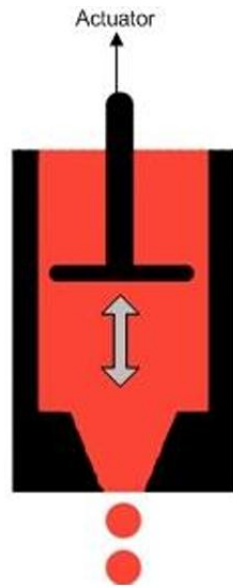


Figure 5: Schematic diagram of Push-mode jetting technique from [37]

Although material jetting started in the early 20th century, the metal materials used have changed in more recent times. The metal material jetting technique will be discussed in the following section.

### **2.2.2. Different methods of Metal material jetting**

Continuous jetting and droplet-on-demand material jets can be used to print metal objects [37].

The history of material jetting in metal additive manufacturing may have come out in 1969. Gottwald [40] of the Teletype Corporation has demonstrated the freeform fabrication of a three-dimensional metal object by a material jetting process (Figure 6). With a low melting point, the molten metal stream was squeezed out and deflected by two magnetic fields (one was from the nozzle, the other was from an outside circuit through the path), then generated to build a metal object [40].

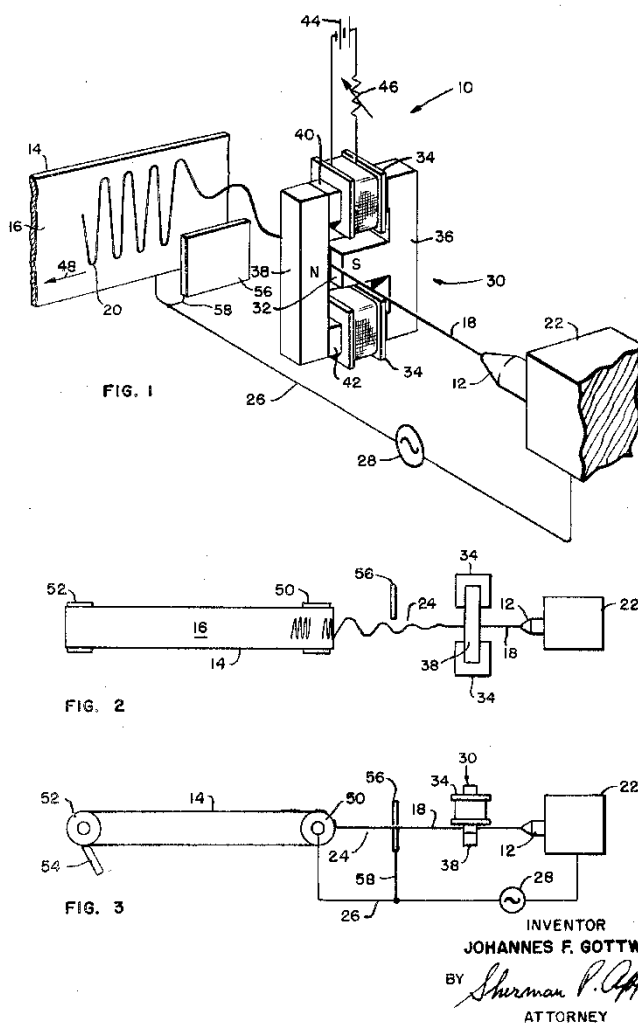


Figure 6: The diagram of the Patent from Gottwald [40]

Then, liquid metal freeform printing is developed by the progress of low-temperature solder. Hieber [41] published a patent in 1989 describing a method of jetting molten solder with a piezoelectric inkjet system. A piezoelectric transducer is used as a pressure generator to squeeze droplets from a delivery nozzle and drop them onto the wet area [41].

According to Ansell et al. [37], the first-time a near-net free-standing form Al object (or any other metal/alloy) was printed via the continuous

material jetting method was in 1999 when Orme and Smith [42] researched a method to jet molten aluminium (Al) into free-standing structures by continuous inkjet. Pure tin (Sn), a zinc-tin alloy and a tin-lead alloy were studied by Kim et al. [43] to develop a control methodology to control the droplet size by adjusting vibration frequency for stream break-up. Jiang et al. [44] researched the CIJ printer and found that droplets need higher gas backpressure and will be more challenging to break up in frequency from the jet stream when going through a smaller nozzle.

Piezoelectric Drop-on-Demand Printing has three different printing modes (Figure 7): squeeze mode, bending mode and push mode [37]. Marusak [45] on Indalloy-58 investigated a squeeze-mode for jetting low-temperature Indalloy-58. The material was filled in the chamber covered by piezoelectric crystal and squeezed out by the deformation of the piezoelectric crystal when a voltage. Squeeze mode could print higher temperatures (about 600°C) of molten metal with the cost of a specially designed glass tube. The bending mode has been developed for metallic inks and low-temperature molten metal. Push mode is a more commonly used one that can print the material under 400°C.

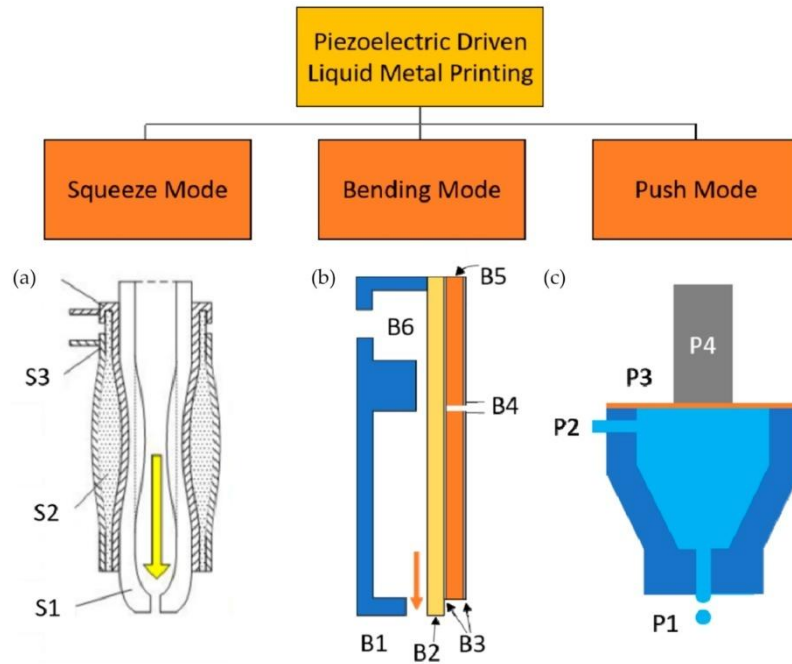


Figure 7: Schematic diagram of three different types of Piezoelectric Drop-on-Demand Printing techniques from Ansell et al. [37].

Field-Induced Drop-on-Demand Printing is based on applying a field to eject material [37]. Electrohydrodynamic (EHD) printing (Figure 8) works by adding a strong enough electric field to break the surface tension in the fluid to form a droplet [37]. EHD has an advantage in high resolution and is commonly printed in polymeric materials, biomaterials or metal nanoparticles. Magnetohydrodynamic (MHD) printing (Figure 9) uses a magnetic field-induced pressure gradient to jet liquid metal droplets. It has two printer systems divided by the difference in substrate: the MetalJet system [46] and MagnetoJet™ Systems [47]. Electromagnetic DOD Printing developed by Luo et al. [48] combines both fields to induce jet droplets. And the droplet diameter changes with nozzle diameter, pulse width, and magnetic field intensity.

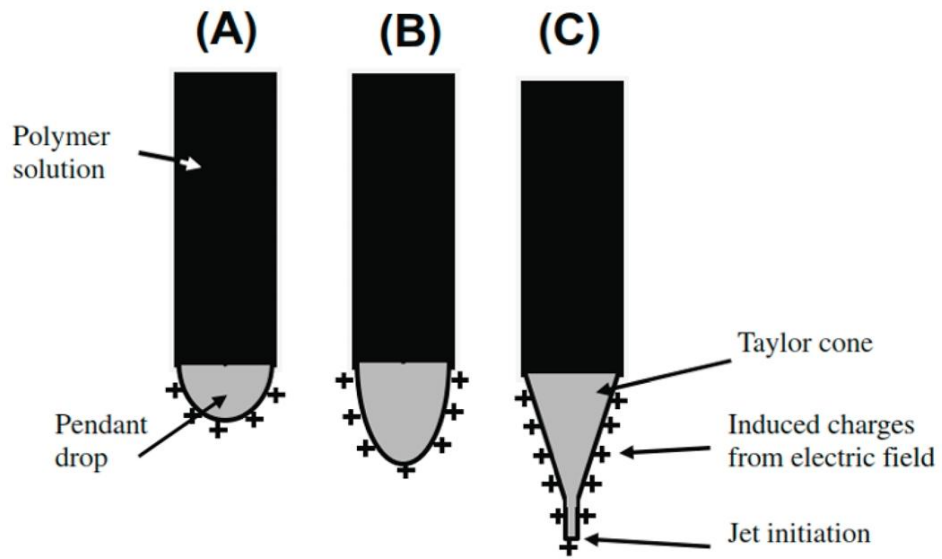


Figure 8: Schematic diagram of Electrohydrodynamic (EHD) printing technique from Ansell et al. [37].

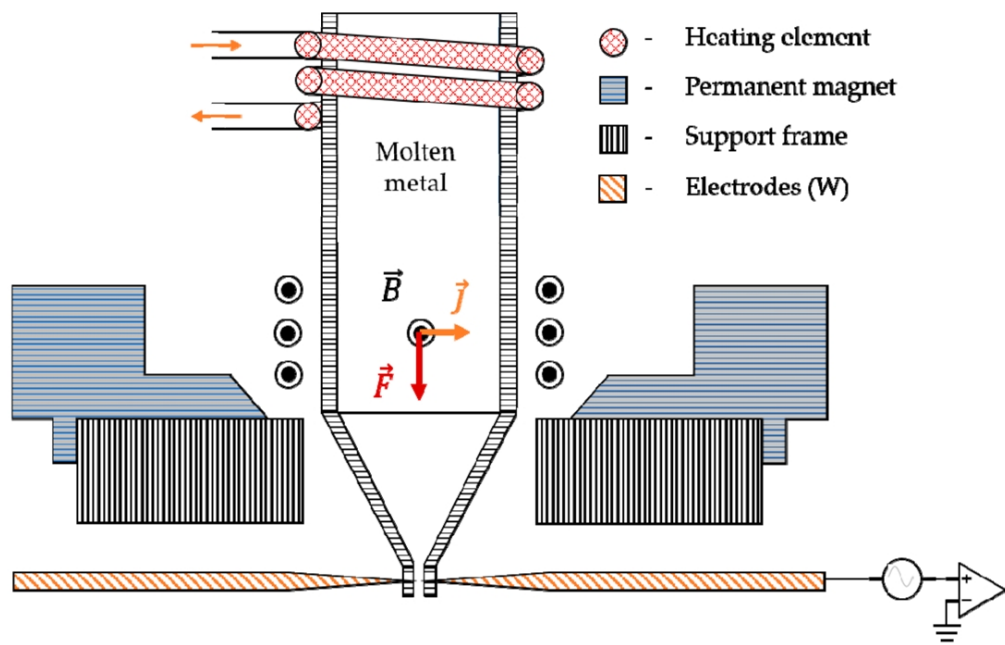


Figure 9: Schematic diagram of Magnetohydrodynamic (MHD) printing technique from Ansell et al. [37].

Pneumatic Drop-on-Demand Printing has two conduction: low temperature (Figure 10) and high temperature [37]. Different from the previous printing method, pneumatic DOD printing squeezes the droplet by applying pressure on the end of the material. A research group investigated two methods of jetting EGaIn (melting point of  $15.7^{\circ}\text{C}$ ) out of North Carolina State University [49]. First was the 'syringe method', in which a syringe pump and piston are used to push the alloy out of the syringe needle with constant downward pressure coming from the coordination between the syringe assembly and the substrate stage. The second method controlled the height of the liquid alloy in the syringe to provide stable hydrostatic pressure. Wang and Liu [50] developed quite the same jetting technique, but the gas pressure was  $\text{N}_2$  from a solenoid valve-controlled cylinder which droplets have a quick speed of solidification.

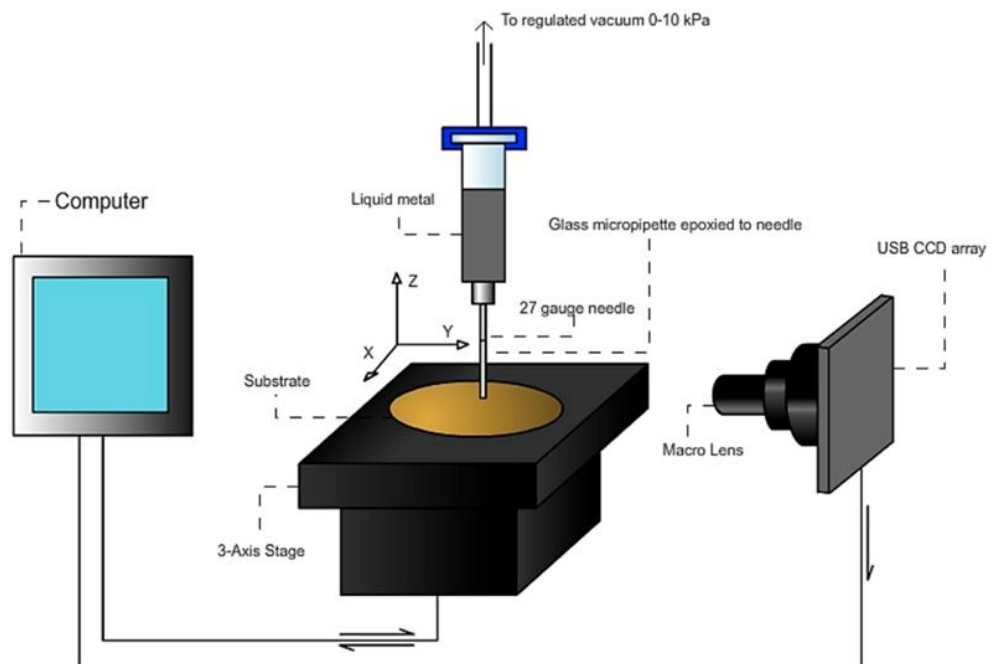


Figure 10: Schematic diagram of low-temperature Pneumatic Drop-on-Demand printing technique from Ansell et al. [37].

As for high-temperature materials like over 300°C metals, piezoelectric actuation becomes difficult because of non-piezoelectric in PZT and mechanical stresses from repeating temperature changes as well as increasing susceptibility of oxidation of the metal. To resolve these problems, Metz et al. [51] developed StarJet (Figure 11), a pneumatic actuation technology. This technique uses inert gas to squeeze the metal from a star-shaped nozzle. For metals with higher melting points, like steel, a crucible is designed to hold the melting metal, and a solenoid valve controls the pressure in the crucible using a function generator.

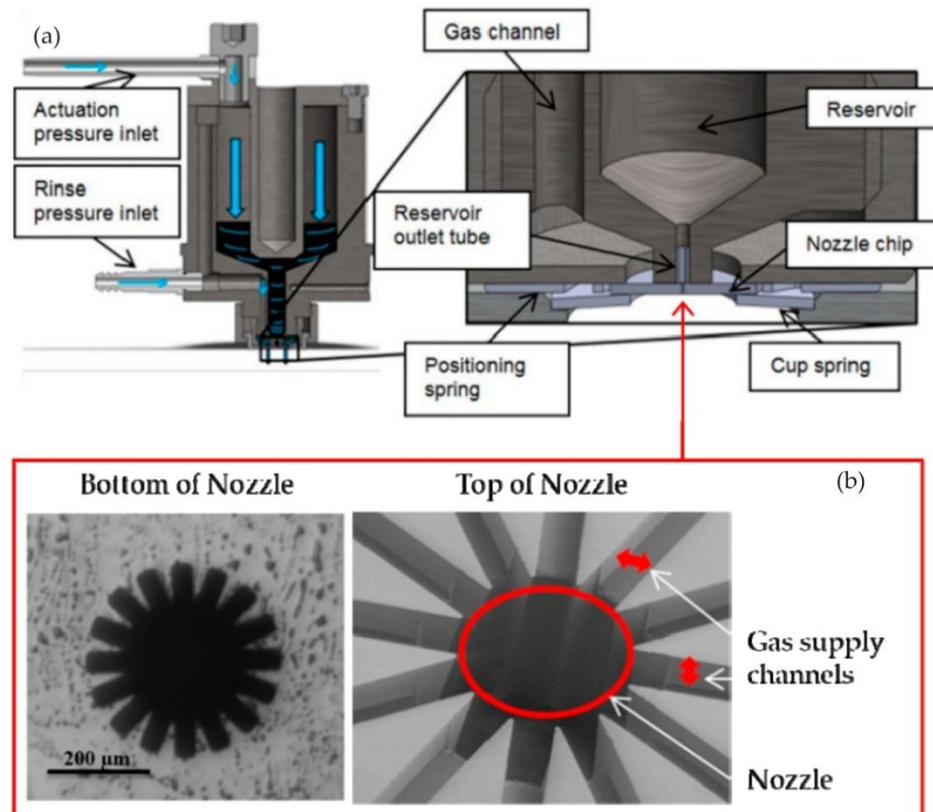


Figure 11: Figures about the StarJet technique from Ansell et al. [37]: (a) Diagram of the StarJet printhead and (b) an SEM micrograph of the nozzle

Luo et al. [52] investigated Impact-Driven Drop-on-Demand Printing (Figure 12), which was like the piezoelectric DOD systems but changed the

piezoelectric element into an impactor directly connected to the material. This system provides a force from a vibrating rod in the material above the nozzle to jet the metal. A solenoid actuates the impactor and hits the vibrating rod to transfer mechanical waves to the piston.

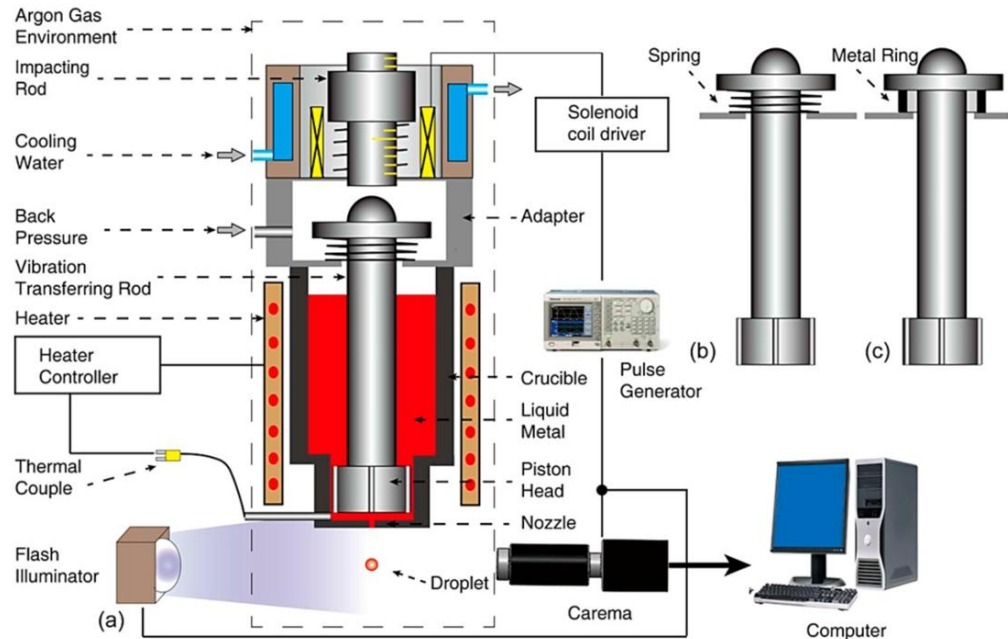


Figure 12: Schematic diagram of Impact-Driven Drop-on-Demand printing technique from Ansell et al. [37].

Laser-Induced Droplet Generation is different from all previous methods. It is the only method that uses solid metal rather than melting metal to print an object. Bohandy et al. [53] first demonstrated 'the direct deposition of metal droplets onto a substrate by laser-induced localised melting of a donor film' in 1986. In the next two years, "laser-assisted forward transfer" (LIFT) (Figure 13) was also developed by Bohandy et al. [54]. This method uses a focused beam to eject the donor onto the substrate under the metal film. LIFT solves some issues with other DOD techniques: temperature, viscosity, and resolution limitations.

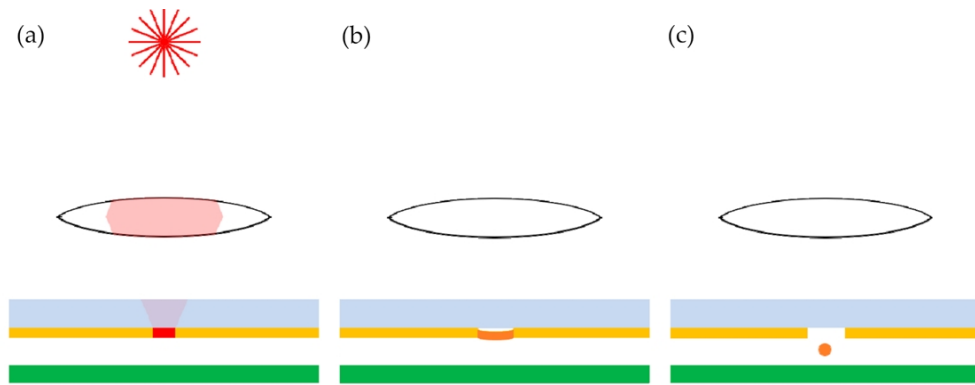


Figure 13: Schematic diagram of Laser-assisted Forward Transfer (LIFT) technique from Ansell et al. [37].

A new material jetting type called nanoparticle inkjet technology from Israeli company Xjet doesn't use melting metal, but a unique liquid carried nano-particle metal to print the object [55]. The oily liquid almost wholly evaporates when touching the substrate to decrease porosity. The final part is subjected to high temperatures to reach the final property.

## 2.3. The substrate system selection of the metal 3D printing

### 2.3.1. Introduction

This section briefly summarises the primary targets (substrate plate material, etc.) and side targets (nozzle substrate system, etc.) used in different additive manufacturing techniques based on the 35 different metal 3D printing articles. The following subsections will compare the techniques with the metal droplet extrusion technique, which is the technique researched in this thesis. It will be divided into two parts: the article's aim and the material's properties.

Finally, the chosen substrate material will be explained.

### **2.3.2. The Classification of the Substrate System in the Articles**

As a new technique that has only recently emerged after several years of development, a review of previous articles is essential and helpful for designing the substrate that will be used to deposit the droplet. The articles and their authors could give guidance and inspiration, especially regarding the choice of substrate plate material and the heating method for the substrate plate.

After a brief reading and classification, 35 articles out of 100 were selected for detailed reading and essential data recording. The technique used in this thesis is metal droplet extrusion, and the primary material that can be printed is aluminium 6061 alloy. So, there will be more articles using aluminium and aluminium alloy as their droplet material. It will also be displayed in the graph to clarify the data. The research key target is to figure out the droplet material, the substrate material, the substrate temperature needed and the method to heat the substrate plate. Also, the side targets, including the nozzle substrate distance, the surface post-processing, droplet temperature, etc., have been determined.

In this thesis, a substrate system, including the container, the plate material, the temperature control, and the connection plate to the 3D moving platform, should be designed and developed to complete a whole useable prototype printer without any previous reference design. The list of the recorded vital information and the references has been clarified in a simple understanding and clarifying way and will be shown in Table 2. Because some articles have researched more than one type of material, both droplet and substrate, the total number of the kinds of droplet material and substrate plate material will be more than the total article number. This appearance will

also be exhibited in Table 2 of the list since all the material will occupy an extra line under the main article line. Also, the researchers used 35 different printing methods, and the names of different techniques were directly collected from the articles with respect to the authors. An extra Table 3 will be displayed after Table 2 to show the substrate surface roughness and the distance between the nozzle and the substrate surface. Two Figures will illustrate the droplet and substrate material classification from these articles.

Table 2: Data collection from 35 articles

No	Printing Method	Droplet material	Substrate material	Heating Type	Substrate temperature(°C)	
1	MetalJet	Sn grade 5N	Cu plates (99.9%)	/		[56]
		Ag grade 6N	Al <sub>2</sub> O <sub>3</sub> substrate			
2	MetalJet	Cu grade 5N	Tempered 99.9% Cu sheets	Stage controller	500	[57]
		Sn grade 5N	Sn		50/100	
3	Droplet-based metal printing	Aluminium 4047A	Nickel sheet	/	300, 400, 500	[58]
4	PDM (precision droplet-based net-form manufacturing)	Pure Aluminium	Copper	/	20	[42]
5	Metal micro-droplet deposition manufacture (DoD)	Aluminium alloy	H13 stainless steel	Copper heater block	77~323	[59]
6	GMAW (gas metal arc welding) / GAW (Gas Arc Welding)	Aluminium ER1100	1100 aluminium	/	/	[60]

			A36 low-carbon steel			
7	MagnetoJet-MHD (magnetohydrodynamic DoD)	Aluminium 4043	Stainless steel	/	62	[61]
		Aluminium 6061				
		Aluminium 7075				
8	Pneumatic DoD	Sn-40 wt.%Pb alloy	Copper foil (99.999%)	Copper heater	170~220	[62]
9	Magnetostrictive actuator (MMDoD)	Sn96.5Ag3.5	PLA	/	/	[63]
10	Molten Al droplet deposition (DoD)	Pure Aluminium	/	/	27	[64]
11	Metal micro-droplet ejection	Steel EN1.3505	Glass	/	Room temperature Water/oil temperature	[65]
12	Pneumatic DoD	Cu	Steel	/	640~680	[66]
13	Pneumatic DoD	Indium	Stainless steel	/	/	[67]
		Tin				
		Lead				
		Bismuth				
		Zinc				
14	Alternate droplet printing	Sn-40 wt% Pb	Al <sub>2</sub> O <sub>3</sub> plate	Resistant heater	118.7	[68]
15	Droplet deposition 3D	Sn-63 wt% Pb	Copper	Substrate heater	50~240	[69]

	printing (Horizontal plate)					
			H13 stainless steel			
16	Pneumatic on-demand ejection	Aluminium 7075	H59 brass	Heating substrate	250	[70]
17	pressure pulses (Pneumatic DoD)	Aluminium 7075	Ni substrate	/	/	[71]
18	Pneumatic DoD	Tin	Stainless steel	Copper block with 125W cartridge heaters	room temperature (25) /240	[72]
19	Starjet technique	AlSi12	Al plate	/	not heated	[73]
			Macor			
			Stainless steel 1.4404			
20	Soluble core-assisted aluminium droplet printing (Uniform metal micro-droplet deposition system)	Aluminium 7075	water-soluble gypsum	Temperature controller	50, 250, 450	[74]
21	Horizontal Molten metal droplet deposition	Solder Sn-63 wt% Pb	Copper	Temperature controller	145/440	[75]
		Aluminium alloy Al Si-10 wt% Mg				
22	Drop-on-demand deposition using ultra-high frequency induction heating	Inconel 625	Inconel 625 alloy	/	394	[76]

23	Starjet technique	Aluminium alloy (Al 88%, Si 12%)	Water-soluble core (Semi-hydrated gypsum (CaSO4 0.5H2O))	/	27	[77]
			Silica (SiO2)			
			Magnesium sulfate heptahydrate (MgSO4 7H2O)			
			Distilled water (H2O))			
24	novel pneumatic drop-on-demand	Aluminium alloy	Asbestos	/	Room	[78]
25	Piezo anti-gravity electric field horizontally ejected droplets	Sn63%Pb37%	Copper	Substrate heater	125, 140, 155	[79]
26	Molten metal micro-droplet deposition (Piezoelectric)	99.999% aluminium	H59 brass	Substrate heater	27, 250, 450	[80]
			Silver-plated ceramic			
27	Piezoelectric	99.1000% aluminium	Brass	/	30	[81]
28	MDDM (Metal micro-droplet deposition manufacture)	Aluminium 7075	Copper	Temperature controller	350, 370, 400, 420, 450 & 500	[82]
29	Metal micro-droplet 3D printing	Aluminum 7075	Coppe	/	25, 125, 225, 325, 425	[83]
30	Pneumatic DoD	Aluminium 380	H-13 tool steel	Temperature controller	25	[84]
		Bismuth	303 stainless steel			

			Brass 330			
31	Solder jetting	63%Sn-37%Pb solder	Copper-FR-4 material	Heated platen	25/35-115	[85]
32	Molten Metal Drop Deposition	99.9% nickel	Copper	/	room	[86]
			Aluminium			
			Stainless steel			
			Fused quartz			
33	Electrochemical additive manufacturing (ECAM)	Nickel	Brass	/	/	[87]
		Copper	Copper			
			Polyethylene terephthalate (PET)		/	
34	Selective Laser Melting (SLM)	Ti6Al4V	Stainless steel	/		[88]
			Carbon		/	
35	Electrodeposition-based 3D Printing	Copper	Platinum-coated silicon wafers	/		[89]

Table 3: The data collection of substrate surface roughness and the distance between the nozzle and the substrate

No.	Distance	Roughness	
1	1mm	/	[56]
2	1mm	0.01 $\mu$ m	[57]
3	6mm	/	[58]
4	500mm	/	[42]

5	18mm	0.5 ~ 5.0 $\mu$ m	[59]
6	/	/	[60]
7	3mm	/	[61]
8	10-20mm	3.76 $\mu$ m	[62]
9	5mm	/	[63]
10	20mm	/	[64]
11	6.5m (total) for 8 levels	/	[65]
12	25mm	/	[66]
13	3mm	/	[67]
14	/	/	[68]
15	3.5mm	0.23 $\mu$ m	[69]
16	10mm	/	[70]
17	/	/	[71]
18	815mm	0.06~3.45 $\mu$ m	[72]
19	50mm	/	[73]
20	10 mm	/	[74]
21	18mm and 6.5mm	/	[75]
22	6mm	/	[76]
23	/	/	[77]
24	/	/	[78]
25	2~26mm	/	[79]
26	10mm	/	[80]
27	120mm	0.05~2 $\mu$ m	[81]
28	5mm	/	[82]
29	/	/	[83]
30	51~459mm (1~3m/s impact velocity)	0.06~5.0 $\mu$ m	[84]
31	0.5mm	/	[85]
32	265mm	/	[86]

33	30 $\mu$ m	0.017 $\mu$ m and 0.19 $\mu$ m	[87]
34	/	/	[88]
35	/	/	[89]

### Classification of the droplet materials used in articles

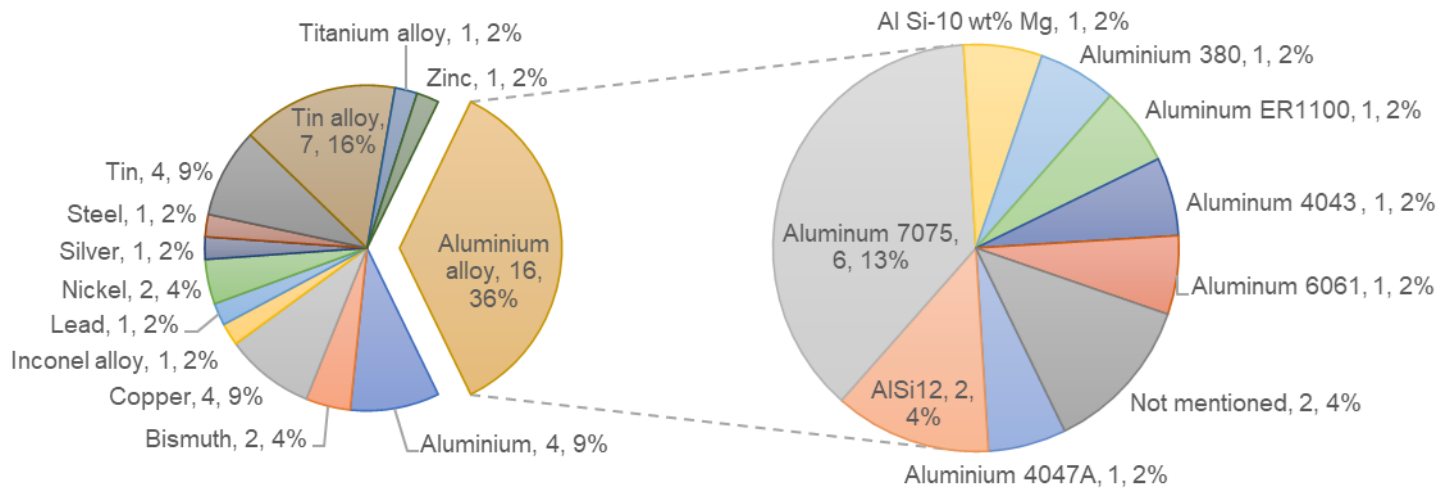


Figure 14: Classification of the droplet materials in Articles

### Classification of the substrate materials used in articles

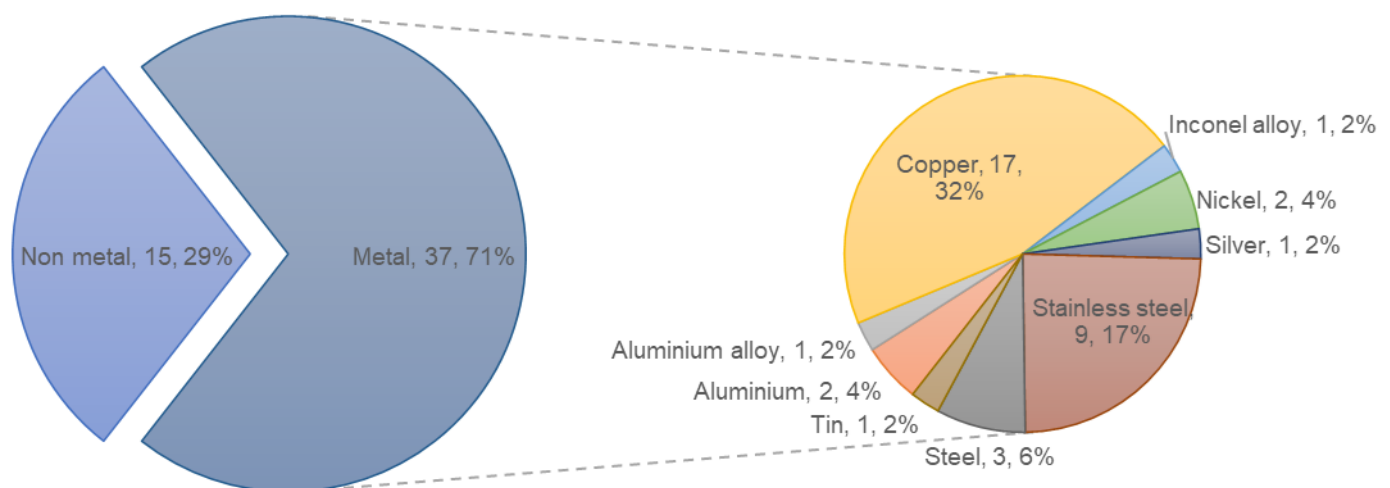


Figure 15: Classification of the substrate materials in Articles

Among the 35 different printing methods used in articles, pneumatic droplet on demand is the most popular technique, and it has been used in 7 different articles.

According to Figure 14, all the articles used 45 different materials, and the aluminium and aluminium alloy materials accounted for 16 (45%) of the total materials. Aluminium 7075 (6) is the most used material in these articles, and two articles don't have a specific type of aluminium alloy. Tin alloy has been tested 7 times and is the second most popular metal above the material type without the particular type.

According to Figure 15, which clarifies the substrate materials, the total number of all the articles used is 52, and the metal materials take up most of them – 71% (37). Moreover, copper is the most commonly used material among all the metal materials, with 17 occupying 32% of the metal materials, and stainless steel is the second most widely used material compared to other materials, which used 9 times (17%). Aluminium and aluminium alloy have the same number as the steel used by the researchers, which is 3. Other metal materials used are Inconel alloy, nickel, silver, and Tin, and each has been used 1,2,1,1 time, respectively. As for the non-metal materials, ceramic has been used 3 times, which is the most non-metal material; aluminium oxide ( $Al_2O_3$ ) has been used 2 times, and the other is Macor. Plastic and gypsum are both used twice. The gypsum has been tested by the same author, Yi et al. [74], [77], who wants to use the soluble core as the substrate surface to improve the inner quality of the thin-wall parts. Also, the soluble material will be easily removed by water [74], [77]. Water is also mentioned once from the 35 articles, the previous substrate material used for droplet analysis of the technique in this thesis – Metal Droplet Extrusion.

Only one article used aluminium 6061 as one of the droplet materials by Sukhotskiy et al. [61], who used stainless steel as the substrate. He tested the

droplet size from 50 $\mu$ m to 500 $\mu$ m with the substrate temperatures 600K, 700K, and 900K at the distance between the nozzle and substrate of 3mm [61]. A cup structure has been printed by the substrate temperature rising from 733K to 833K based on the height of the parts to overcome the local thermal diffusion increase and avoid the influence of the high conductivity of the aluminium alloy material [61]. However, in this thesis, the single droplet morphology will be focused on, and we will try to print simple flat shapes like a line. So, the real-time temperature-changing system is not essential and will not be considered.

Among all the articles, the information on substrate temperature and the heating method is relatively minor, showing many spaces in the list. Based on limited information, the commonly used substrate temperature for aluminium alloy is 500°C ([58] & [82]). Consider the melting point of aluminium 4047A is 577-582°C, and the melting point of aluminium 7075 is 477- 635°C. Also, the liquid droplet does not help form a good product quality since its shape will be affected by the next droplet easily. Thus, a desired temperature of 550°C as the highest temperature of the substrate plate has been considered because the material used is aluminium 6061 and at this temperature, the material will not totally melt, but the behaviour will be like the liquid, which will help for the remelting of the droplets, hence is beneficial to product printing. But it is okay if the plate reaches the temperature of 500°C, as shown in the articles ([58] & [82]).

As for the heating method, there is less information than the substrate temperature. Based on the experiment setup section and the schematic view of the equipment in the article, most of the researchers will use the direct heating method to heat the substrate plate, which is just connecting the substrate plate to the heater and controlling the temperature of the heater ([57], [59], [62], [68], [69], [70], [72], [74], [75], [79], [80], [82], [84] & [85]). The

induction heating method has been considered and compared to the direct heating method at the beginning of this project. However, induction heating has too many drawbacks: no commercial products, limited container material, and a complex control system. Hence, the direct heating method is chosen for this thesis.

Other factors, such as the distance between the nozzle and substrate and the surface roughness, are also taken into consideration and collected in Table 3. The distance from 35 articles in Table 3 varies from 30 $\mu$ m [87] to 6.5m [65] for different technologies and materials. However, for the aluminium and aluminium alloys, the distance is from 3mm [61] to 500mm [42], which can be partly achieved in the MDE technique based on recent equipment because the screw head at the bottom of the recent print head blocks the rise height of the moving platform. If the closest distance has been approached, the biggest distance between the nozzle and the platform cannot reach 500mm, which will be 133mm. Thus, the substrate design should consider this height condition and should make the substrate fit for further experiments.

The roughness has been displayed in Table 3 and was from 0.01 $\mu$ m [57] and 5.0 $\mu$ m [59]&[84]. The articles all provide methods to make different roughness surfaces. Article [57] mentioned using SiC papers to polish the substrate to remove the oxidation layers. Other articles [59] and [84] used belt shaders to help get certain roughness. Silver has been considered the coating material in this thesis because the chemical reaction between aluminium and silver will help to catch the aluminium droplet and decrease the rebound of the droplet [80], [81]. However, it was deleted because it is unsuitable for my major and silver will be expensive.

There is still little information about how to choose the thickness of the substrate plate. The only data collected are 0.2mm [62], 0.95mm [71], 5mm [76], 6.35mm [60]&[67] and 6.4mm [72]. 6.35mm [60]&[67] and 0.95mm

[71] were used to test aluminium alloys, but the samples were too small, and the thickness was hard to prepare, so they had no reference point. Instead, commercial plates have been considered since they are cheap and easy to purchase.

## **2.4. Droplet Morphology Consideration**

### **2.4.1. Introduction**

This section will include three parts. At the beginning, the process of the impact process of the droplet will be introduced, which will contain the detailed process stage, a review of the equation from the previous articles and a brief discussion of the factors that affect the impact. Then, it comes to the splash shape, one of the final shapes after the droplet impact and solidifies. The equation and the value describe which droplet splat will be introduced, followed by the factor that affects the splash. Finally, the sphere-like shape will be discussed using contact angle calculation and influence factors.

### **2.4.2. The Impact of the Droplet**

Metal droplet extrusion acts as a droplet-on-demand additive manufacturing technology that uses droplets as the basis to form production. The droplet's morphology is essential to forming the final printed project. Because it will affect the surface roughness of the project and, more essentially, affect the strength of the whole framework of the project as the shape of the droplets, from Yi et al. [74], [77], [80], [81] found that the cold lap pores will be formed at the bottom of the deposited droplet because, in this position, the previous droplet will affect the appearance of the next droplet, which could fill the space. Also, Gilani et al. [90] observed that the inter-

droplet void occurs at the droplet contact angle of more than 90 degrees.

As a technique that uses dropping droplets to create layers, the impact of the droplet during the printing process should be understood. Many researchers [91-102] have studied the process of impacting droplets based on different 3D printing techniques. According to their articles, the whole printing process can be divided into six stages, and each stage has the figures from Mehdizadeh et al. [102], Gilani et al. [90] and Yang et al. [103] to help understand the whole process:

### 1. Pre-impacting stage

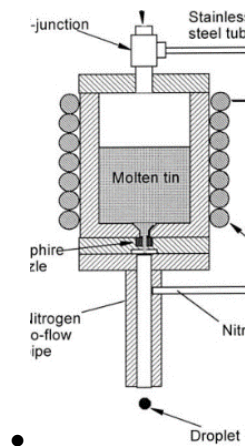


Figure 16: Schematic droplet generator from Mehdizadeh et al. [102]

- It is the stage where the raw material of the 3D printing technique is heated up to its melting point by various heating methods, and the phase of the material becomes totally liquid in the different generators based on the techniques
- The melted material (liquid) is dropped from the nozzle and approaches the substrate at a certain velocity

## 2. Impacting stage

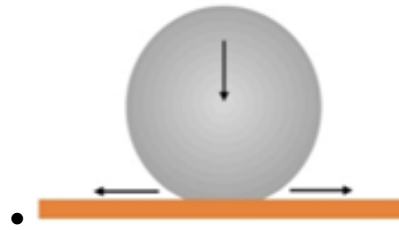


Figure 17: Impacting stage [90]

- It is the stage when the droplet reaches the substrate and starts to change its shape by the effect of the inertia

## 3. Spreading stage

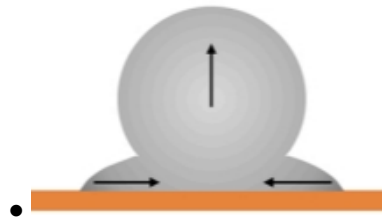


Figure 18: Spreading stage [90]

- It is the stage when the droplet becomes a thin layer and forms an edge because of the viscosity, surface tension, surface roughness, etc.

## 4. Rebounding and equilibrium stage

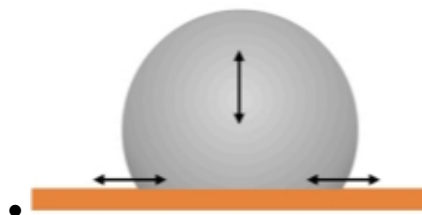


Figure 19: Rebounding and equilibrium stage [90]

- It is the stage when the droplet spreads at the maximum diameter and starts to rebound or become stable based on different situations of the substrate and the droplet itself.
- During the rebound, droplets could even leave the substrate surface and drop back again.

- Also, there could be multiple spreading and rebounding actions of the droplet, which will act as a wave.

## 5. Heat transferring and solidifying stage



Figure 20: Heat transferring and solidifying stage [90]

- It is the stage where the droplet transfers the heat to the substrate and the gas, then solidifies itself.

## 6. Final morphology stage – two types

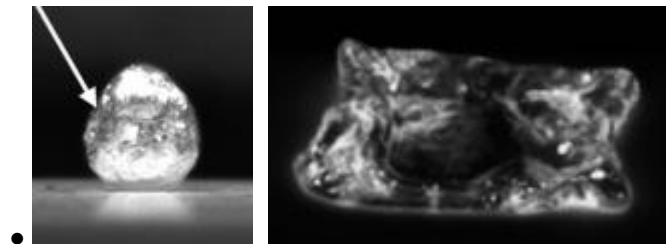


Figure 21: Two types of droplets from Yang et al. [103]

- It is the stage where the droplet is stable, which means it doesn't have any deformation and heat transfer at this position.
- The final shape of the droplet has two different types – half sphere-like and splash.

As for the impact on the spreading, rebound, and equilibrium stages, many researchers have developed different models to predict the spreading and recoil of the droplet. Early research can be recalled from 1949. Walton and Prewett [104] when they were studying the centrifuged behaviour of the spray left from the centre of a rotating disc using a parameter spreading ratio. Moreover, scientists have done more research to analyse the droplet impact model of liquids like water, ethanol, etc., which are at ordinary temperatures, and more models have been developed.

In 1993, Bennett and Poulidakos [105] collected and explained four different models- Jones' model [106], The model of Collings et al. [107], Chandra and Avedisian's model [105] and Madejski's model [108]. They also used Madejski's model [108] to explain the results of their experiment. In more recent times, Tang et al. [99] concluded and compared the results from the empiric models of the spreading factor and the splashing threshold criterion to the experimental data to study the droplet impact mechanism on different substrates of various roughness. However, these models and articles are based on the liquid droplet; when the material changes to metal, the performance of its droplet impact will be different. A high temperature is needed to melt the metal, and the material properties of the metal are totally different from those of a regular liquid.

Hence, several articles that are more suitable for the metal material jetting technique- droplet material is metal- have been reviewed in Appendix 1 to understand the droplet impact mechanism of the technique. The table will include the authors' names, the year, their metal material, their substrate material and their method or expression of the spreading factor.

According to Appendix 1, image analysis is commonly used to measure experimental data using different cameras or photography systems. As for Aziz and Chandra [100], Zhang et al. [97], and Yang et al. [103], these researchers have used the same model to predict the spread factor of their metal droplet – the Pasandideh-Fard model [92], [101].

The author, Pasandideh-Fard [92], [101], has used the numeric simulation and experiment (Figure 22) to study the impacting model of the water and tin droplet on a flat surface and how surfactant will affect the solid-liquid contact angle at the beginning of the article. Then, the Pasandideh-Fard model [92], [101] was developed, which was used to calculate a prediction of the spreading factor. After that, the predictions were compared to the

experimental measurements from others' articles and showed a good agreement with the literature data for both liquid and metal materials. This model is based on Chandra and Avedisian's model from Bennett's [105] but has been extended and developed to make it more suitable for their experimental situation.

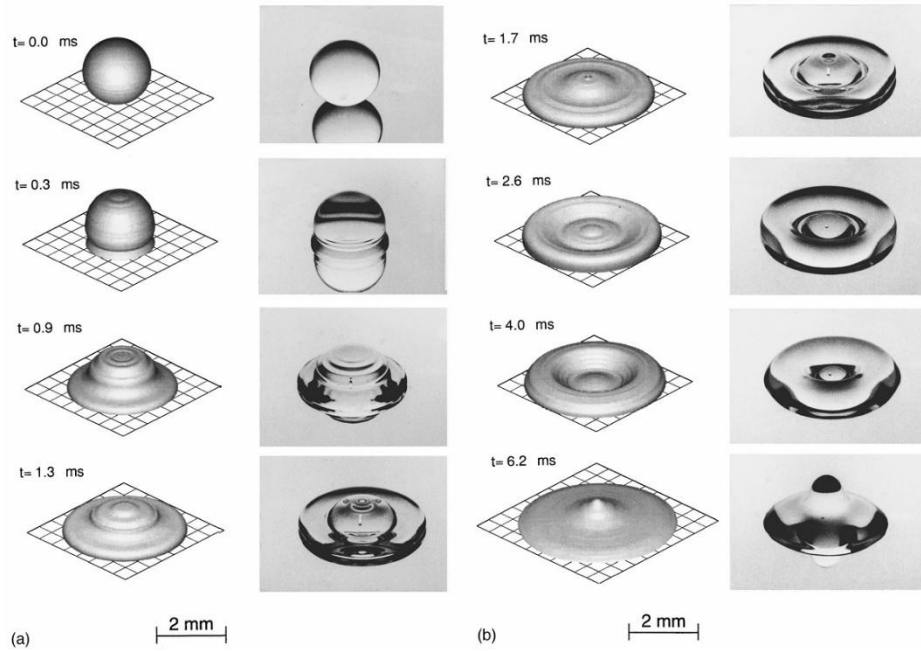


Figure 22: Computer-generated images compared with photographs of a 2mm diameter water droplet impacting a stainless steel surface with a velocity of 1 m/s from Pasandideh-Fard et al. [92].

According to Bennett's [105], all models start from the energy balance equation, which states that the initial kinetic energy of the droplets from the nozzle is equal to the viscous energy and the surface tension energy of the droplet on the solid surface.

However, Pasandideh-Frad et al. [92], [101] mentioned that the surface tension energy of the droplet itself remains at the initial stage in their articles. Based on that, the energy balance equation changes to the combination of the initial kinetic energy and the surface tension energy before the impact equal

to the final surface tension energy and the viscous energy after impacting the substrate where the initial kinetic energy was related to the impact velocity, the droplet material density and the initial droplet size; the initial surface tension energy was related to the surface tension of the droplet and the initial droplet size; however, the impacted surface tension was affected by the contact angle of the droplet on substrate.

However, as for the viscous energy, there are differences between Chandra and Avedisian's and Pasandideh-Fard's models. As explained by Pasandideh-Fard et al. [92], [101], Chandra and Avedisian assumed the characteristic length in the y direction was the same as the splat thickness, which brought a 40% higher value of the maximum diameter. Instead, they assumed the length was smaller than the thickness, and the axisymmetric stagnation point flow could express the liquid motion. Based on this assumption, it estimated the energy loss was equal to the work of a droplet defending against the viscosity, which is the viscous energy affected by the Reynolds number  $Re$  of the droplet (or use the Weber number  $We$  to simplify the equation). The maximum spread factor equation, which represents the division of the maximum spread diameter into the initial diameter, was given by rearranging the equations from Pasandideh-Frad et al. [92], [101].

In the article [92], Pasandideh-Frad et al. tested the maximum spread factor with the data that  $26 < We < 641$  and  $213 < Re < 35339$  and found the error between the predicted and measured factors was less than 15%, which means the equation was fixed well. Moreover, the article [92] also mentioned that if  $We \gg \sqrt{Re}$  the capillary effect can be regarded as negligible, and if also  $We \gg 12$ , the equation can be simplified to an exponential function with stable exponent and multiplier related to the base  $Re$ .

Although Pasandideh-Fard's model [92], [101] fits well, the prediction is based on the liquid droplet and doesn't consider the solidification and heat

transfer of the metal droplets [100]. So, Aziz and Chandra [100] made another hypothesis that all the kinetic energy stored in the solidified layer was lost when the droplet spread to the maximum diameter. The kinetic energy loss could be approximately concluded as an equation based on the average thickness and diameter of the entire flat droplet [100]. Thus, the maximum spread factor equation from Aziz and Chandra [100] was related to the dimensionless thickness that was defined by the droplet thickness divided by the initial droplet diameter, which can be used in the situation of isothermal droplet impact, where the solidification does not happen.

However, Aziz and Chandra [100] also used Tin as the droplet material, which has a relatively lower melting point ( $231.97^{\circ}\text{C}$ ) and a thin invisible oxygen layer (invisible-stannic oxide (Britannica)). Hence, the effect of the oxygen layer on the impact of the droplet is small, but it still caused a higher calculated value than the measured value based on the review of the article from Pasandideh Fard et al. [92], [101].

This phenomenon has also been observed in Yang et al. [103], which studied the influence of the oxide layer on the impact mechanism of molten aluminium (Figure 23). Yang et al. [103] illustrated that the predicted value fits well with the experimental value where there is a hypoxic environment and gave the explanation that the initial mechanical energy cannot be entirely transformed into surface tension energy because of the vortices inside the droplet, the presence of surface energy, and cracks in the layer.

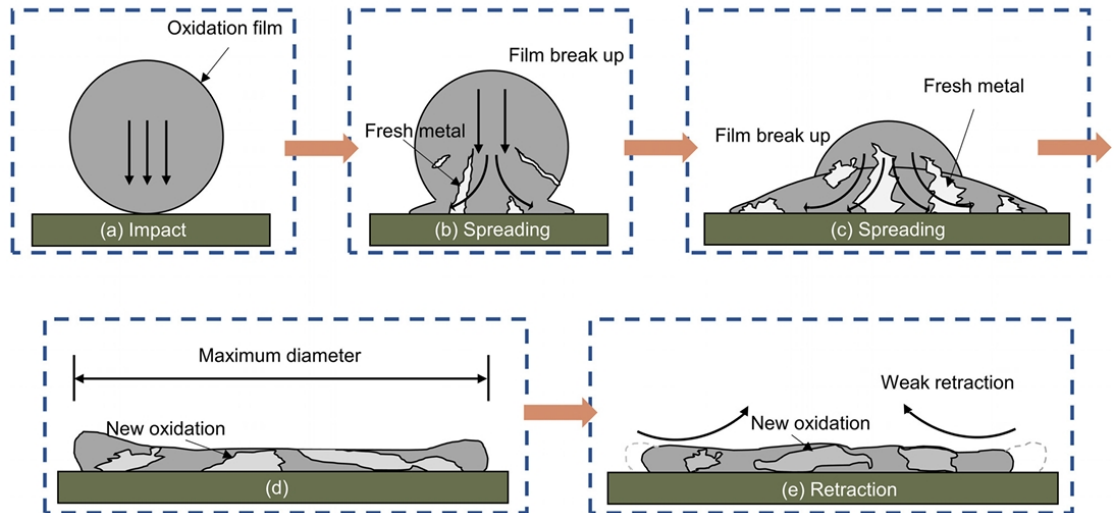


Figure 23: Schematic diagram of the collision behaviour of aluminium droplets covered with an oxide layer in an air environment from Yang et al. [103].

Therefore, they tried another model – the Ryan model, which was developed by McGuan et al. [109]. The advantage of their model lay in that they considered the effect of the oxide layer [103]. Still, it simplified it into a transformation process between the kinetic energy and elastic potential energy of the oxidised droplet without the break of the oxide layer, which circumvented the complexity and the challenge of modelling the three reasons concluded by Yang et al. [103]. The spread factor of the Ryan model [109] is proportional to the Weber number raised to the power of one-half.

The mean relative error between Wenjie’s experiment [103] data and Ryan's model [109] is 2.9%, which is much smaller than the 18.4% from the Pasandideh-Fard model [92], [101].

Go through the articles about the process of the droplet impact; the spreading factor is an essential element in explaining the mechanism of the droplet behaviour. The factors that affect the impact process can be concluded by dividing the parameters of the droplets, the impact surface, and the local gas layer [110], which will appear in the spread factor. For example, poor

wettability leads to a smaller spread factor [110]; a lower oxide layer will have a higher spread factor [103], and a higher initial velocity will increase the spread factor.

However, the more detailed morphology of the droplet will be discussed in the following two sections since the spread factor is not apparent enough to describe the impact of the droplet compared to the shape of the droplet – splash shape and half-sphere shape, which can be observed directly and are easy to recognise.

### 2.4.3. Splash Shape

Based on the definition of Mehdizadeh et al.[102], splash is the disintegration of a single droplet to generate satellite droplets during the impact process, which will decrease the solidification efficiency because of the bouncing of separate tiny droplets. A derived schematic view of the splash is shown in Figure 24 by Mundo et al. [94]. Before the impact, the droplet is a sphere. After the droplet dropped onto the plate, a liquid film from the main droplet diffused and formed a corona. The corona grew with the pouring liquid from the droplet, which caused instability of the corona, and finally, the formation of a secondary droplet flew away from the main droplet.

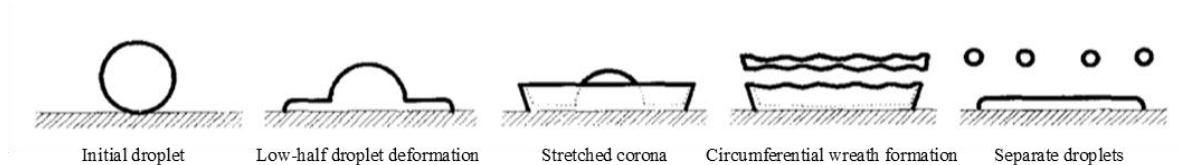
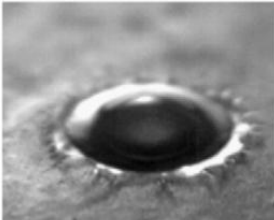
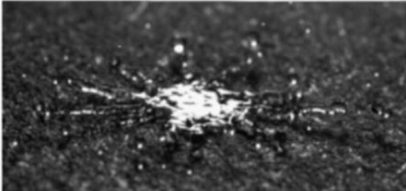
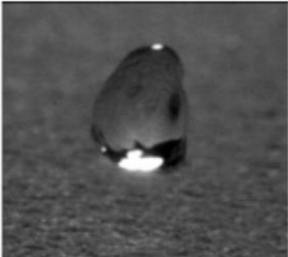
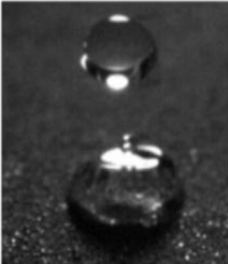


Figure 24: Schematic view of splash droplet from Mundo et al. [94].

However, the future article from Rioboo et al. [111] has clarified clearly and detailed the situation of the outcomes from a droplet impact into 6

different morphologies, which are concluded in Table 4 as well as the corresponding figures from Roisman et al. [112] - the Table 4 including the names of the outcomes, the figures and the descriptions of each outcome

Table 4: Outcomes of the droplet impact process [111], [112]

Name of outcome	Description	Figure
<b>Deposition</b>	The droplet only deforms and stays on the substrate throughout the process.	
<b>Prompt splash</b>	The droplet has a spreading of the lamella between the liquid and the substrate.	
<b>Corona splash</b>	The droplet forms a corona and spreads, finally breaking into tiny droplets.	
<b>Receding breakup</b>	The droplet is left on the substrate in the preceding phase.	
<b>Rebound</b>	The entire droplet rebound on the substrate	
<b>Partial rebound</b>	Part of the droplet rebound and part of the droplet stays on the substrate.	

However, Bejan and Gobin [93] use construal law to analyse the flow of

the droplet impact and prove the factors that affect the disc shape, ring shape and needle shape of the droplet. Azar et al. [96] found the relationship between the offset distance and the splat shape by observation and simulation. With a considerable pin height, the splat will have a V-shaped notch in it, which makes the droplet. Conversely, the short pin height will cause a growth of the ‘finger’ at the edge of the splat.

In some fields like engine design and lacquer spraying, the droplet is required to become a splash shape to achieve the particular target – effective burning [113] or special coating [114]. However, in 3D printing, a sphere-like droplet is needed, especially in a droplet-on-demand technique, since the droplet is the smallest element to constitute the final project. A splash or awkward shape of the droplet will cause small holes inside the project and also foul surface roughness caused by the sharp edge, which requires complex or time-consuming post-processing. Thus, it is necessary to find the mechanism of the splash occurrence.

In order to observe the limitation of the deposition and the splash, Mundo et al. [94] found a good relation between the Reynolds number and the Ohnesorge number. They used a factor  $K$ , called the Sommerfeld parameter in Escure et al. [115]. The relationship is

$$K = \sqrt{We \cdot \sqrt{Re}} \quad \text{Equation 1}$$

Where the Reynolds number and Weber number are

$$Re = \frac{\rho V_0 D}{\mu} \quad \text{Equation 2}$$

$$We = \frac{\rho V_0^2 D}{\sigma} \quad \text{Equation 3}$$

Where  $\rho$  is the material density,  $V_0$  is the initial velocity of the droplet,  $D$  is the initial diameter of the droplet,  $\mu$  is the kinematic viscosity, and  $\sigma$  is the surface tension of the material

Mundo et al. [94] also mentioned that a value of  $K$  equal to 57.7 is the edge of the change in droplet deformation. A value bigger than 57.5 causes an incipient splash; on the contrary, the droplet whose  $K$  value is less than 57.5 can ultimately deposit on the substrate.

In 2001, Escure et al. [115] reviewed the article of Mundo et al. [76]. They combined this value with the value from Lavergne and Platet [116], which discovered that  $K$  equals 3, the boundary condition of a droplet from rebound to deposition and confirmed the Mundo et al. [94] value. In their observations of the alumina material, if the droplet is not solidified before reaching the substrate, it will be like a liquid droplet. It could deposit when  $K$  is between 3 and 80, but splash will occur at a value more significant than 20.

In more recent times, Tang et al. [99] have reviewed the splash threshold criterion from Stow et al. [117], Mundo et al. [94], Cossali et al. [118] and Range and Feuillebois [119]. The experimental results in the article [99] have been used to compare with the results from Stow et al. [117], [118] and Cossali et al. [118]. Tang et al. [99] found that only Stow's model [117], [118] fits well with the water measurements, and Cossali's model [118] has a disadvantage in predicting the critical Weber number. So, in the further analysis of the data, Tang et al. [99] found the logarithmic relationship between the critical  $K$  parameter  $(We/Oh)_{cr}^{1/2}$  and the normalised roughness which has the fitting coefficients depending on the liquid and the coefficients can be found in their article. However, it is not helpful to this thesis since the material is aluminium 6061, and Tang et al. [99] did not give the exact value of the coefficients for Aluminium 6061. The only four materials in the article [99] that have been parameterised are water, Decane, Ethanol and Tetradecane.

According to previous reviews, the effect of the Weber number, Reynolds number and Ohnesorge number are significant on the splash parameter, which Mundo et al. [94] also conclude. Mundo et al. [94]

Compared the droplet impingement for the smoother and rougher surface and discovered that the effect of the fluid properties is more vital for the diameter distribution of the secondary droplet on the smooth surface than on the rough surface.

The splash occurs because the local surface angle transfers the tangential momentum into normal momentum. Escure et al. [115] found that the substrate temperature and impact velocity were essential to the 'classical' splashing of the alumina droplet, which is flattened with fingers at the edge.

Bejan and Gobin [93] used construal law to analyse the geometry of the impact droplet and found that the initial droplet size and velocity significantly affected the shape of the splash.

Mehdizadeh et al. [102] discovered in their experiment that the tin droplet will splash less when the substrate's surface temperature is high.

In the article from Tang et al. [99], the increase of the surface roughness forwards the formation of the splash. Lin et al. [120] have researched both surface roughness and surface temperature based on a critical value  $K_c$  where if the splash number  $K$  is more significant than  $K_c$ , the splash will happen. It is declared that in the rebound region, the  $K_c$  will become very small and not be affected by the surface temperature and roughness. However, in the deposition region, the  $K_c$  is proportional to the rise of the surface temperature but opposite for surface roughness. According to Hao [121] and De Goede et al. [122], surface roughness is the crucial factor that can transfer the corona splash to prompt splash.

Thus, when reviewing these articles, the initial droplet velocity, the substrate temperature and the substrate surface roughness should be considered carefully to avoid splashing on the aluminium droplet.

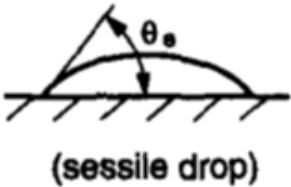
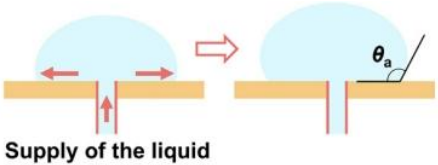
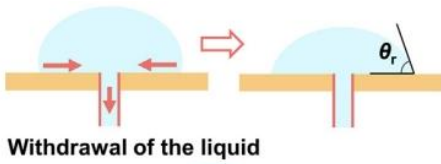
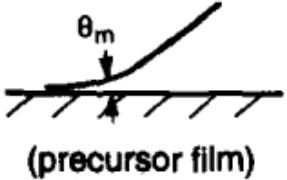
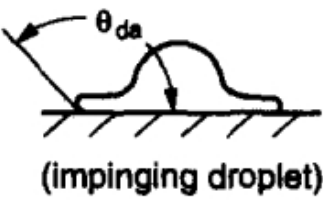
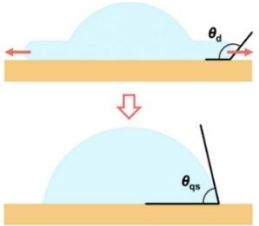
#### **2.4.4. Sphere-like Shape**

As mentioned in the previous section, the outcomes of the droplet impact have six different types. After discussing the splashing types and ignoring the rebound types since both are not suitable for the product formation of the 3D printing techniques, the deposition type, in which the droplet is more like a droplet or like a sphere, should be discussed. The study of the mechanism that affects the morphology – more specifically, the contact angle- will help people improve the printing quality of the final product using 3D printing techniques.

This unique angle can be determined by Young's equation [123], which uses the mechanical force equilibrium of three interfacial tensions at a three-phase contact line, explained by Wang et al. [124]. Young's equation [123] is the solid-vapor interface tension equals solid-liquid interface tension plus liquid-vapor interface tension multiplied by the cosine equilibrium contact angle.

Because of the different corresponding conditions, the contact angle can be divided into several different types. Table 5 concludes by combining the conclusions of Song and Fan [125], [126], and Bernardin et al. [127].

Table 5: Description and definition of different contact angles [125], [126], [127]

Contact angle name	Schematic description	Definition
<b>Equilibrium</b>	 <p>(sessile drop)</p>	The contact angle is given by Young's equation, where the ideally smooth and homogeneous solid surface, system-free contamination, and fluid motion are applied.
<b>Advancing</b>	 <p>Supply of the liquid</p>	The highest metastable apparent contact angle can be achieved by increasing the drop volume.
<b>Receding</b>	 <p>Withdrawal of the liquid</p>	The lowest metastable apparent contact angle can be achieved by decreasing the drop volume.
<b>Apparent macroscopic</b>		The contact angle is determined by extrapolating the macroscopic liquid-vapour (liquid-liquid) interface to the mean solid surface, which depends on the position of the three interfaces intersecting (roughness).
<b>Microscopic</b>	 <p>(precursor film)</p>	The actual equilibrium contact angle in the microscopic precursor film is less than 1 $\mu m$ from the apparent contact line.
<b>Dynamic</b>	 <p>(impinging droplet)</p>	The changing contact angle exists in the droplet spreading process.
<b>Quasi-static advancing</b>		The contact angle in the quasi-mechanical equilibrium regime, in which the apparent contact angle remains stable

Also, in the article by Song and Fan [126], 5 different methods, including sessile bubble, captive bubble, tilting plate, Wihelmy balance and capillary rise, to measure the contact angle are concluded, which is shown in Appendix 2. According to their revision, the sessile drop and captive bubble are the two most popular methods because of their accuracy, simplicity and flexibility. Moreover, the sessile droplet is the most convenient technique due to the small test liquid quantity and tiny size samples if high accuracy is not required. Vaikuntanathan and Sivakumar [128] also illustrated that the equilibrium contact angle can be measured on a smooth surface, and the roughness should be minor.

Bao et al. [129] mentioned that the value of the equilibrium contact angle is the representation of the wetting behaviour of the liquid material in the calculation and contact angle section. Still, the influence of the curvature of the aluminium is not considered [129]. So, the method of three surface tensions of the aluminium change by temperature was tried to predict the change in the contact angle and plot all the measurements of the aluminium contact angle on the Al<sub>2</sub>O<sub>3</sub> from both their experiments and others to see the differences [129]. The linear equation surface tension of the oxygen-saturated molten aluminium is from the article of Mills and Su [130] which is related to thermodynamic temperature (higher temperature results in lower surface tension). With the comparison of the surface energy between Eustathopoulos et al. [131] and Takematsu et al. [132], the linear equation of solid-vapour surface energy of the alumina concluded that higher temperature would cause lower surface energy.

Then, they introduced the factor  $E_A$ , which is the work of adhesion, and the equation was from Girifalco and Good [133], including the function of molar volumes, the liquid-vapour surface energy and the solid-vapour surface tension. The  $E_A$  is proportional to the solid-vapour and liquid-vapour surface

energy as well as the function of molar volumes. The function of the molar volumes of the liquid and the solid was reviewed and found by Bao et al. [129]; the function of the molar value is exponential decay with temperature, and a final value of 0.755 will be reached when the temperature goes extremely high.

Another equation of work of adhesion can be calculated by combining the liquid-vapour and solid-vapour surface tension minus the solid-liquid surface tension [129]. Thus, the solid-liquid surface tension can be calculated by the function of molar value, the solid-vapour and liquid-vapour surface tension, and Bao et al. [129] found that the calculated solid-vapour surface tension value was in agreement with the results of Nikolopoulos et al. [134]. Also, the graph of the comparison of various measured and calculated contact angles affected by temperature has been plotted by Bao et al. [129], as shown in Figure 25, and it shows that increasing the temperature will decrease the contact angle with a decreasing gradient.

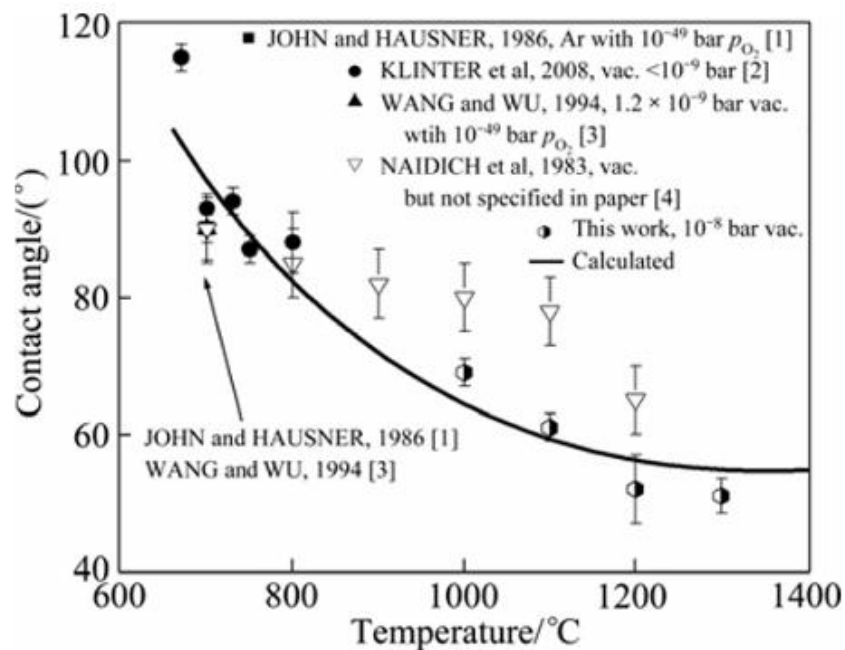


Figure 25: The graph of the comparison of measured and calculated contact angles affected by temperature from Bao et al. [129]

Some of the articles also observed the effect of temperature on the change of contact angle. Li et al. [135] found that the solidification contact angle decreased with the increasing substrate and jetting temperature. The substrate temperature affects the contact angle more effectively than the jetting temperature. Venkatesan et al. [136] indicated that the more temperature-dependent contact angle effects were observed at higher values of the rate of change of surface tension with temperature.

Villa et al. [137] use two different models - The decreasing trend model (DTm) and the Unsymmetrical trend model (UTm), to predict how the surface temperature affects the contact angle. DTm predicts contact angle well, but UTm has a mistake in the test water on the SHS plate (glass sample covered by a uniform and thin coating to generate super-hydrophobicity). The equilibrium contact angle changes slightly with the temperature of the water drop, which Song and Fan [125], [126] also observed. However, for aluminium droplets, Zhang et al. [138] indicated that a range of  $147^\circ$  of the contact angle can be controlled by the wetting temperature of 1573–1773 K.

Except for the temperature effect due to the change of the surface tension, roughness shows excellent importance in the formation of the contact angle. Two models are developed by Wenzel [139] and Cassie and Baxter [140] to predict the effect of the surface roughness on the contact angle. The difference between these two models is whether the droplet will float on the groove caused by the roughness or will fill them, as shown in Figure 26 from Wang et al. [124] that (b) is the Wenzel contact angle and (c) is the Cassie contact angle.

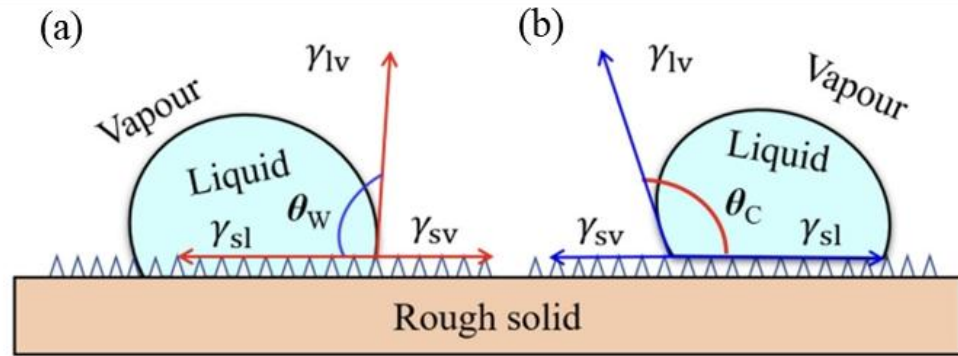


Figure 26: (a) Wenzel model and (b) Cassie model [124]

For the Wenzel equation [139], the cosine of the Wenzel angle is equal to the roughness factor multiplied by the cosine of the equilibrium contact angle where the roughness factor is more significant than 1. According to Bell and Borthan [141], the Wenzel equation is often used to predict the contact angle when the droplet size is much bigger than the grooves made by surface roughness.

Cassie's equation [140] expressed that the cosine of Cassie's contact angle is related to the solid fraction and the cosine of the equilibrium contact angle minus the quantity of one minus the solid fraction. Bell and Borthan [141] also mentioned that the effect of liquid removed from the droplet cap would cause a smaller contact angle value than Wenzel's.

Based on the experiment in Xiong and Cheng [142] with phase change material, roughness affects oscillation motion more than the spreading motion of the droplet. The rough surface will release the bubble at the bottom of the droplet, which can increase the product's surface quality. As for Quetzeri-Santiago et al. [143], the substrate roughness will increase the chance of droplet splash since it affects the dynamic contact angle. The dynamic contact angle increases with the increase of the surface roughness, but the different droplet surface tension will also influence it. Wang et al. [124] indicated that the contact angle hysteresis has a bottom value with the increase of the surface

roughness. In the article of QI et al. [144], the average roughness  $R_a$  of the rough ceramic surface is  $2.23\mu\text{m}$ , and the smooth surface is  $0.092\mu\text{m}$ . The graph of the change in the contact angle depends on the roughness change, which is from around  $77^\circ$  to  $71^\circ$  for water and  $67^\circ$  to  $51^\circ$  for glycerol.

Other factors, such as pressure and chemical effects, influence the contact angle. Champion et al. [145] mentioned that chemical reactions will occur when the alumina and aluminium have good wetting. For water, the pressure will only affect the contact angle at a temperature bigger than  $120^\circ\text{C}$  [127]. Song and Fan [125], [126] found that low pressure will have a more pronounced influence on the contact angle due to surface roughness.

As for the value of the aluminium contact angle, Bao et al. [129] have reported the calculated value of  $97^\circ$  at the temperature of  $700^\circ\text{C}$ , which is the casting temperature. The calculation in the article [129] is in good agreement with her experimental data as well as the previous author's results. Based on the contact angle, Bao et al. [129] concluded that the alumina wasn't wetted by the pure aluminium at this temperature. The article [129] also reported that aluminium's calculated contact angle values of aluminium on the Sic and graphite are  $79^\circ$  and  $92^\circ$  at  $700^\circ\text{C}$ . Ip et al. [146] indicated the contact angle value of aluminium and its alloys on the ceramic ( $\text{Al}_2\text{O}_3$ ) and  $\text{CaO}$ .  $103^\circ$  is the value reported in the article for the aluminium on alumina at  $1173\text{K}$ , and it will not change over time. The addition of other elements in the aluminium alloy, such as Ca and Mg, will decrease the contact angle.

Lin et al. [147], [148] have mentioned that the contact angle of aluminium 6061 alloys wets the Tu2 copper and the low carbon steel. For the TU2 copper, Lin et al. [147], [148] indicated that the aluminium 6061 alloy has the final contact angle of  $37^\circ$  at  $923\text{K}$  and  $21^\circ$  at both  $973\text{K}$  and  $1023\text{K}$ . However, Lin et al. [147], [148] cannot find an equation to express the

spreading model of the aluminium 6061 alloy wetting the copper plate since the alloying element affects the wettability and the interfacial structures negligibly. However, the magnesium in Al 6061 alloy reduces the oxide film by infiltrating more molten aluminium into the steel substrate for low-carbon steel. Therefore, the final contact angle is much lower at the temperature of 700 degrees, which is around  $7.5^\circ$ . Also, the change in the contact angle of the aluminium 6061 alloy is significant, from  $45^\circ$  to  $7.5^\circ$ .

## **2.5. Conclusion**

In summary, the droplet-on-demand technique has been developed for a long time, and many different droplet-producing methods have been explored and commercialised.

The consideration of the substrate is based on the 35 different articles and the critical information collected. Plastic material is not considered for the material chosen since the temperature of the aluminium alloy 6061 is too dangerous and will burn these kinds of materials. Ceramic ( $Al_2O_3$ ), copper and stainless steel are chosen to be tested in this thesis for their effect on the morphology of the droplets because they are used more in the articles and are suitable for the droplet material. Direct heating method – a heater will be selected to heat the substrate plate because it is economical and practical. The substrate system should be designed as close as possible to the nozzle. The detailed design inspiration and the development of the system will be shown in Chapter 3 methodology. And a new printer prototype will be introduced in detail including the structure and the schematic figure.

As for the factors that affect the impact behaviour, the splash, and the contact angle, the droplet properties and the impact surface will affect the spreading of the droplet. The initial droplet velocity, the substrate temperature

and the substrate surface roughness will affect the splash of the droplet. As for the contact angle, the substrate temperature and surface roughness play an essential role in changing the contact angle. Other affections will point to the oxidation and the chemical reactions between the droplet and the impact surface. Because MDE is a new technique and no experience can be referenced, the experiment setting for studying the change of the droplet morphology will be in simple but important fields like the substrate temperature and the surface roughness. Also, the distance between the nozzle and substrate can be tested to give guidance on better printing quality, and the performance of different substrate materials should be figured out to find suitable material for the technique. In the methodology chapter, the preparation and the steps of the experiments will be detailed and introduced in section 3.4. The results and analysis chapter will show the experiments' results.

## **Chapter 3 Methodology**

### **3.1. Substrate System Design Development and Testing**

#### **3.1.1. Introduction**

This section will contain 3 sub-sections. First, the original design requirements will be explained. The following section will be the substrate system development. It will include the original design part, the development part and the final assembly system. It first comes to the original design, which will explain the first design consideration and the equipment selection. Following the original design comes the design development part, which contains the developed parts' drawings and the improvement description. After the development, the whole assembly of the models and genuine

manufactured parts, including the control system, will be shown. Also, the process to control the substrate temperature will be introduced. Finally, the test for the substrate temperature and the substrate plate will be displayed to decide the final machine used in the newly designed prototype and the further study of the droplet morphology.

### **3.1.2. Requirements**

From the literature review, some of the considerations of the substrate system have been decided: the plate material will be copper, stainless steel and ceramic with different thicknesses to test; a heater with a controller will be used to heat the plate; the heater should heat the plate at least 500°C, but the best 550°C which will be a good temperature for future droplet remelt study and product printing. And the whole system size should be considered to get close to the bottom of the printhead. Meanwhile, other considerations about the remaining lab equipment, such as the safety of both humans and equipment, the difficulty of manufacture and assembly, and the operational convenience, are considered. A list of the items taken into account, both in the literature review and the others, is exhibited in Table 6, and each item will be explained.

Table 6: Design requirements and the descriptions

No.	Requirements	Description
1	Modular substrate	The design of the substrate should be convenient for removing and inserting the test plates.
2	Thermal Regulation	The controller of the heater should be simple but accurate
3	Optimal Thermal Range	The heater should heat the plate higher than 500°C
4	Compact System Design	The system should have the ability to move in the space that is limited by the 3D moving platform (300mm moving limit on the x-axis and y-axis, 130mm limit on the z-axis; the support table is 1200mm long and 800mm wide)
5	Dynamic Integration Capability	The system can lock onto the remaining 3D move platform in the lab.
6	Load Bearing Specification	The weight of the whole system with the product should be less than 20kg (platform limit)
7	System Dimensions	The system plate can catch the droplet in all ranges of the platform move limit (300mm moving limit on the x-axis and y-axis, 130mm limit on the z-axis; the support table is 1200mm long and 800mm wide)
8	Thermal Insulation Composition	The system should be insulated to prevent damaging heat to the moving platform.

The reason for the No.1 item is that multiple plates should be tested. An easy removal design can help save experiment time and is also convenient for doing the post-processing process of the printed products since the present metal 3D printing techniques always have a removable plate to put the product into the oven or other machine. The fourth item should be considered with the prototype design since the printhead cannot move, and the 3D moving platform has moving limits. Thus, this will be considered later. For the requirement of the system size, it will be better for the system to have the ability to fully use the moving range of the platform to print large-size products. However, the support structure of the induction heater and the printhead constrain the size of the plate as well as the size of the system because the substrate shouldn't hit the structure, which will cause severe damage. In that situation, the square plate with a length of 31cm is chosen, which can catch the most droplets at a safe distance.

### 3.1.3. Substrate Design Development

Based on the design requirements, the heater is essential to the whole system since other substrate system parts can be easily found or manufactured. A ceramic heater with a PID temperature controller provided by an online seller, which has the highest limit temperature at 800 degrees, has been chosen, and the original design model was built based on the size of this heater. Figure 27 shows the design's explosion view and each part's name.

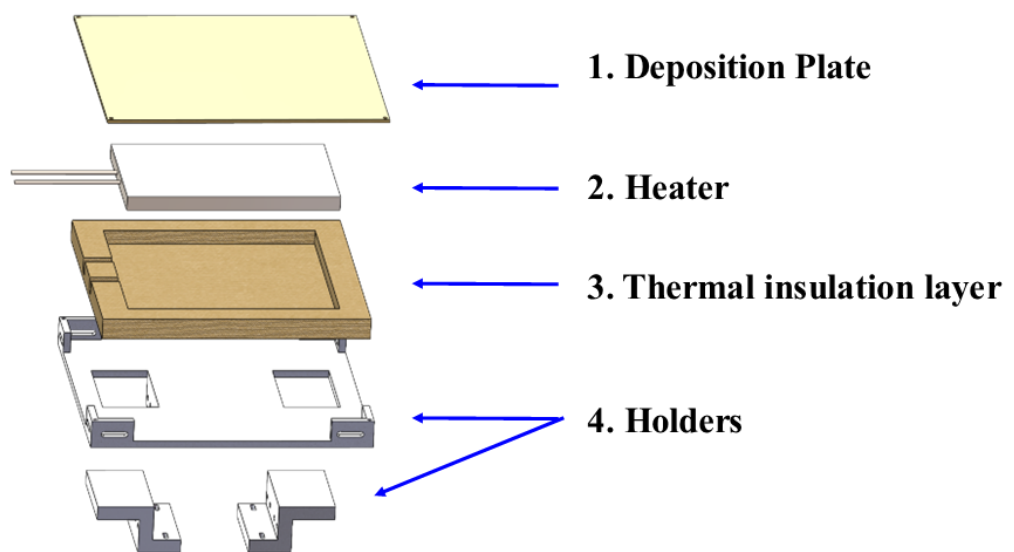


Figure 27: Explosion view of the original design

The original design focuses on fitting the chosen heater and building a simple structure with little weight to connect the substrate system and the platform. So, as shown in the explosion view, the heater is held by the holder, which contains insulation layers. The two bottom parts of the holder can lock to the 3D platform sliding brick by the screws and will insert into the two empty squares of the upper part of the holder. Screws will be used to lock both the upper and bottom parts of the holder. At the top of the whole design, the plate is directly put on the heater and will be supported by the four structures at the corners of the holder. Four screws are screwed through the four holes of the plates to fix the plate on the holder. Aluminium 6061 was chosen as the

material for the holder to reduce the weight. Ceramic fibre, which is an Aluminium silicate material, was determined to be the insulation material between the heater and the holder because it can prevent the temperature of 1260°C and has a low thermal conductivity, which is  $0.035W/m \cdot K$ .

Although the original design is simple and light, moving the plates is unsafe and hard. Because the ceramic fibre is soft, the thickness of the design cannot fix the heater. Also, the lock of the holder is only four screws which will break since they suffer both vertical and horizontal shear stress when the platform is moving up and down. Meanwhile, the screw method will cause inconvenience both in the plate preparation and the changing process of the plates.

Besides, the bottom part of the holder directly connects to the insulation layer, transferring heat from the insulation layer to the 3D platform through long-term use (at least 30 minutes for each experiment). Although ceramic fibre is adequate in insulating heat, the heat generated by the heater can still transfer to the two covers during prolonged use. As a result, the bottom holder will become heated, and the moving plate of the 3D platform may also experience deformation by the heat from the bottom holder. More severely, the heat will also affect the sensor. The deformation of the connected platform and the affected sensor will lead to inaccuracies in the movement distance. Therefore, it is advisable to incorporate a cooling component between the heater and the platform to prevent heat transfer from the heater, thereby protecting the moving platform.

The design has been developed and changed twice to improve the system and achieve the requirements as much as possible. Finally, the design's third version is the system's final version, which is shown in Figure 28.

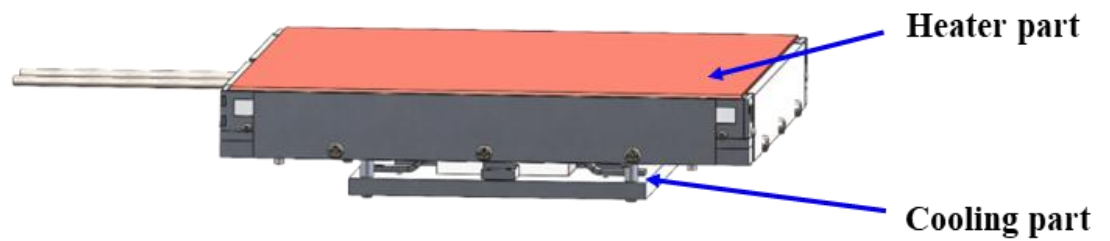


Figure 28: Final version of the substrate system without the PID controller

The total substrate system contains two parts: the heater part and the cooling part. The heating part is the element that contains the heater and support and holds the test plates. The size of the shown whole part is 332mm x 332mm x 42mm; the height is from the plate surface to the bottom of the part without the pins connected to the cooling part, and the side length doesn't include the head of the screws. The plate thickness can change, and the total height of the part can also change. These sizes have been measured and decided by the movement of the 3D moving platform and the size of the 3D moving platform desk, which will be the basement of the printer structure. One problem may be the plate thickness when calibrating the moving platform, but the plate can be taken off during the calibration and then put back when doing experiments. Next, Figure 29 shows the up, bottom, and disassembly views of the heater part model, which contains eight different parts, and all will be assembled by the screws and the easy mortise and tenon joint.

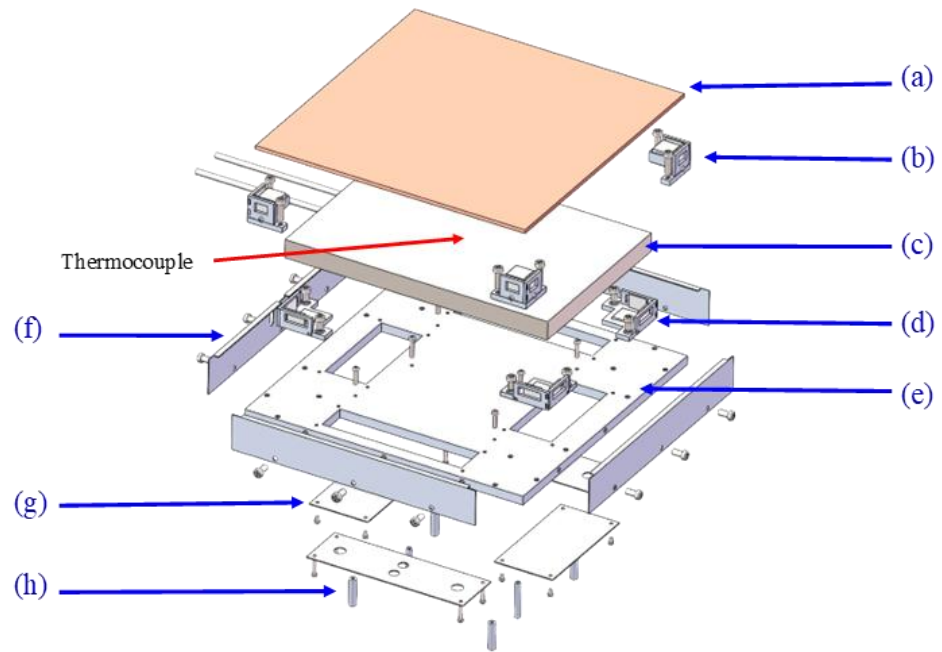


Figure 29: Explosion view of Heater part

The eight different parts will be (a) a plate, (b) 4 plate supports, (c) a heater with a thermocouple at the centre, (d) 4 heater supports, (e) a base, (f) 4 side covers, (g) 2 pairs of the different bottom cove and (h) 6 different sizes pins including 4 pins lock to the cooling part, and 2 pins lock to the moving platform.

For the (c) heater, the dimensions are 300mm x 200mm x 18mm with the power of 1500W from Taobao “海红电热”. This heater was the most suitable commercial heater that can be found on Taobao, with the highest limit temperature of 800°C and a working temperature of 500°C~700°C. The other structures were designed to fit the dimensions of the heater and the limit of the 3D moving platform, for the design in Figure 29, a 310mm x 310mm space for printing the products. However, the final printing space was 200mm x 200mm because the big plate had un-uniformed heat dissipation that was not equal on such a big plate, as shown in Section 4.1.1. Also, the price (650 yuan

with controller) is relatively low compared to other commercial heaters or custom-made heaters, which fit the original purpose of the MDE technique (cheap to use). The thermocouple is placed in the centre of the whole heater, and the heater's temperature will be displayed on the PID controller connected to the heater.

The plate support (b) and the heater support (d) are made of 4 pieces which are tightened by the screws and the easy mortise and tenon joint. The model of them will be shown in the following Figure [30-33]. The hollow at the base aims to decrease the weight and provide a space to insert the spring thermocouples to measure the plate's temperature. The space remaining in the heater part is the location of the insulation layers. The covers around the base will close the whole design, not allowing the insulation layer (ceramic fibre) to go out.

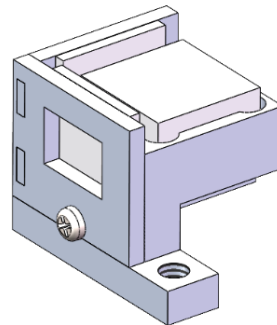


Figure 30: Assembly view of the plate support

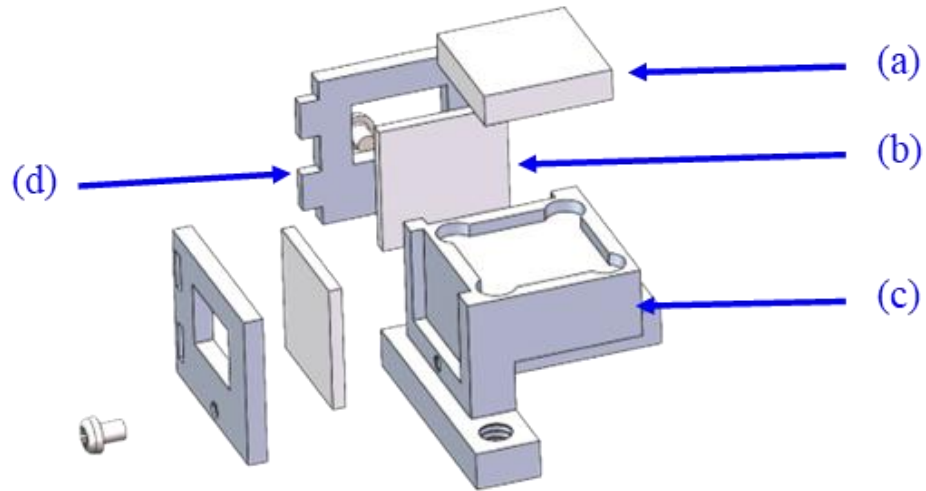


Figure 31: Explosion view of the plate support

Each plate support is assembled by 4 different pieces: (a) a 4mm ceramic plate, (b) two 2mm ceramic plates, (c) a support base and (d) two covers connected by easy mortise and tenon joint. The ceramic plates will disconnect the heater directly from the plate to protect the body of the support since the plate may have a high temperature of over 500°C, and the support material will be aluminium 6061 alloy. The circle at the top corner of the support base is designed to simplify the manufacturing process since the sharp corner will be hard to achieve with the standard 3-axis CNC knife and will cost more money. The space at the cover and the bottom of the support base aims to reduce the weight and transfer less heat from the plate, which can protect the covers and the base of the heater part. Figure 32 and Figure 33 show the heater support model, which has the same design considerations.

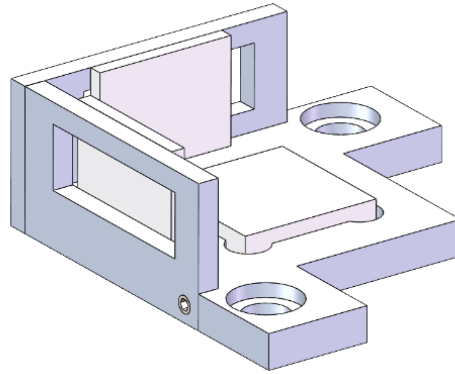


Figure 32: Assembly view of the heater support

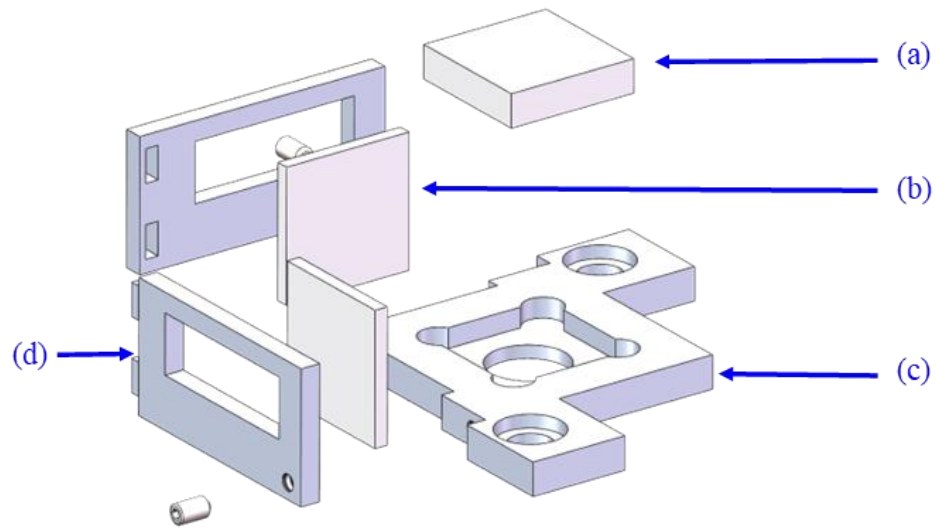


Figure 33: Explosion view of the heater support

The heater support is also formed by 4 pieces: (a) a 4mm ceramic plate, (b) two 2mm ceramic plates, (c) the support base and (d) two covers connected by easy mortise and tenon joint. Unlike the plate support, the heater support will transfer the heat directly from the heater, which can reach 800°C, but the material will still be aluminium 6061 alloy. Thus, a bigger space in the cover and an added hollow in the base are designed to decrease the transferred heat. The ceramic is used to disconnect the heater, and the part is made of

aluminium 6061. The whole support also lifts the heater, which protects the base of the entire design. But, because of the thickness requirement of the whole design, the heater cannot be lifted too high, so the thickness of the base is 5mm. Counterbores are designed to avoid the intervention between the heater and the head of the screws. Figure 19 and Figure 20 show the cooling part.

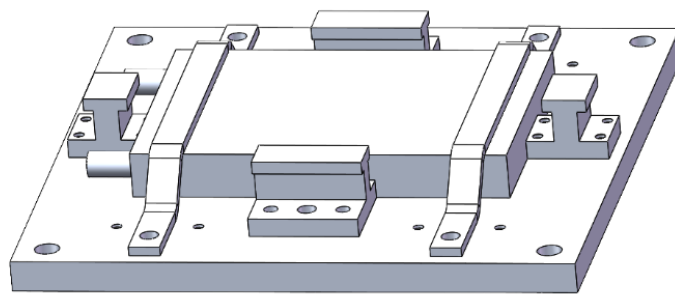


Figure 34: Assembly view of the cooling part

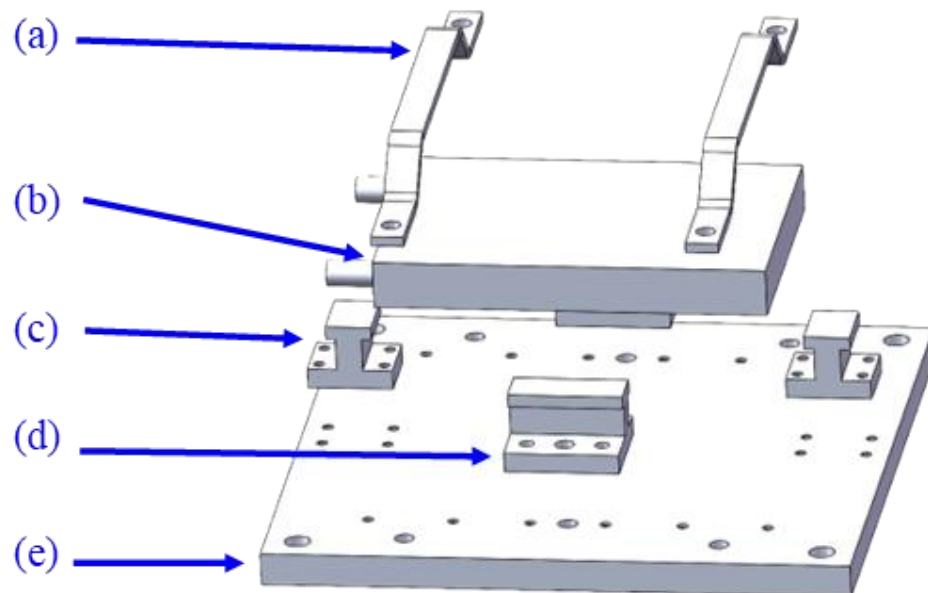


Figure 35: Explosion view of the cooling part

The cooling part contains five different parts: (a) 2 lock bars, (b) the water cooler, (c) 2 I structure supports without hollow, (d) 2 I structure supports, each with a hollow for through the pin, and (e) a base. The whole cooling part is designed based on the size of the water cooler and made of aluminium 6061 alloys, which results in good heat dispersion, is lightweight, and has a low cost. Because the water cooler is a commercial product and there are no holes for the screws to go in, the bars block the up-and-down movement. In contrast, the four I structure supports block the parallel movement by directly connecting to the water cooler. Also, the lock bars and the I structure are designed to reduce the weight but still have good structural strength to support the heavy heater part. Then, the I structure has a smaller top to transfer less heat from the heater part, and the large connection surface to the air also increases the heat dispersion ability. The cooler can also protect the connected support.

Compared to the previous original design, all the requirements from the beginning have been considered and achieved uniquely. So, the 3D model of the whole design is transferred into the engineering drawing and sent to the factory to manufacture it. The entirely manufactured and assembled substrate system is shown in Figure 36.



Figure 36: Manufactured and assembled substrate system with 4mm stainless steel plate and waiting for temperature testing

Most of the parts of the system are within the expectation and have been manufactured with good accuracy and follow the engineering drawing, except for some of the products, which are the covers for the heater part, the commercial ceramic heater and the ceramic fibre. The covers did not totally follow the drawing by the models since the bending of the aluminium 6061 plate is quite challenging. Thus, a little post-processing work has been done to fit the cover to the base and the plate. As for the ceramic heater, it has an inflated surface and needs extra grinding and polishing to make the upper surface flat surface to have a better connection to the plate to transfer the heat. Three types of ceramic fibre provided by different online sellers have been tested. One did not meet the expectations because it could not approach the temperature required for the testing and had a bad smell when heated to 150 degrees. Thus, one eligible ceramic fibre has been cut and filled in the heater part as the insulation layers. Also, the materials not mentioned in the model are the Honeywell PTM7950 Phase-change thermal conductive sheet and

0.05mm graphite paper. Both aim to provide better connections and transfer the heat. But in differences, the thermally conductive sheet is put between the water cooler and the base to help the cooler cool down the base. The graphite paper conducts heat better between the heater and the plate.

After assembling the whole substrate system, several tests were held to determine its heating speed and temperature control. The results, as well as the behaviour of different material plates during the heating test, will be shown in Chapter 4, Results and Analysis.

### 3.2. Whole Prototype Design

After building the substrate system and testing for working, the whole structure of the prototype should be redesigned since the previous structure only contained a wire feeder and was not concerned about the location of the substrate or the print head. The simple 3D modelling design is shown in the following Figure 37.

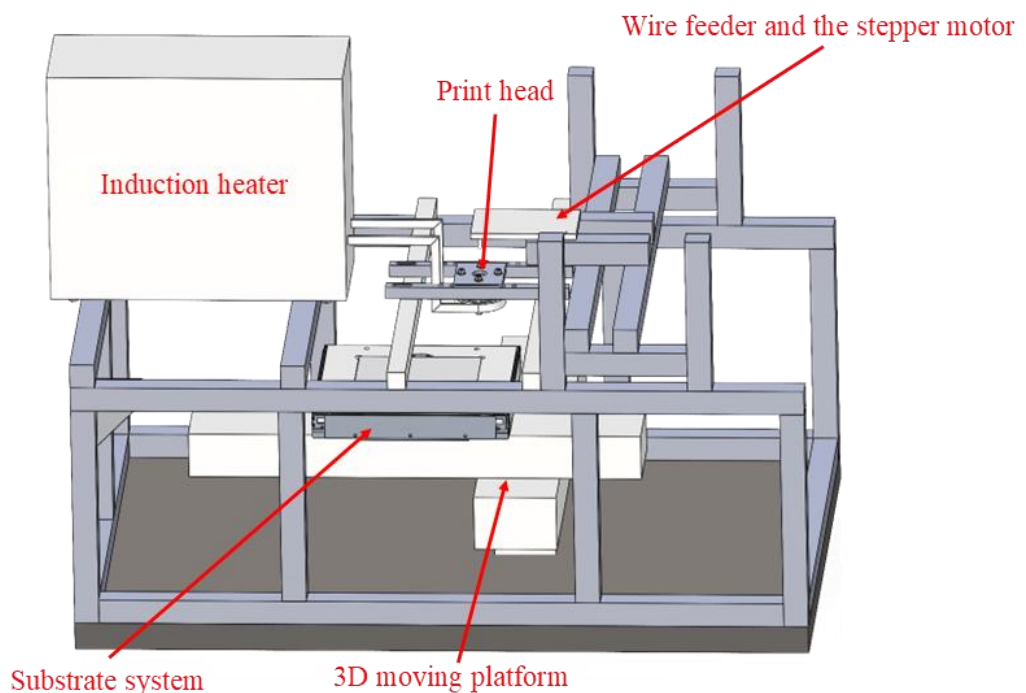


Figure 37: Schematic of the whole prototype system

This model contains all the parts' brief model, which is the same size as the actual parts but loses some details. The targets of this model are to determine the size of the whole structure and find the location of each part – the wire feeder and stepper motor, the print head, the induction heater, the substrate system and the 3D moving platform. The moving platform has been designed to be movable to check the intervention between the substrate system and the beam of the structure when the platform reaches the maximum range during its calibration process. The actual height of the whole machine will be higher because the bottom space of the platform has been deleted in the model, which contains the control system of the platform and ample space to store small parts and disposables.

All the grey bricks are the 4040 aluminium alloy profiles except the holder for the print head. The holders of the print head are made of quartz and machined by CNC to secure the top part of the print head. The white bricks are the 3030 aluminium alloy profiles. The lengths of the profiles are all based on the measurement in the model, but can be adjusted during the assembly process. The 4040 and 3030 profiles were chosen because they are easy to assemble and convenient to adjust. Different types of connectors, like the 90-degree angle connector, two-hole plate connector, etc., were used to connect and secure the whole structure. The final assembled prototype will be shown in the following Figure 38.

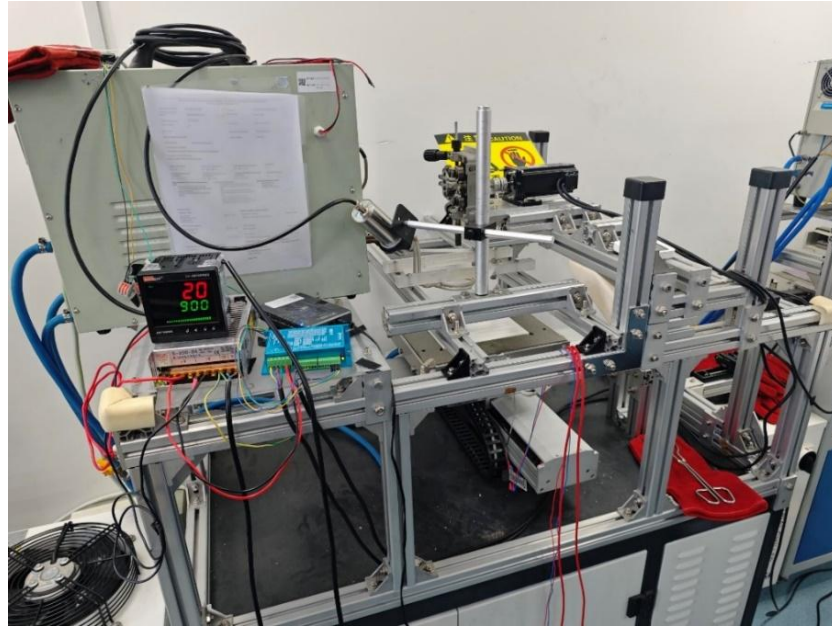


Figure 38: Manufactured prototype

As shown in Figure 38, the position of the wire feeder and the stepper motor differs from the model. The front 4040 profile holds them and has a considerable vibration that will affect the droplet produced during the printing process. Thus, two extra strong supports were added to strengthen the beam and reduce the vibration. Since these supports are extensive and take up space, the wire feeder and stepper motor increased by 40cm higher than the model exhibited. Also, a wire connects the whole structure and the ground to avoid the influence of electrostatic protection during the printing process. Also, the structure was secured by eight aluminium plate connectors at the corners, which can help clean the useless droplets and dust on the table of the 3D moving platform.

To help understand the whole system, a connection graph of the different equipment of the whole prototype system with different colour connectors is shown in Figure 39. A detailed explanation of the graph will be shown in the following paragraphs.

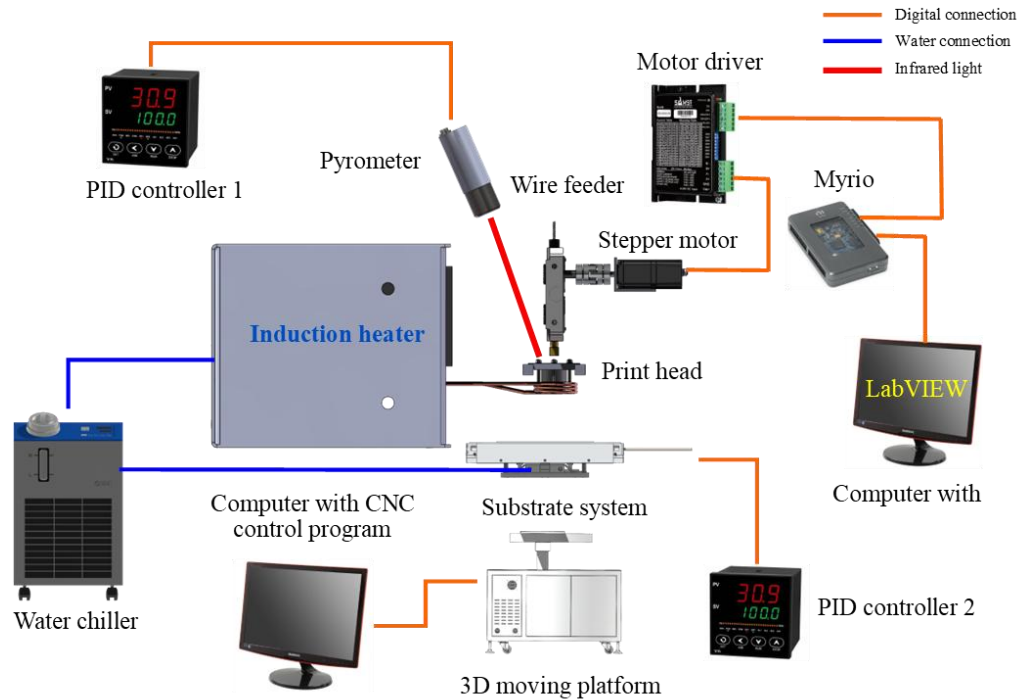


Figure 39: Connection of all equipment of the prototype.

In Figure 39, there are three different colours of connectors, each with its own meaning. The blue connector is the water connection of the prototype, and the orange connector is the digital connection of the prototype. The red connector is the infrared light from the pyrometer. The water chiller provides cold water to the induction heater and the cooler part of the substrate system. The power of the induction heater will be changed by turning the power knobs on the control panel. A pyrometer is used to measure the temperature of the graphite plate in the print head by red-fraud light, and a PID controller will transfer and display the temperature from the pyrometer. An NI Myrio transfers the command from the LabVIEW program on the computer to the motor driver. The motor driver actuates the stepper motor, and the stepper motor rotates the wire feeder to achieve the up-and-down movement of the aluminium wire to produce the droplets. A computer moves the position of the slider of the 3D moving platform by a CNC control program, and the substrate systems move with the slider. The other PID controller controls the

temperature of the substrate system by setting the temperature on the controller.

After the prototype had been built and tested for workability, the prototype printer printed some simple parts of the products, like the square and the word 'UNNC', as shown in Figure 40.

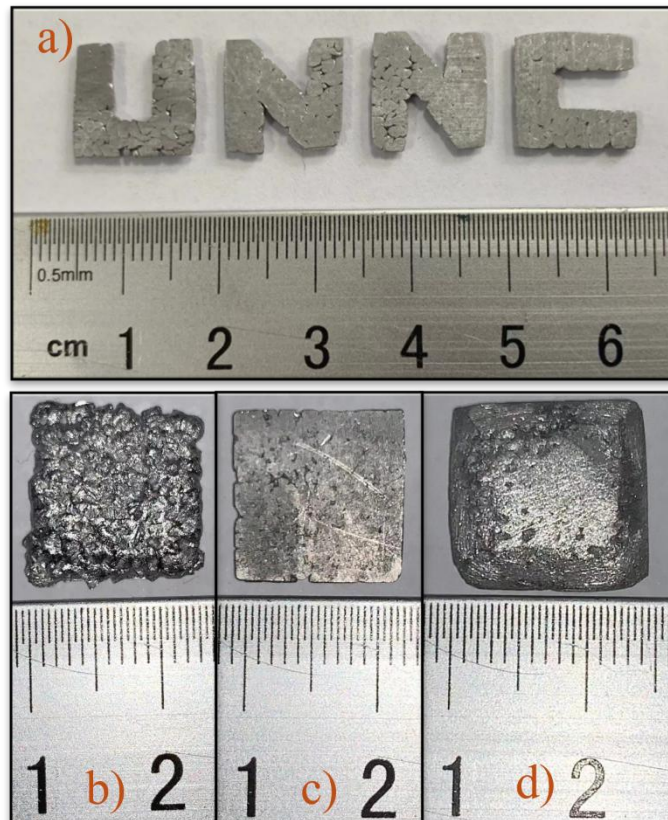


Figure 40: Printed products with the mica ceramic substrate system

The details of Figure 40:

- a) The substrate face of the printed metal 'UNNC' word.
- b) The upper face of the printed square.
- c) The substrate face of the printed square.
- d) The upper face of the printed cube after polishing.

The products show that the prototype can print aluminium 6061 parts,

which also means that the substrate system built is successful. However, the surface quality of the product still needs improvement, and the printed product is quite simple and small. The prototype still needs to be improved and developed in the future. The calculation and prediction of the droplet impact will be shown in the next section to better understand the droplet prototype produced. Three different types of experiments based on the calculation and prediction will be planned.

### 3.3. Calculations and Predictions of the Experiments

This section aims to provide a guide on how the droplet will behave based on the equations mentioned in the literature review section. Also, all the calculations will avoid the solidification of the droplet and have some assumptions to provide the data that cannot be measured.

Based on the Reynolds and Weber numbers, the initial velocity when the droplet impacts the surface is required. However, the high-speed camera can not be set in the system because of the lack of equipment and the design limit. However, the velocity can be calculated using the energy balance equation based on the droplet velocity from the nozzle. Nevertheless, the actual velocity still can not be measured. However, it can be estimated to assume the downward and upward movement of the wire as a simple downward movement. The Bernoulli's equation is

$$P_1 + \frac{1}{2}\rho V_1^2 + \rho g h_1 = P_2 + \frac{1}{2}\rho V_2^2 + \rho g h_2 \quad \text{Equation 4}$$

Assume the surface of the molten aluminium 6061 is the original surface, and the nozzle is the second surface. At the original surface, the liquid does

not have velocity; the extra pressure from the movement of the wire and the height is the distance between the surface to the nozzle, which is measured by the solidified wire using a calliper after the experiment. There is no extra pressure at the nozzle surface, and the distance is 0. So, the changed equation will be

$$P_{wire} + \rho g h_1 = \frac{1}{2} \rho V_{nozzle}^2 \quad \text{Equation 5}$$

The extra pressure of the wire can be regarded as an increase in the molten metal surface. The movement of the wire is caused by the wire feeder and the step set in the Labview program. So, the equation changes to

$$\rho g \frac{n_{step}}{400} \pi D_{wheel} + \rho g h_1 = \frac{1}{2} \rho V_{nozzle}^2 \quad \text{Equation 6}$$

Thus, the velocity when the droplet is squeezed out of the nozzle is

$$V_{nozzle} = \sqrt{2g \left( \frac{n_{step}}{400} \pi D_{wheel} + h_1 \right)} \quad \text{Equation 7}$$

The diameter of the wheel on the wire feeder is 28.4mm. And the measure  $h_1$  is 13mm for 800 degrees and 17.4mm for 900 degrees. Table 7 shows the transformation of different steps for different wire movements, the theoretical droplet volume, the theoretical radius of the sphere, and the initial nozzle velocity.

Table 7: Wire movement, theoretical sphere volume, theoretical sphere radius and the initial nozzle velocity based on steps

Step	Movement (mm)	Volume ( $mm^3$ )	Radius (mm)	Initial velocity (m/s)
1	0.223	0.448	0.475	0.489
2	0.446	0.897	0.598	0.494
3	0.669	1.345	0.685	0.498
4	0.892	1.794	0.754	0.503
5	1.115	2.242	0.812	0.507
6	1.338	2.691	0.863	0.511
7	1.561	3.139	0.908	0.516
8	1.784	3.588	0.950	0.520
9	2.007	4.036	0.988	0.524
10	2.231	4.485	1.023	0.528

Equations from the literature review were used to predict the splash. The K parameter equals 20, and 57.5 will be used as a limit for the transfer of the droplet behaviour, which is the red line in the graphs. The surface tension value is from Bao et al. [129].

$$\sigma = 1043 - 0.18T \quad \text{Equation 8}$$

The value of the kinematic viscosity of aluminium alloy is from Liao et al. [149]. The equation of the kinematic viscosity  $\eta$  will be

$$\eta = \eta_0 e^{\frac{E}{RT}} \quad \text{Equation 9}$$

Where  $\eta_0$  is the pre-exponential viscosity, R is the molar gas constant ( $8.3144 J \cdot mol^{-1}K^{-1}$ ), E is the activation energy for viscous flow, and T is the temperature whose unit is K. The factor  $\eta_0 = 0.149 mPa \cdot s$  and  $E = 13.08 kJ \cdot mol^{-1}$  is selected from Srivastav and Chaudhari [150] for the prediction of Aluminium 6061. And the dynamic viscosity can be calculated

by the kinematic viscosity [151]:

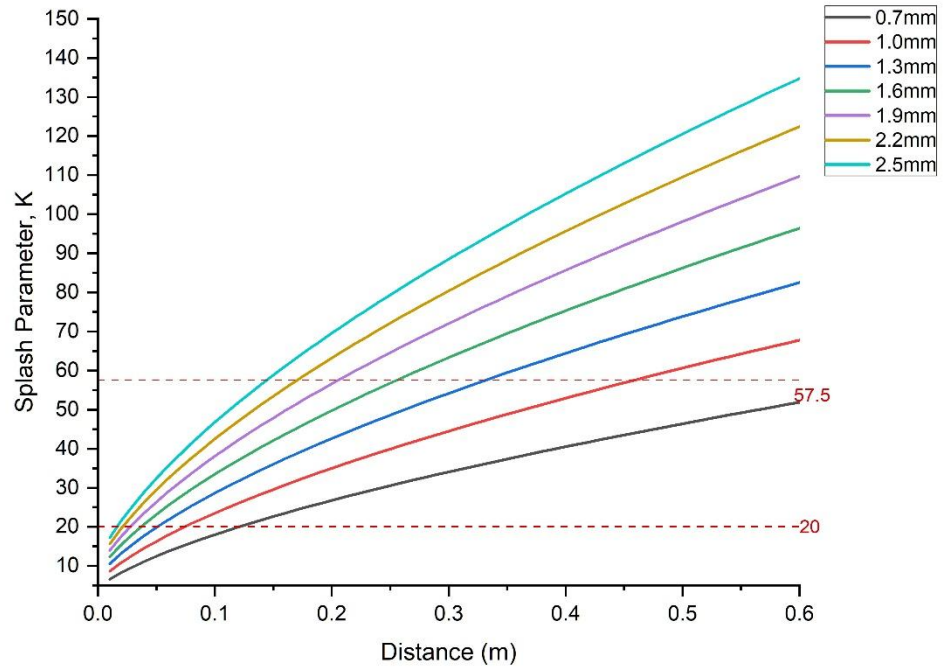
$$\eta = \frac{\mu}{\rho} \quad \text{Equation 10}$$

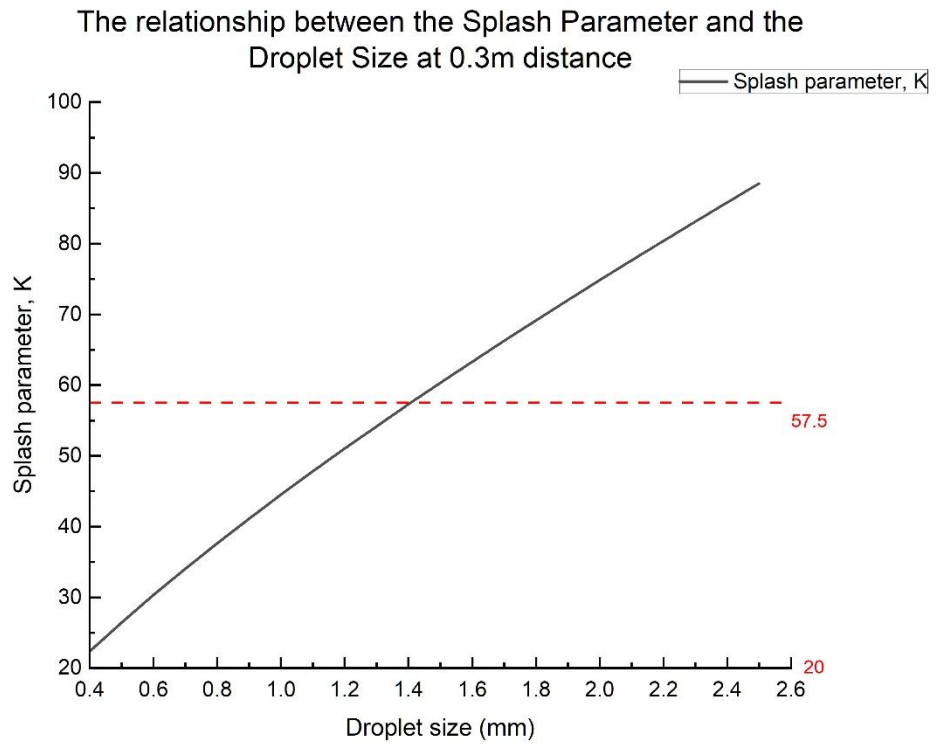
Based on these values and using Equation 1-3 and Equation 9-11, the K value was

$$K = \sqrt{\frac{2700 \times V_0 D}{1043 - 0.18T}} \times \sqrt{\frac{V_0 D}{0.149 \times e^{\frac{13.08}{8.3144 \times T}}}} \quad \text{Equation 11}$$

By inserting the changing parameters (temperature, distance between nozzle and substrate, and droplet sizes), the K parameter can be predicted. The prediction graph with different nozzle-substrate distances, droplet sizes, and droplet initial temperatures will be shown in Figure 41.

The graph of the relationship between the splash parameter and the distance for different droplet sizes at 800°C droplet temperature





The relationship between the Droplet initial temperature and Splash parameter for different droplet sizes at 0.3m

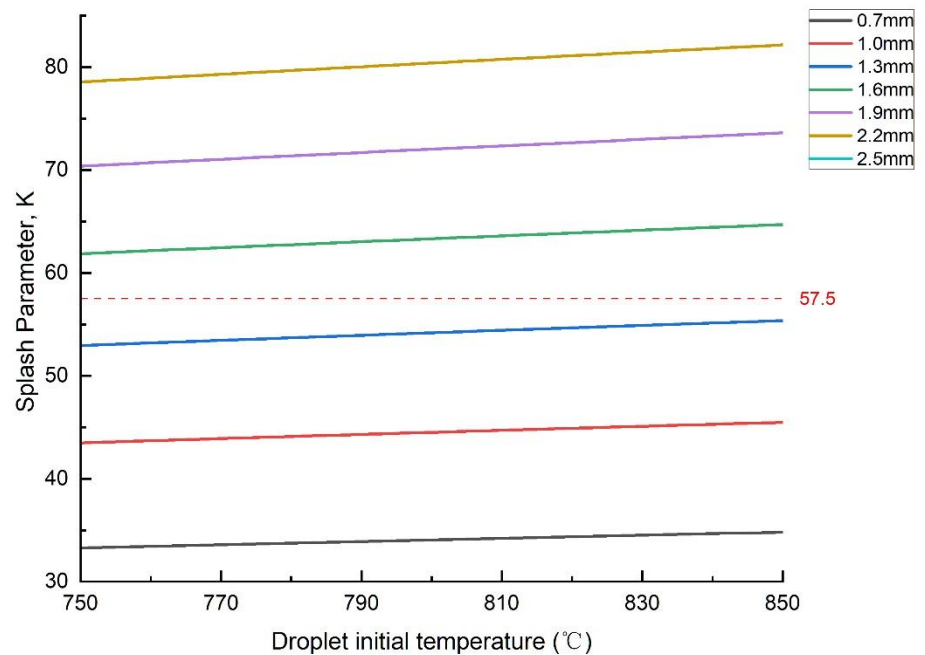


Figure 41: Prediction of the K parameter changed by droplet sizes, the distance and the droplet temperature

As shown in the graph, the initial temperature of the droplet will not

significantly affect the K parameters. However, the droplet sizes and the distance between the nozzle and the substrate plate have a significant influence on the K parameters. 750 degrees and 850 degrees are used in the temperature graph because the previous test of the droplet temperature is around this range, which can provide a fluent droplet production. Since  $K=20$  is the range, droplets will start to splat, and tiny droplet sizes cannot be reached based on the recent printhead. The droplet will splat randomly during the experiment. Thus, the droplets will be selected after the printing process.

The following section is the experiment arrangement, which includes the equipment, sample preparation, and the experiment plans based on the calculation and the literature review.

### **3.4. Experiment arrangement**

#### **3.4.1. Introduction**

In this section, the experiment setup will be introduced. There will be three different experiments: the distance between the nozzle and the substrate, the surface roughness, the substrate surface temperature and the substrate material. Before the experiment is explained, the material preparation and the equipment introduction will be mentioned and introduced. After the material and equipment are ready, the detailed steps of the experiment will be explained.

#### **3.4.2. Material Preparation**

Based on the literature review, three different materials have been decided to test for the comparison of each behaviour to choose a suitable material as the substrate plate material of the metal droplet extrusion technique. The materials used are copper, stainless steel, and aluminium oxide ceramic.

For the specific material trademarks, the T2 purple copper, the 304 stainless steel alloy and the 95 aluminium oxide ceramic have been chosen. Because all of them are commercial products and can be approached very easily in the daily market, such as Taobao or Alibaba, these materials are relatively cheap when bought in commercial sizes. For instance, the TU1 copper is the oxygen-free copper with a purity of  $\geq 99.97\%$  [152]. The price of 4\*310\*310mm is 700 yuan, compared to the T2 purple copper, which is 275 yuan and is the same size. The 4\*310\*310mm 99 aluminium ceramic plate needs to be customised and requires 1500 yuan per piece, but the commercial 95 aluminium oxide ceramic plate for the size of 4\*200\*200mm will be 100 yuan. But, for the stainless steel, the price is relatively low, and the cost of a 4\*310\*310mm size is 93 yuan because of the wide range of use and simple cutting method. Going back to the purpose of the technique, a relatively low cost in the consumable materials is necessary for the users, as the target population of this technique is personal users. Low cost will also be popular in the industry production.

After the material is chosen, different shapes and post-processing of the material are needed, which will be shown in Table 8. The detailed elements of the materials will be shown in Table 9.

Table 8: Different types of material plate preparation

No.	Material	Size (mm)	Number	Post-processing
1	T2 Purple copper	200*200*4	1	100 mesh sandblasting
2	304 Stainless steel	200*200*4	1	100 mesh sandblasting
3	95 Aluminium oxide	200*200*4	1	None
4	T2 Purple copper	110*50*4	5	Sandblasting and polishing
5	304 Stainless steel	110*50*4	5	Sandblasting and polishing
6	95 Aluminium oxide	100*100*4	5	Grinding and polishing

Table 9: Detailed elements of the material

Material	Element	Manufacturer
T2 Purple copper	Cu 99.98%, Bi 0.00045%, Sb 0.00097%, As 0.00056%, Pb 0.0011%, S 0.0014%	永圣五金
304 Stainless steel	GB/T 20878-2007 304 stainless steel	泰州市睿灿金属制品有限公司
95 Aluminium oxide	95% aluminium oxide and 5% yttrium oxide	茜恩旗舰店

Plates No. 1, 2, and 3 are used for temperature experiments, and they should have quite the same surface roughness and cover the space that remains in the mica plates. For copper and stainless steel plates, 100 mesh sandblasting will increase the original surface roughness of both plates and have a close roughness to that of the ceramic plates. The material for sandblasting is white corundum and in 2 bar pressure.

For No. 4 and 5, the size of the corundum used for sandblasting will be increased from 12 mesh to 100 mesh (12 mesh, 24 mesh, 60 mesh and 100 mesh) at the same pressure to get different decreasing surface roughness. AUTOSUL metal polish cream is used to polish two metal plates to remove the dirtiness on the surface and achieve a smooth surface. The prepared plates will look like in Figure 42. The surface roughness of these plates is from 12.9 to 0.0292 $\mu$ m, depending on the material and the corundum sizes. For 95 aluminium oxides, the hardness of this material is so high, and it is hard to change its surface roughness (around 2 micrometres through the literature). So, for No.6, different meshes of the diamond sandpaper are used to grind the plates using the YUZHOU grinding and polishing machine. The mesh will be 60 mesh, 180 mesh and 600 mesh, which will result in a decrease in the surface roughness. As for the other two plates, one will not be ground, and the other

will be polished with 3000 mesh silicon carbide sandpaper, resulting in the smallest surface roughness among all the ceramic plates used for the surface roughness experiment.

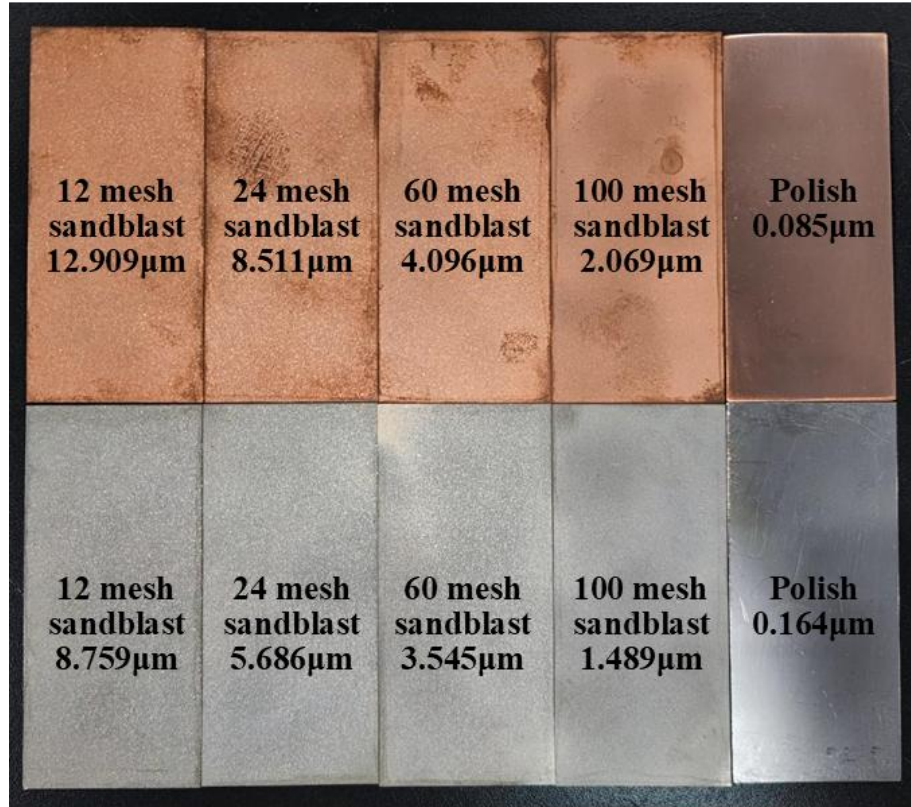


Figure 42: Sample copper and stainless steel plates with different surface roughness

The surface roughness was measured by the MarSurf GD 120 roughness meter from the Mahr company with the selected Ra mode, which is the average roughness of the test plate. Each plate was measured at the centre three times, and the average of the three results was taken. The detailed values of the surface roughness of the sample plates with different materials and post-processing methods will be shown in Table 10.

Table 10: Surface roughness of the sample plates with different post-processing methods and materials

Material	Post-processing	Surface Roughness ( $\mu\text{m}$ )
T2 Copper	12 mesh sandblast	12.909
	24 mesh sandblast	8.511
	60 mesh sandblast	4.096
	100 mesh sandblast	2.069
	Polish paste	0.085
304 Stainless steel	12 mesh sandblast	8.759
	24 mesh sandblast	5.686
	60 mesh sandblast	3.545
	100 mesh sandblast	1.489
	Polish paste	0.164
95 Aluminium oxide	None	1.293
	60 mesh Grind paper	1.019
	180 mesh Grind paper	0.984
	600 mesh Grind paper	0.752
	3000 mesh Grind paper	0.665

The droplet material is commercial aluminium 6061 wires, which the project provided during the previous procurement. Before the wire is inserted into the wire feeder, the Line adjuster should straighten it.

### 3.4.3. Equipment Preparation

After the prototype printer is built, some extra equipment should be used during the experiment and the measurement process. This equipment will be divided into two groups: hardware and software.

#### Hardware

1. A UTI 260B infrared thermal imager with a derrick crane will be used to measure the plate surface temperature since the heater controller only controls the temperature of the ceramic heater. Thermocouples have been

tried using different connect positions. Still, because of the problematic place position, the measurement from the thermocouple is not accurate or can be said to be far away from the actual temperature. Thus, thermocouples are not considered to be the equipment to measure the surface temperature.

2. The Canon EOS C70 camera with a macro lens will be used to take pictures of the produced droplets and transfer them to the computer for further analysis.
3. A pair of high-temperature gloves and crucible pliers will be used to move the hot sample plate because the heat from the print head will transfer to the sample plates, and the coil will also induction heat the plate a little bit. This preparation is to protect the safety of the researchers.

### **Software**

1. MATLAB is used to remove the distortion from the pictures taken by the camera lens. A calibration board will first be used to take around 25 different photos, which will be put into the Camera Calibration App in MATLAB to produce the camera's parameters. Then, the `undistortImage` function, which is in MATLAB, and the parameters produced by the calibrator app will be used to remove the picture's distortion automatically.
2. LabVIEW will be used to control the stepper motor, which connects to the wire feeder. A detailed view of the program will be shown in Appendix 3. The principle of the program is to control the Myrio to imitate the PWM pulse and send it to the driver of the stepper motor to actuate the stepper motor—the change of the duty cycle of the pulse to control the speed and distance of the wire.
3. A CNC software called X5 CNC111, loaded into the computer of the 3D moving platform, is used to control the substrate's position and movement.

The simple G code program is created and run on the software to make the substrate stop at different positions to catch the droplet from the nozzle. A G code example will be shown in Appendix 4.

- 4 The software Camera Measure measures the contact angle of the final picture (4096 x 2160 pixels) post-processed by MATLAB. Because the measurement was done manually, an artificial error of  $\pm 2^\circ$  will be added to the final results.

#### **3.4.4. Experiment Plan**

Previous sections talked about the material and equipment preparation, and this section will discuss the steps of the experiment. Based on the literature review section, three different types of experiments have been decided and processed to study the effect of distance, substrate temperature and substrate surface roughness on the contact angles of the droplets. Also, three different materials will be compared to select the best material to use as the substrate plate material. A brief flowchart of the experiment steps will be exhibited in Figure 43, and a detailed explanation will be provided in the following paragraphs, including the differences between the experiments.

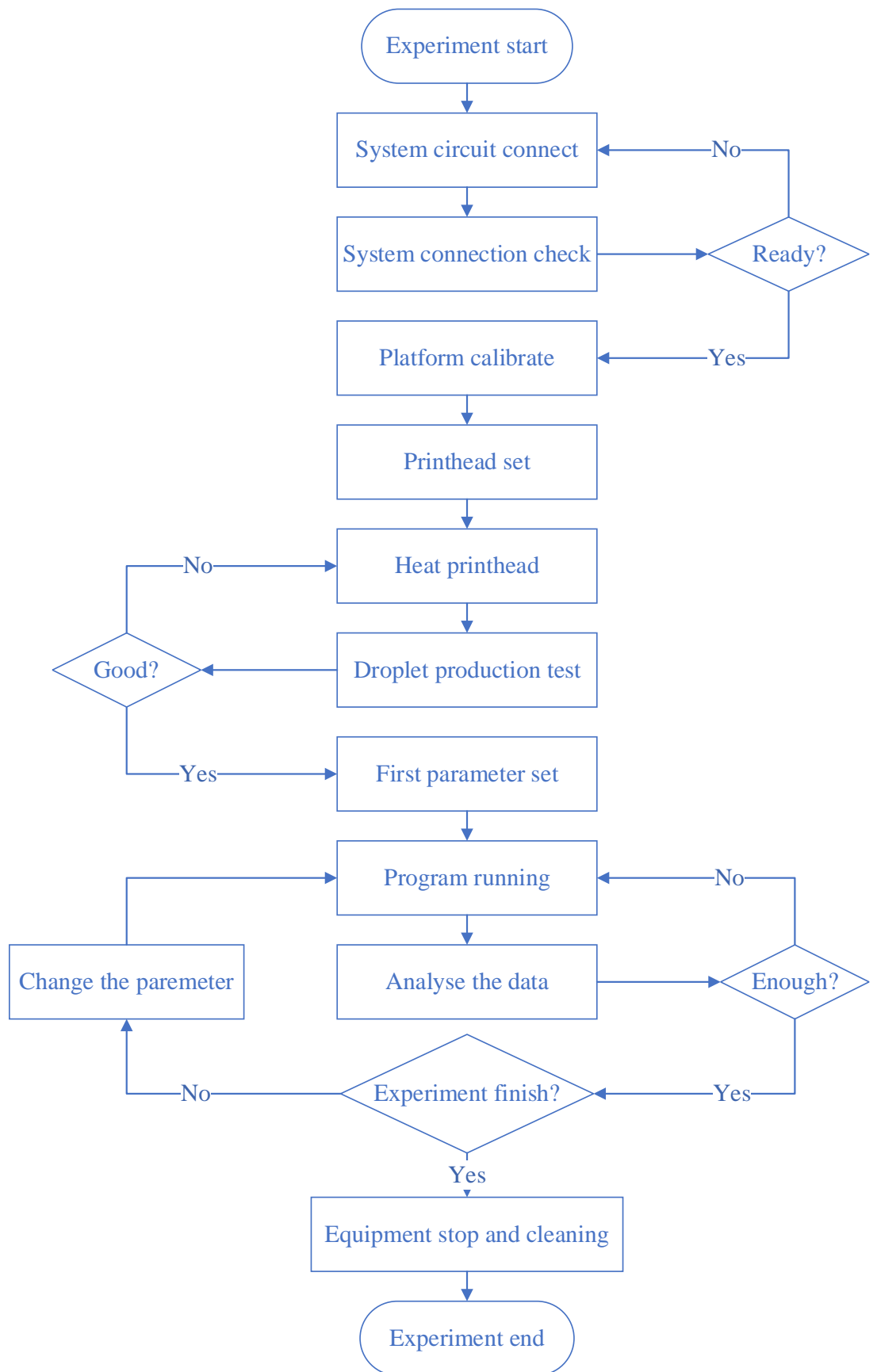


Figure 43: Flow chart of the experiment

The following paragraphs explain the flow chart and indicate what needs attention when experimenting.

- 1) System circuit connects and system connection checks: all the equipment will be connected and checked for safety issues.
  
- 2) Platform calibration: Calibrate the 3D platform for the zero point of the 3-axis using the software's auto-calibration process. It's essential to ensure that the printhead is not settled during this calibration process, as it may damage both the printhead and the substrate plate. The substrate plate will hit the printhead when the platform reaches the Z limit.
  
- 3) Printhead set: Assemble the different pieces of the printhead and secure it with the ceramic screws and nuts with a bare hand until the nut cannot be tightened more. Tightening the nut with tools may destroy the screws and the main body of the print head. Then, secure the print head at the holder with four stainless steel screws. Finally, insert the wire until it touches the hole of the nozzle and lock it with the wheels of the wire feeder.
  
- 4) Heat print head: First, turn on the chiller and verify that water flows through the pipe in both the induction heater and the cooling plate of the substrate. Failure to provide water flow may result in an error from the induction heater. Then, turn on the parameter and place the printhead in position in this step. Ensure that the red pot from the parameter points to the surface of the graphite in the printhead. Additionally, set the desired temperature in the PID box, which controls the opening and closing of the induction heater. Finally, turn on the induction heater and adjust the power output. The power output will only affect the maximum temperature and

the rate at which the printhead heats up.

5) Droplet production test: First, open the LabVIEW program on the laptop, which controls the production of the droplets. Then, wait for the temperature of the printhead to stabilise. This can be determined by observing the number on the display of the parameter on the PID box. The temperature should remain steady or vary within a range of 4-5 degrees above or below the set temperature. After that, fill in the parameters in the LabVIEW program that control the size and number of droplets. Ensure that the parameters match those defined for the experiment. Finally, using tongs, place a test plate under the print head. This plate will catch the test droplets and allow observation without interfering with the experiment plate. Begin producing droplets until the production becomes continuous. The droplets should be uniform in size, and there should be no missing droplets during the production process

6) First parameter set: it will be different from the experiments

- For the distance experiment, control the platform and move the substrate plate at the position of 20mm from the nozzle. Then, place the smooth sample plate.
- For temperature experiments, move the substrate plate at the position of 45mm from the nozzle. Then, place the first sample plate (smooth plate) on the substrate system
- For roughness experiments, move the substrate plate at the position of 45mm from the nozzle. Then, the PID controller of the substrate should be set at 50 degrees and wait for it to be at a stable position.

- 7) Program running: Start the program on the CNC control program first and then start the LabVIEW program to produce the droplets. Wait until the platform stops moving.
  
- 8) Analyse the data: Check the droplet caught on the sample plate and clarify whether it is good to use or not. If the droplet on the sample plate does not meet the amount requirement (at least 5 droplets are good to use), rerun the program to get more droplets. If the droplet number is enough, the sample plate can be changed.
  
- 9) Change the parameter: First, the material of the sample plate will be changed, and then the different parameters will be used in each experiment. For the distance experiment, the platform will leave the nozzle further. For the roughness experiment, a rougher sample plate will be placed. The PID controller will be set to a higher temperature for the temperature experiment.
  
- 10) Equipment stop and cleaning: After an experiment has been done or the wire is bent, the whole experiment will be finished. It should follow the following steps:
  - i. Stop the induction heaters and allow sufficient time for the droplets and the plate to cool down. Since the final production has just been completed, the original temperature of the droplets may be as high as 900 degrees. Waiting for them to cool down is crucial to protect the researchers from the high temperatures.
  - ii. Store the droplets in a sample box to protect them.

- iii. Verify that all machine components have cooled down. If any components are still hot, allow more time for them to cool down, as the remaining heat could impact or damage the components.
- iv. Shut down all equipment.

After the experiments and the droplets are collected, the measurement will be processed by following steps:

- a) Pick the droplet and place it on the platform in front of the camera with the microlens, ensuring they are in a proper position.
- b) Take clear photos of each droplet, focusing on the corner of the droplets. Save the images and transfer the picture to the computer.
- c) The MATLAB code will deal with the distortion of the picture.
- d) Image measurement software will be used to measure the contact angles of the droplets, and the measurements will be recorded manually in Excel.
- e) The measurement will be transferred to the graphs and tables for further Excel analysis.

After all the previous steps, the experiment can be regarded as finished. The results and analysis of the experimental data will be shown in the next section, as will the discussion of the behaviour of the droplet impact on the different sample plates.

## Chapter 4 Results and Analysis

### 4.1. Substrate temperature experiment

#### 4.1.1. Substrate System Test and System Adjustment

At first, three experiments about different materials were carried out to check the system's working condition (the stability and the maximum temperature) and analyse the drawbacks to find a better choice of plate material. Thus, the 310mm x 310mm x 4mm plate of T2 high-purity copper (copper content  $\geq 99.90\%$ ), 304 stainless steel and 95 Aluminium oxide ceramic plate was prepared as the substrate plate to observe how the temperature would change for the plate and the heater. The Uti160S infra-red thermograph and EM1500 infrared thermometer will measure the temperature. The accuracy of the Uti160S infra-red thermograph is  $\pm 2^{\circ}\text{C}$  (when an error is less than  $2^{\circ}\text{C}$ ), or  $\pm 2\%T$ . The accuracy of the EM1500 infrared thermometer is  $\pm 2^{\circ}\text{C}$  when the temperature is  $0^{\circ}\text{C}\sim 23^{\circ}\text{C}$ ;  $\pm 1.5^{\circ}\text{C}$  or  $\pm 1.5\%T$  (choose the higher one) when the temperature is  $23^{\circ}\text{C}\sim 500^{\circ}\text{C}$ ;  $\pm 3^{\circ}\text{C}$  or  $\pm 3\%T$  (choose the higher one) when the temperature is higher than  $500^{\circ}\text{C}$ .

The thermal graph will directly measure the plate temperature. To have a more accurate temperature at the different locations of the plate, several graphite pieces with numbers are placed on the plate. The thermometer will directly measure the temperature of the graphite rather than the plate, since copper and stainless steel will reflect the infrared light, which causes an inaccurate measurement in the meters. The location of the graphite will be shown in Figures 44-50. The graphite at the corner was used to detect the edge plate temperature and show the heat dissipation of the plate. The corners have been included for the measure because they do not directly touch the heater,

but there will also be a place where the droplets will be located according to the design purpose. Thus, the corner was expected to be heated at the same temperature as the centre of the plate or slightly lower than the centre temperature (lower than 30°C). This was one of the reasons copper and stainless steel have been selected.

Each material will be tested at least twice, a low-temperature and a high-temperature test. However, this section will only show the results of the high-temperature test because the low-temperature test aims to check the system. The temperature will be set in the controller, and a stable time will be provided to keep the temperature stable. The following temperature will be set after the plate's temperature remains the same. A K-type thermocouple will measure the heater's temperature, as shown in Section 3.1.3. The accuracy of this thermocouple is  $\pm 2.5^{\circ}\text{C}$  or  $\pm 0.75\% \text{ T}$ .

The temperature set of the PID box was different for the materials and the times in these tests. Because of the different heat conductivity of the materials, the temperature set will be increased from a low temperature to a high temperature and then wait for a little time at each temperature set to make the plate temperature equal to protect the test plate, especially the ceramic plate. These tests aim to find the maximum temperature of the different materials and test whether the substrate system can keep a stable temperature so that the temperature set on the PID will not affect the results of the tests.

For the T2 copper plate, the temperature was first set from 200°C to 350°C in steps of 50°C. For the 304 stainless steel plate, the temperature was raised from 200°C to 700°C in the first two steps of 200°C, and the final step is 100°C. For the 95 ceramic plate, the temperature set was low since the ceramic will easily break due to the uneven heat. The temperature set was from 50°C to 200°C in steps of 50°C. The following figures (Figures 44-46) show the pictures of the first three test plates and the graphite. The temperature-time

graph will be shown in Figures 44-46.

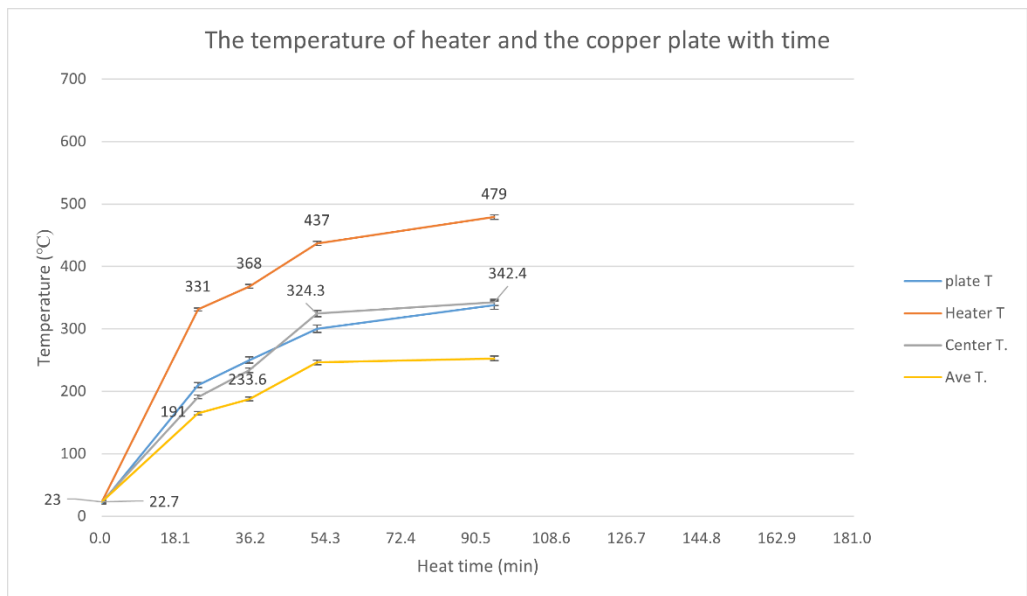
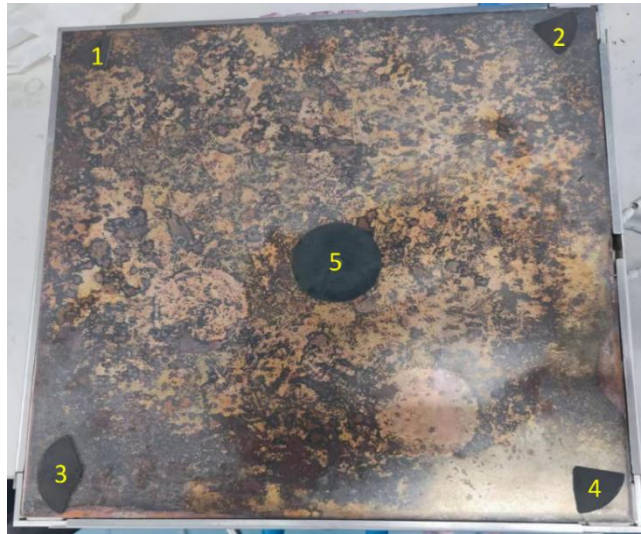


Figure 44: The experiment set and results graph of the T2 copper plate temperature test

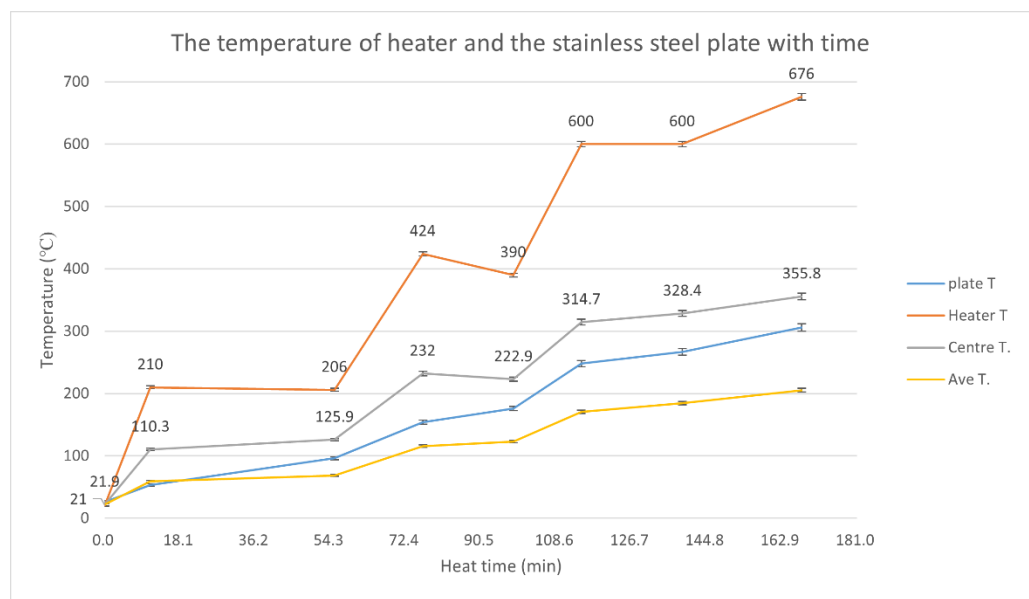
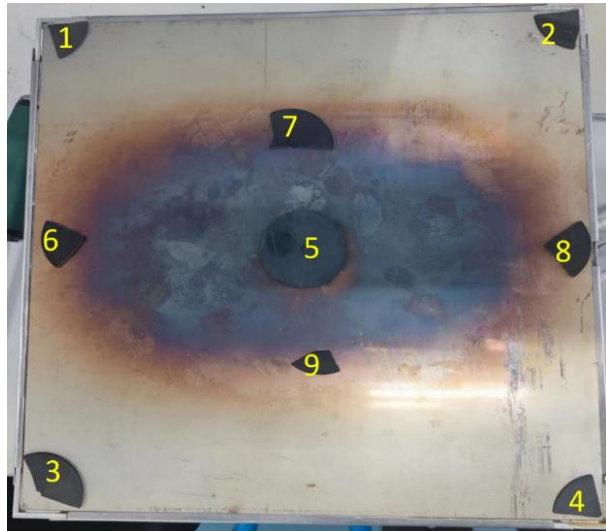


Figure 45: The experiment set and results graph of the 304 stainless steel plate temperature test

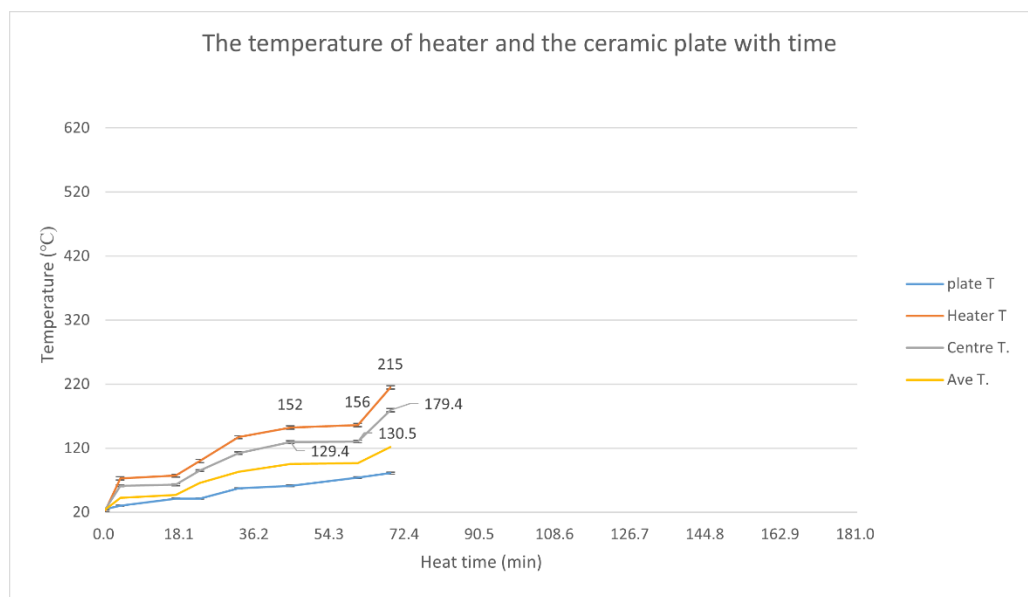
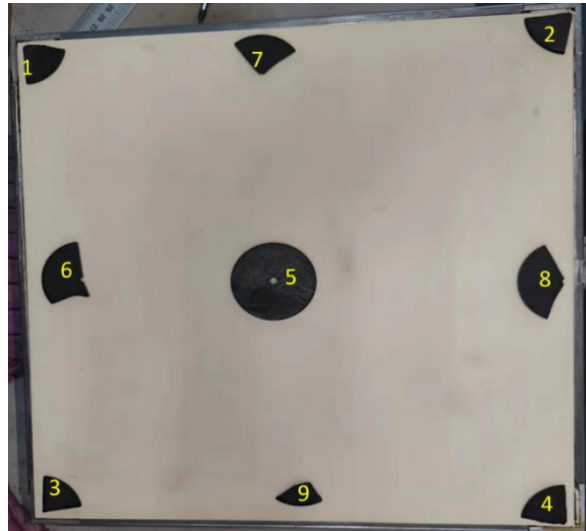


Figure 46: The experiment set and results graph of the 95 Aluminium oxide ceramic plate temperature test

According to the experiments' results, the big plates do not fit the substrate system since the heater does not touch the whole plate, which causes enormous differences in the temperature of the plate's centre and the plate's corner. Those differences caused the metal plate to bend and the ceramic plate in Figure 46 to break; also, the copper plate was heavily oxidised, and the centre of the stainless steel plate was partly oxidised, which can be seen in Figure 44 and Figure 45. Meanwhile, the difference between the heater, centre, and corner temperatures was more significant than expected. The choice of

copper and stainless steel as the plate material was based on the material chosen in the literature review section and the metal's high conductivity, which is expected that temperature differences would not be high (lower than 30°C).

However, the deformation, the oxidation and the high-temperature differences (over 150 °C between the heater and the plate) show these materials are not the materials that should be used for the MDE technique, especially in the air. Nevertheless, the ceramic plate exceeded the expectation that the temperature rise was quick, and the differences (36°C) were minor, although it broke at a low temperature. To examine the reliability of the small ceramic plate, two more experiments were done based on the broken piece of the previous big ceramic plate before the commercial small-size ceramic plate was ordered. The following Figure 47 and Figure 48 show the experiment's setting and the results graphs.

For the break piece ceramic experiment, the temperature was increased from 100°C to 500°C in steps of 100°C. For the copper in the middle experiment, the temperature was set from 200°C to 600°C in steps of 200°C.

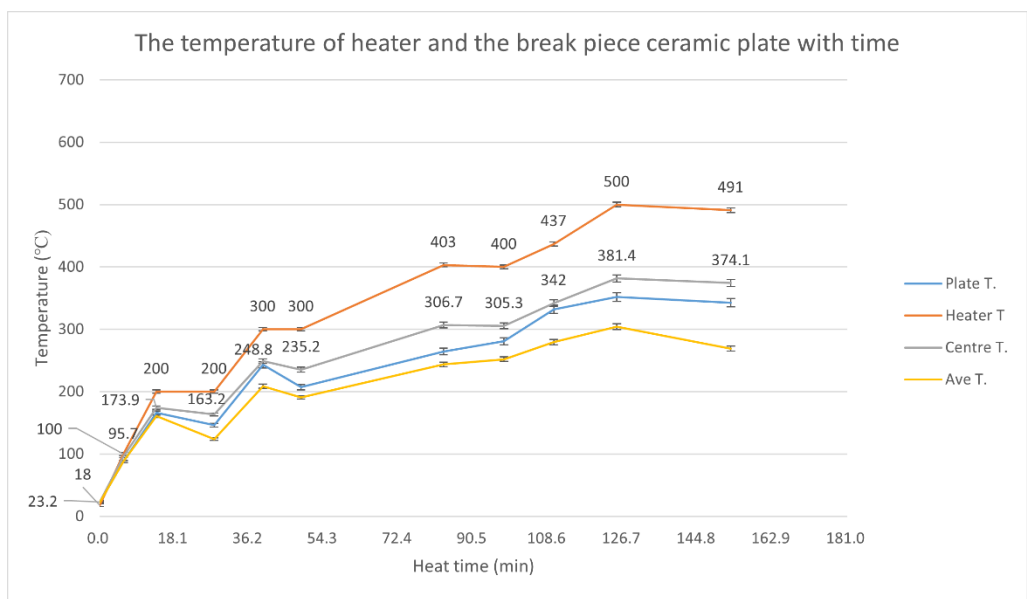
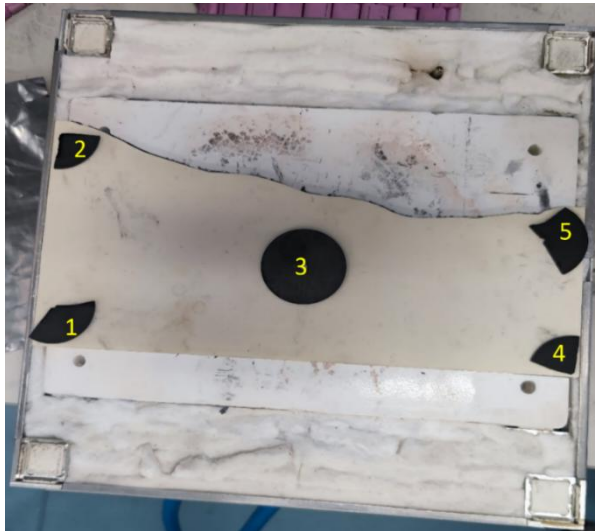


Figure 47: The experiment set and results graph of the pieced ceramic temperature test

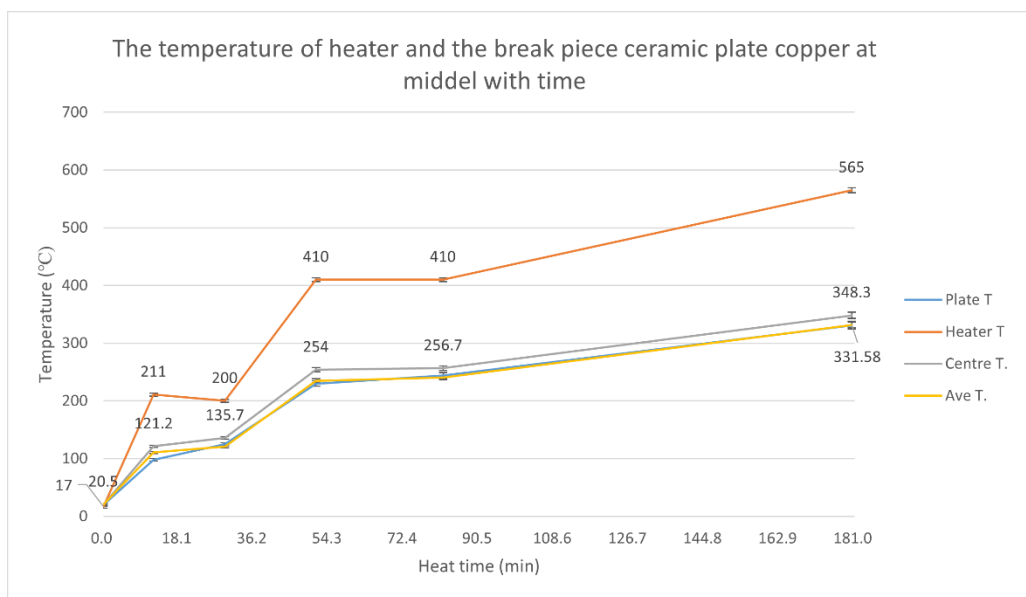


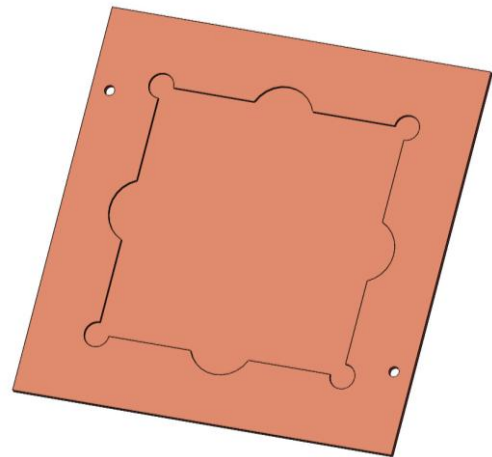
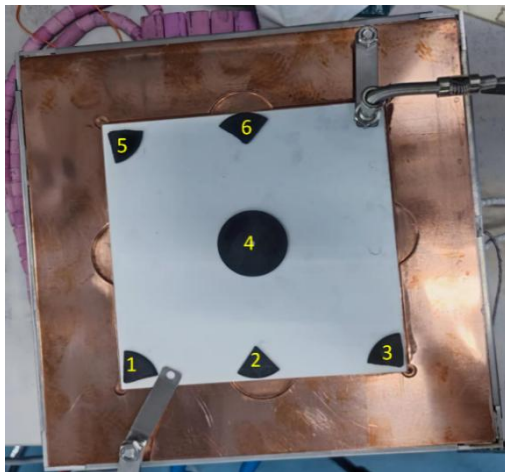
Figure 48: The experiment set and results graph of the pieced ceramic and cooper in the middle-temperature test

In the first broken-piece experiment (Figure 47), the ceramic piece decreased the difference between the heater and the plate (around 120°C) and a better heat dissipation. However, because of no insulation at the top, the heater was exposed to much heat in the air, causing the maximum heater temperature to be slightly lower compared to the previous stainless steel experiments but still higher than the copper experiment. Therefore, a big copper plate was placed between the heater and the broken ceramic piece to reduce the heat loss from the heater and transfer heat to the ceramic piece,

which is shown in Figure 48. The copper plate increased the maximum heater temperature and narrowed the differences in the plate temperature. However, the time cost of this setting was long because the conductivity of the copper was too high, which made the copper plate a big air cooler in the experiment.

Hence, a designed copper plate and a 20cm x 20cm x 4mm 95 alumina plate have been used to seek a better performance than the previous experiment. The ceramic plate will be inserted into the holes in the copper plate, and the copper plate will be put on the heater, as shown in Figure 49. The hollow of the copper plate will help to secure the position of the ceramic plate when the platform is moving. Also, it is convenient for the users to replace the used ceramic plate with this designed copper plate.

The temperature was set as 150°C, 300°C and 500°C.



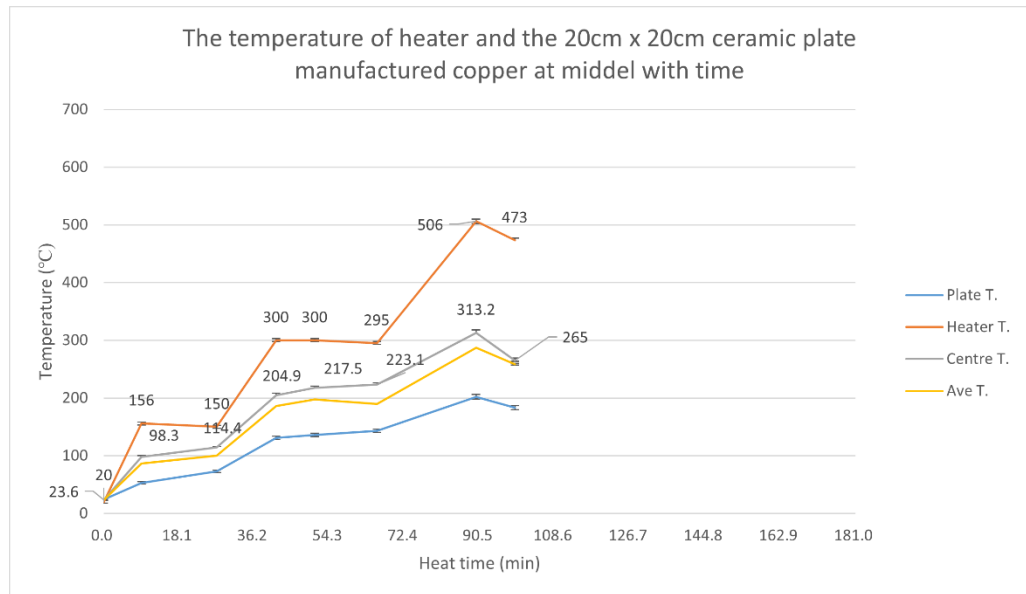


Figure 49: The experiment set and results graph of the Ceramic and manufactured copper plate temperature test

The newly designed copper plate provided a less uniform plate temperature but had a narrower difference between the heater and the plate.

However, it still does not meet the requirements of the plate temperature in the previous requirement table, which should reach 500 degrees. Hence, a new material, black golden mica, can get a temperature of 1400 degrees, but the thermal conductivity is 0.42 to 0.67 W/ (m·K), which has a suitable heat insulation property. So, a manufactured mica plate was used to secure the ceramic plate and keep the heat from the heater, as shown in Figure 50. The temperature was set from 100°C to 500°C in steps of 100°C.

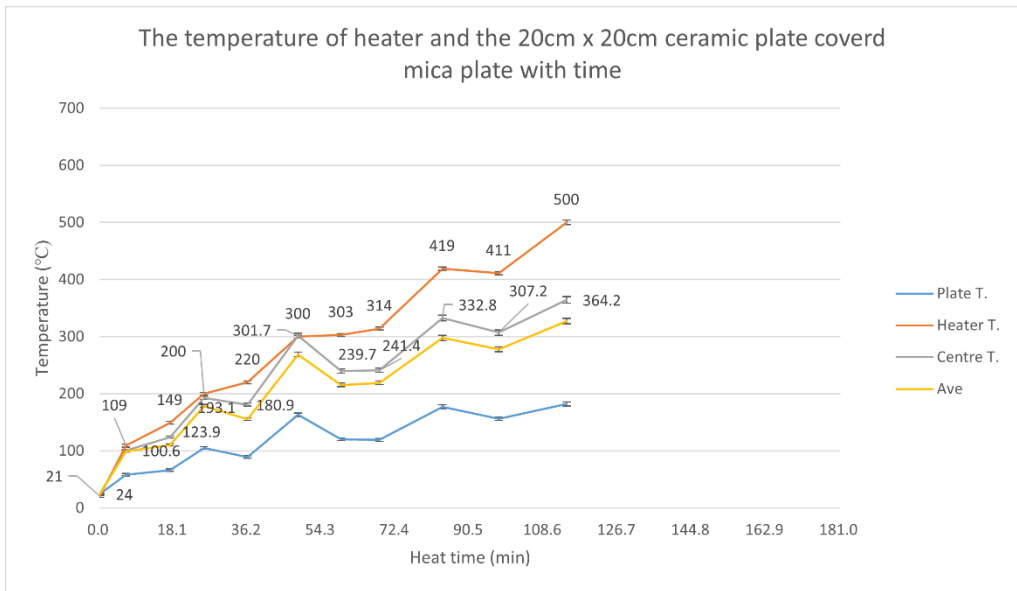
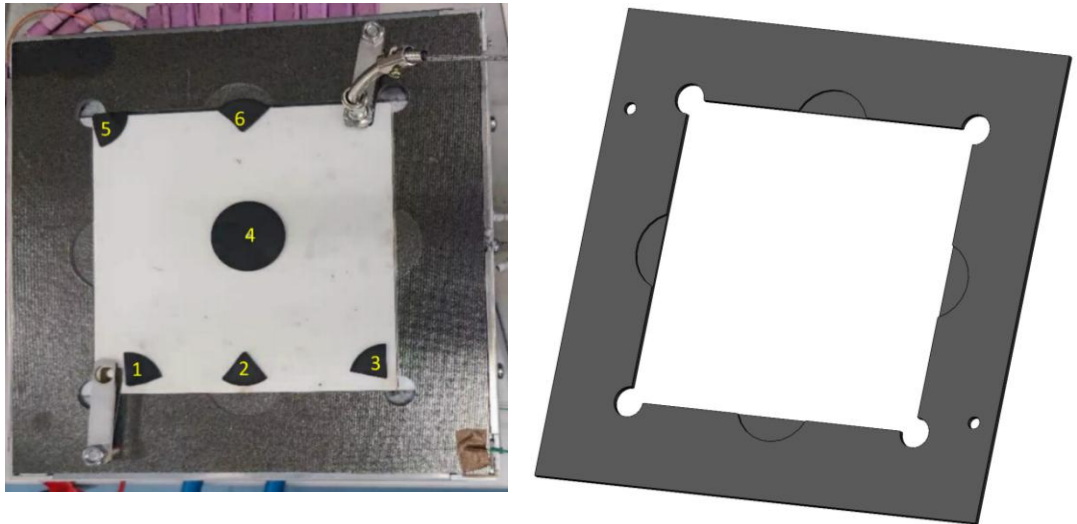


Figure 50: The experiment set and results graph of the Mica cover with ceramic plate temperature test

The mica plate was good at insulating the heat and helping to decrease the differences between the heater and the ceramic plates. The temperature was more uniform across the whole plate.

To better compare the performance of four materials or material sets (copper, stainless steel, ceramic with copper and ceramic with Mika), a series of experiments have been carried out at the same heat rate to compare the maximum temperature. Also, an experiment with the ceramic and Mika set in

which the heater directly connects to the power without the PID box, has been done to test the limit heat speed and the maximum temperature the substrate system could reach. The following 4.1.2 section will show all the detailed results, graphs, and discussions. According to the results, the ceramic + Mika plate has the same heat accumulation for the heater as the stainless steel plate, but can reach a higher plate centre temperature. Also, it will not oxidise and bend at high temperatures. With a maximum power input, the highest temperature reached 534.3°C, which approaches the requirement but is slightly lower than the expected temperature (550°C).

#### **4.1.2. Comparison of different substrate materials**

These experiments were tested to compare the maximum temperature and heat speed for the T2 copper, 304 stainless steel, ceramic with copper, and ceramic with Mika at the settled heating rate, for which the PID box was set at 600°C. The set of each experiment will be shown in Figure 51. Figure 52 and Figure 53 show the conclusive results. Also, a further experiment was run to test the maximum plate surface temperature without controlling the PID box (full power). The result is shown in Figure 54.

The surface roughness of the different material plates was

- T2 copper: 0.1581µm
- 304 stainless steel: 0.2789µm
- 95 alumina ceramic: 1.4204µm

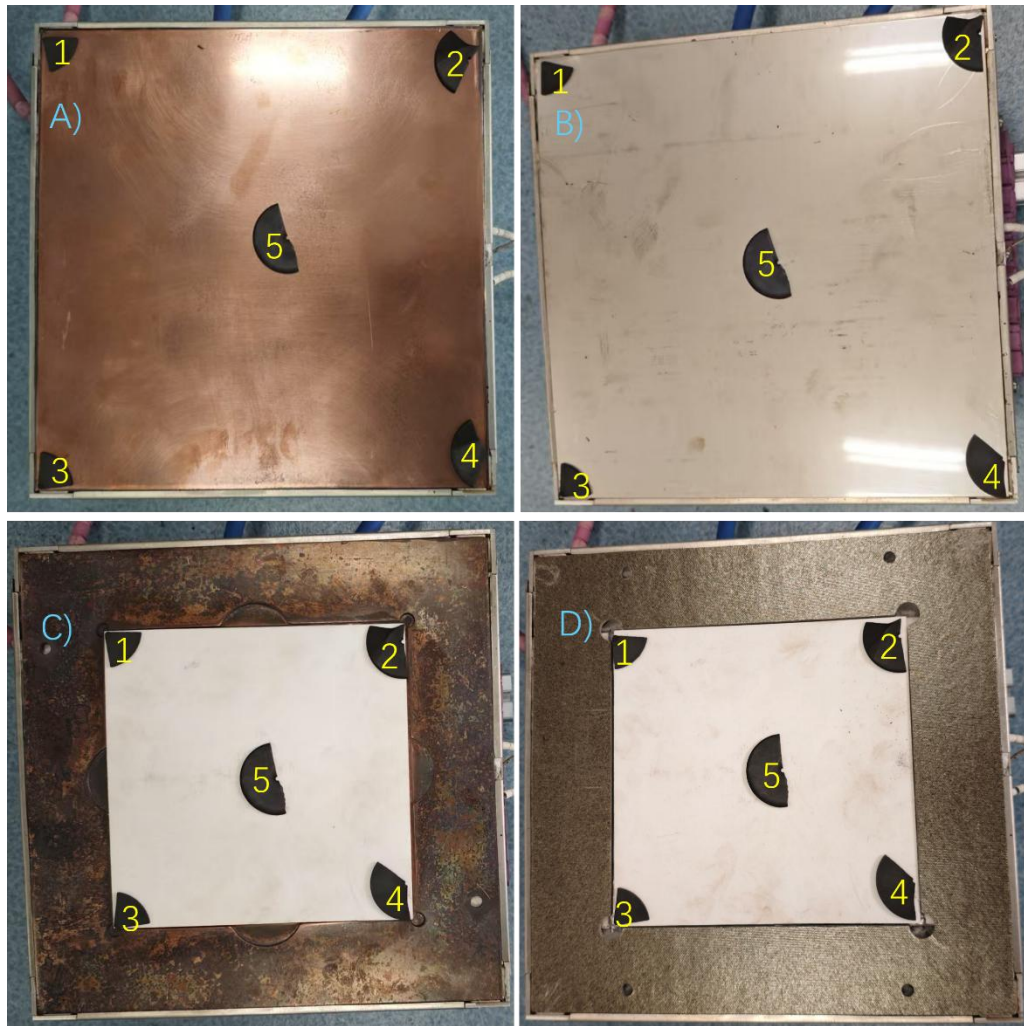


Figure 51: The experiment set of four materials for the comparison experiments: A) The big copper plate set; B) The big stainless steel plate set; C) The ceramic plate with manufactured copper; D) The ceramic plate with Mika cover

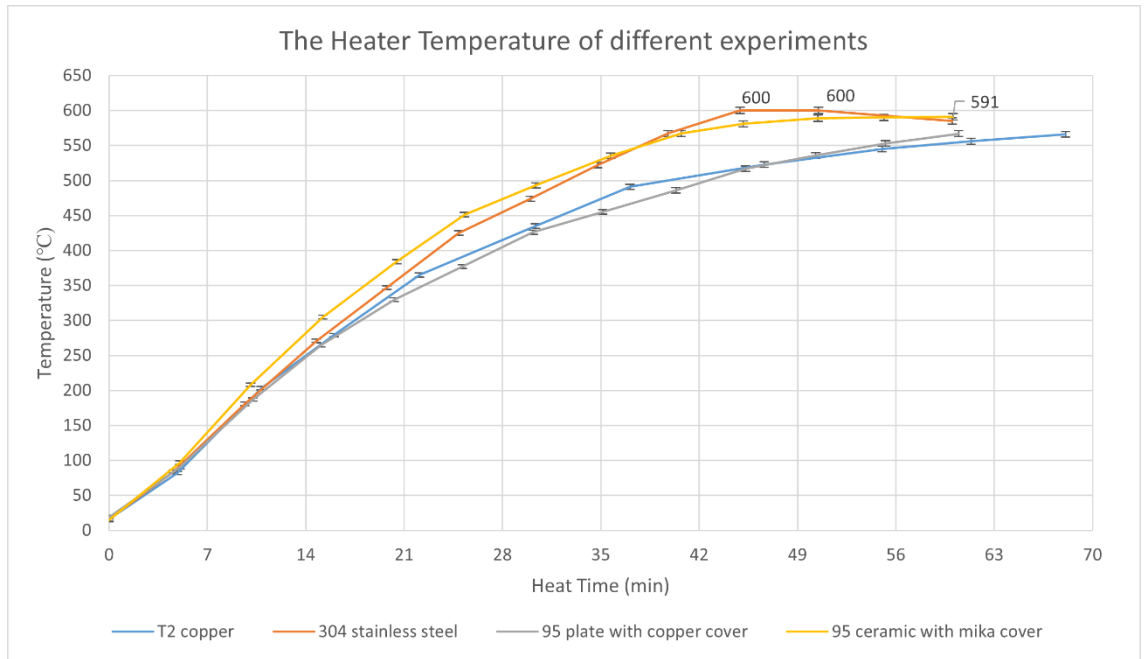


Figure 52: The heater temperature of different material experiments

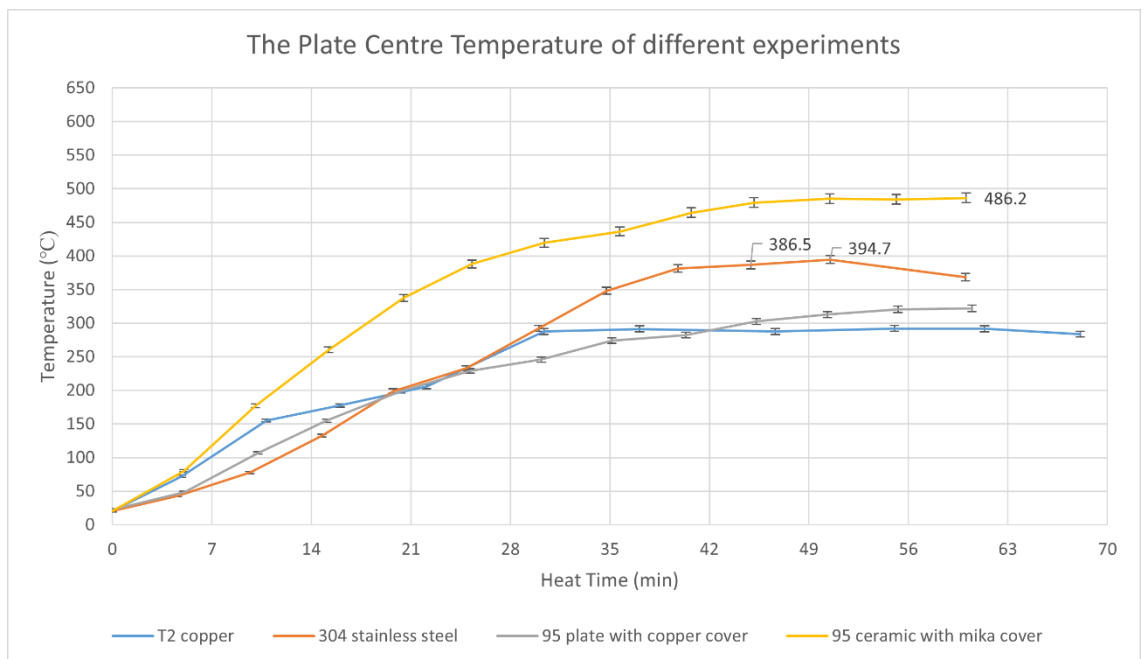


Figure 53: The plate centre temperature of different material experiments.

Figure 52 shows the heater’s temperature trending similarly and the heat speed before 250°C. The heater’s temperature of the ceramic-Mika group increased faster than other materials before 500°C. But all groups have quite

the same final heater's temperature at the end. Nevertheless, the Plate centre temperature has quite different performances. The ceramic-Mika group had the highest heat speed and final temperature among the other three groups. T2 copper had the same heat speed before 100°C and spent the least time reaching the maximum temperature, but its maximum temperature was the lowest. 304 stainless steel has the second highest final temperature, but still has a 100°C difference lower than the ceramic-Mika group. It might be the limit of the temperature set, but the maximum heater temperature cannot reach over 650°C shown in Figure 54. Thus, the maximum plate centre temperature of the stainless steel plate cannot reach 500°C even when setting a higher PID temperature or maximum power.

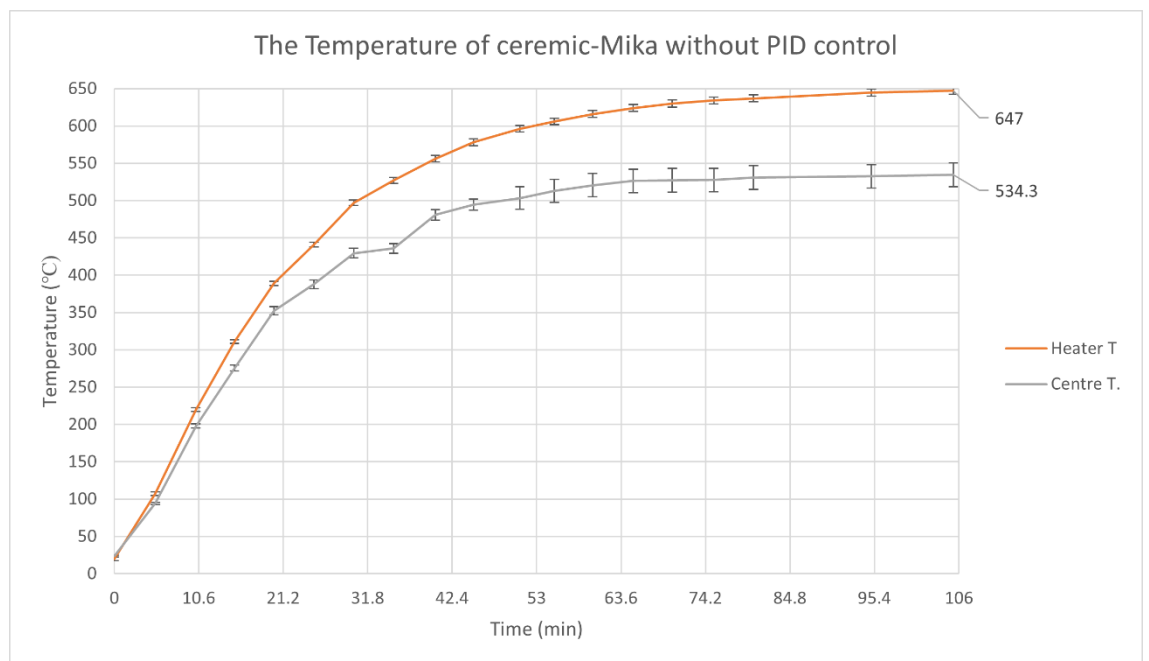


Figure 54: The temperature graph of the Ceramic-Mika plate without PID control

This graph shows the highest heater temperature, 647°C, and plate centre temperature, 534.3°C, for the ceramic-Mika experiment. This proves that the ceramic-Mika reaches the requirement in the Methodology Chapter. However, it cannot reach the 550°C, the expected temperature that is beneficial to future droplet remelting study and product printing study, which means there are still

drawbacks to the recently built system. A more advanced substrate system is required for future developments since the MDE technique will focus on the 304 stainless steel printing in further study.

### 4.1.3. Conclusion of the substrate system

In conclusion, the substrate system has been manufactured and meets most requirements in section 3.1.2. Table 11 shows the status of the achievement and details how the requirement has been reached.

Table 11: The table of the status and the details about the achieved requirement

No.	Status	Results
1	Complete	After cooling down, the substrate plate can be easily removed and changed by hand.
2	Reach but not perfect	A PID box controls the heater's temperature and can make the temperature stable.
3	Reach but not perfect	The repeatable maximum substrate plate temperature reached 534.3°C, which does not fit the 550°C expected temperature. The test results will be shown in the results section.
4	Complete	The whole system is 32.5cm in length, 32.5cm in width, and 7.2cm in height, and it can be fully used within the platform's limits.
5	Complete	The cooler part connects to the platform by four screws, and the heating part assembles with the cooler part by four screws.
6	Complete	The system is 6.7 Kg, including the cooling part, 1.35 kg and the heating part, 5.35 kg.
7	Reach but not perfect	The used plate size is 20 cm*20 cm, which is smaller than the platform's moving limit. However, the plate can't catch all the droplets at the platform's limit.
8	Complete	A cooler part is assembled in the system to protect the heat of the screws coming from the heater.

## 4.2. Distance Experiment

All following experiments (distance, temperature and roughness) will have the same droplet temperature, which is 800°C. And the same parameter of the

droplet control program on the LabVIEW (Appendix 3), which controls the droplet production:

Delay between up and down: 1000

Forward distance: 7

Backward distance: 1

Forward pause: 1500

Backward pause: 60

Pause for direction change: 100

Delay between each movement: 2000000

Considering the K parameters in the calculation and prediction section from section 3.3 and the design of the whole prototype, the height experiment was set at a distance between the nozzle and the substrate plate surface at 20mm, 45mm, 70mm, 95mm and 120mm. The number of all droplets and the splashed droplets has been recorded to figure out the suitable distance that should be used for the following two experiments. The results of the experiment are presented in Figure 55 below.

In this distance experiment, the substrate is at room temperature. The surface roughness of the copper, stainless steel and ceramic is  $2.069\mu\text{m}$ ,  $1.489\mu\text{m}$  and  $1.293\mu\text{m}$ .

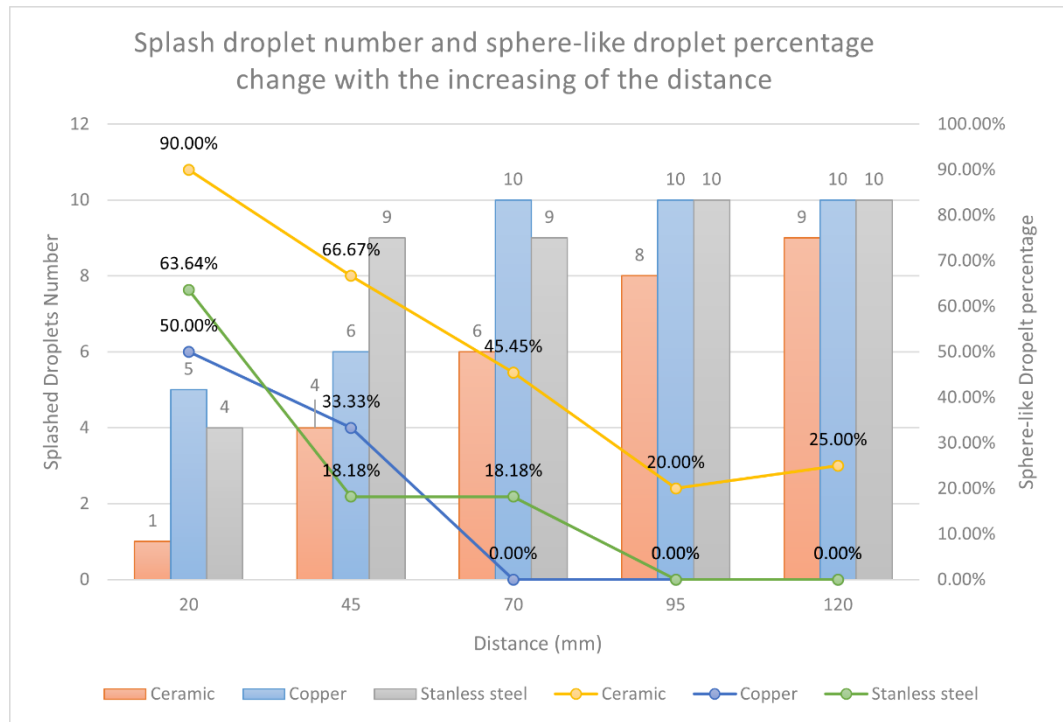


Figure 55: Splash droplet number and sphere-like droplet percentage change with the increase in the distance

The graph shows an increase in the splashed droplets number of the droplets and a decrease in the sphere-like percentage of the droplets, impacting with the rising of the distance increases. The sphere-like droplet was calculated:

$$Sphere \% = \frac{Total\ droplets - Splash\ droplets}{Total\ droplets} \quad \text{Equation 12}$$

The graph follows the prediction of the K parameter in section 3.3 that with the increase in the distance, the K value will also increase, which results in a decreasing percentage of sphere-like droplets. But differently, the ceramic plates will still have over 20% sphere-like droplets when the distance is 95mm and 120mm, where the K value was indeed larger than 57.7 based on the distance prediction in section 3.3. And in this situation, all the droplets should be splashed based on Mundo et al. [94]. This might be caused by the oxidation of the aluminium and the solidification of the droplet over a long distance,

which has been mentioned by Yang et al. [103].

However, the copper and stainless steel plates' droplet impact at this distance of this range is totally splashed. The droplets on the copper plate totally splash at 70mm, which has the worst performance. Besides, almost half of the droplets splashed on the copper plate and the stainless steel plate at the start distance of 20mm since the K value is 45.5, close to 57.7 [94].

These two plates will absorb the magnetic field from the coil of the induction heater and cause a sudden reduction of the heat on the graphite, which will influence the production of the droplet. Meanwhile, several rebounds of the droplets can be observed at 70mm, 95mm, and 120mm, causing a variable total number of droplets on the ceramic plate. This might also be caused by the oxide layer of the aluminium, which has been mentioned by Yang et al. [103]. Meanwhile, Aziz and Chandra [100] assumed that the temperature of the spreading droplet is equal to the initial temperature. Still, the thermal conduct resistance between the aluminium 6061 and the ceramic plate is bigger than the aluminium between copper and stainless steel, which caused the droplet to be more in the liquid phase [100]. Aziz and Chandra [100] mentioned that the conduct resistance has a negligible impact on droplet impact dynamics in their velocity change experiments. However, the material conduct resistance may be necessary in the droplet-impacting process.

Based on the observation in the distance experiment, the following temperature and roughness experiments have been adjusted to set the distance at 45mm to avoid the material effect on the coil and have better performance to produce sphere-like droplets to measure the contact angle. Before this experiment, the distance was considered to be set at 5mm, which was used for printing the simple product.

### 4.3. Temperature Experiment

Based on the temperature test in the methodology section, the copper and the stainless steel plates are oxidised at a temperature of 200 degrees. Thus, to avoid the effect of the oxygen layers, the highest temperature of these two plates has been set at around 150 degrees. The height–distance between the nozzle and the substrate was set at 45mm so that the loss of magnetic field doesn't affect the temperature of the print head. However, as for the ceramic plate, a higher temperature has been set to see the behaviour of the droplet's impact on a high-temperature substrate plate.

The plates will have quite close surface roughness – 1.8747 $\mu\text{m}$  for the copper plate, 1.55659 $\mu\text{m}$  for the stainless steel and 1.241 $\mu\text{m}$  for the ceramic plate. The following Figure 56 and Figure 57 display the two distinct graphs.

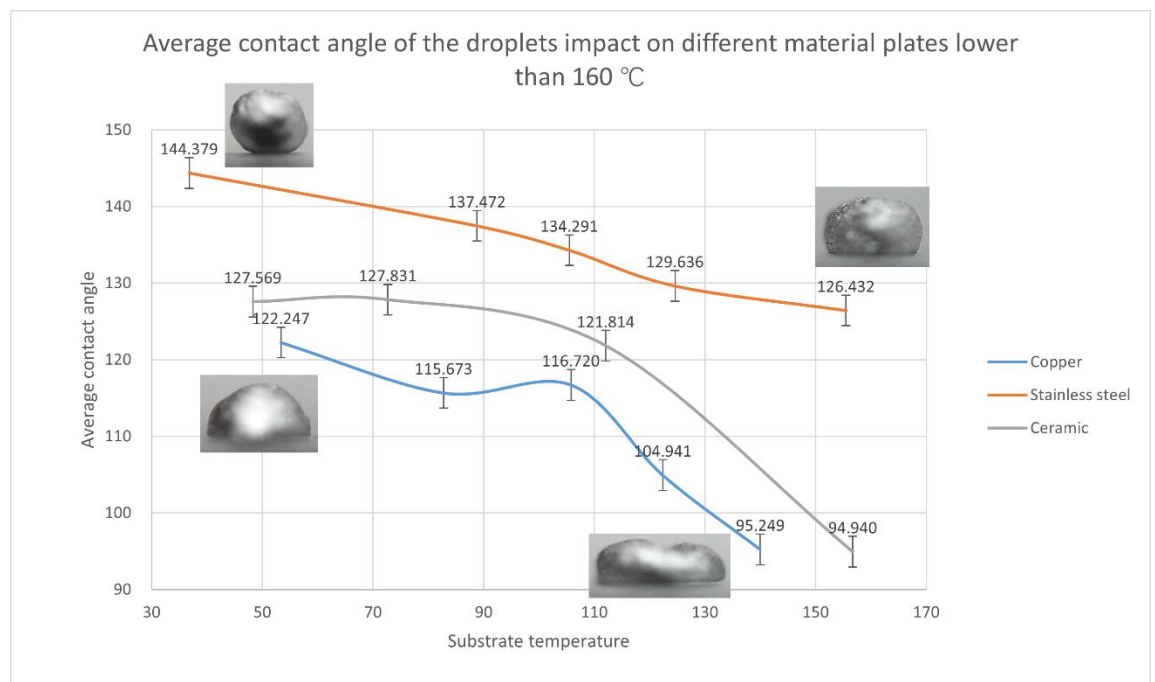


Figure 56: Average contact angles of the droplets on all three materials change with increasing substrate plate temperature lower than 160 degrees with photos of droplets

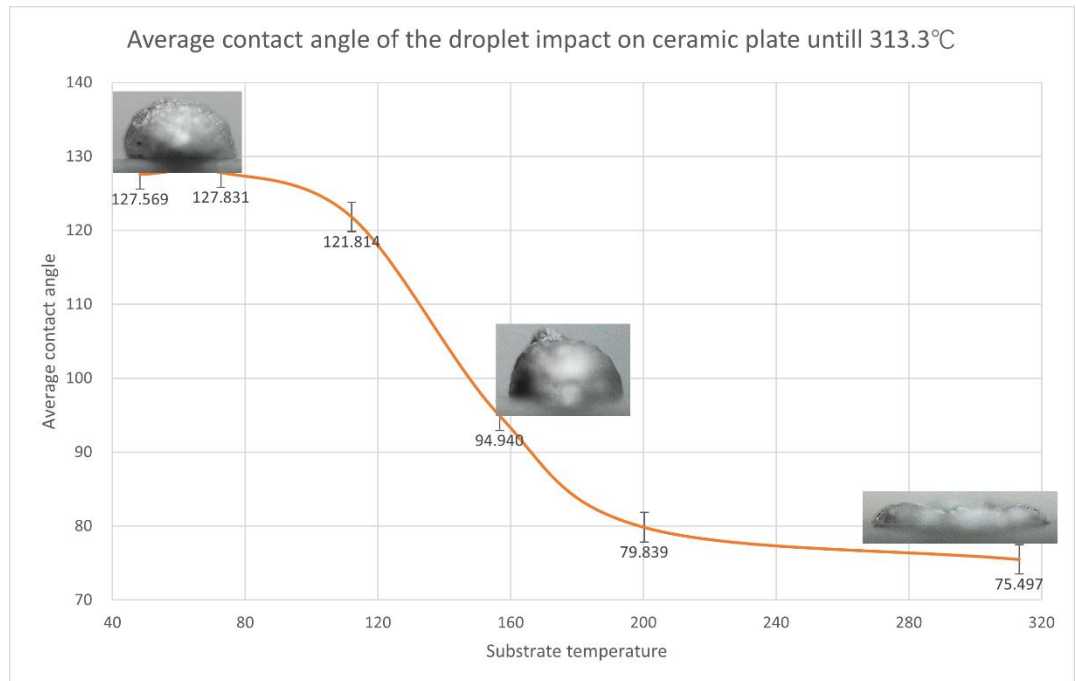


Figure 57: Average contact angle of droplets on ceramic changes by the increasing substrate surface temperature until 313.3 degrees with the photos of the droplets.

Graph a) shows the average contact angle changed by the increasing substrate surface temperature under 160 degrees. All three materials show that the contact angle has the opposite trend of the increase of the substrate temperature. The contact angle of the droplet impact on the stainless steel plate is the biggest of the three materials, and the change in it was also smaller than the other two materials, which is 18°. Also, aluminium 6061 cannot wet the stainless steel plate since all the contact angles are over 90° with the temperature under 160 degrees.

The droplet cross-section shape changes from a circle to a half-circle. As for the copper plate, the value of its contact angle is the smallest of all three materials at the same temperature. The graph also demonstrates that the wettability of the aluminium 6061 droplet increases with the rise in temperature, as stated by Lin et al. [147], [148] in the literature review section.

However, the temperature of 140 degrees cannot allow the aluminium 6061 to totally wet the T2 copper since the contact angle of that was  $95.249^\circ$ , which is still larger than the transfer contact angle of  $90^\circ$ . The shape of the droplet changed from a half-sphere to a doughnut-like shape, with a hole at the centre of the droplet, like the receding breakup in Table 4. It means the droplet is non-wet or partially wet with the substrate [112]. The biggest contact angle happens at the lowest temperature at the bottom corner of the droplet. The sudden increase in the contact angle at  $105.8^\circ\text{C}$  may be caused by the instability of the droplet production from the printhead and the selection of the droplets, since the more spherical droplets are more likely to be selected. However, it follows Venkatesan et al. [136] that the contact angle will be more affected by the temperature in high-temperature regions. In Figure 57, the contact angle on the ceramic plate partly follows the theory from  $120^\circ\text{C}$  to  $200^\circ\text{C}$ .

According to Graph b), the droplets that impact the ceramic plate have the exact shape change but appear at a more extensive temperature range. The contact angle change is around  $52^\circ$ , less than half of the angle difference in Zhang et al. [138] ( $147^\circ$ ). At a temperature over 200 degrees, the change in the contact angle becomes minor, only  $4.342^\circ$ . Meanwhile, the thickness of the droplet decreases with the increase in the bottom length of the droplet. The higher temperature has not been tested since the droplet's shape at  $313.3$  degrees is not suitable for forming the production. The hole at the centre of the droplet will cause a hollow sensation when the upper droplet solidifies over the bottom droplet.

According to both graphs, the trend of the contact angle follows the Li et al. [135] and Bao et al. [129] that an increasing substrate temperature causes a decrease in droplet contact angles. However, the temperature of the impacting process in this experiment was much lower than the temperature in

the article [129] since the start temperature was 700°C and the material was static. At a distance of 45mm, around 165 degrees of the ceramic plate temperature and around 150 degrees of copper plate temperature will be the fit temperature for droplet production because the contact angle will be almost 90° based on Graphs a) and b). However, it is hard for droplets to remelt and combine at this temperature, which means the final product's strength will weaken after printing. Thus, post-processing is required to remelt and combine the droplets to strengthen the whole structure of the product.

Nevertheless, the words 'UNNC' and square have been printed in the methodology section, and all droplets are combined well. This is because the distance was 5mm, and the temperature of the substrate was higher than 500 degrees. Hence, further study about low distance and higher ceramic plate temperature is required, which can help improve the quality of the printed part of the product.

#### **4.4. Roughness Experiment**

The methodology section demonstrates the detailed value of the surface roughness of sample plates. The two graphs in Figure 58 and Figure 59 show that the average contact angle changed with the surface roughness. The ceramic plates have an independent graph because the range of the change in surface roughness is too small.

The height was 45mm, and the substrate was at room temperature.

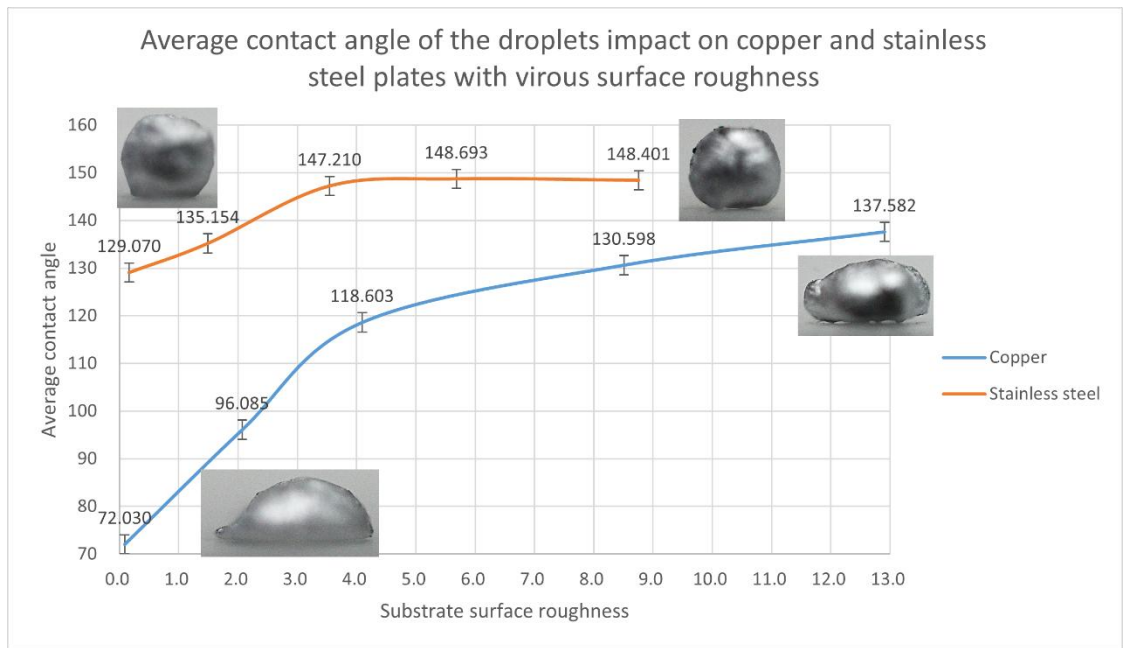


Figure 58: Average contact angles of the droplets on stainless steel and copper plates change by different surface roughness

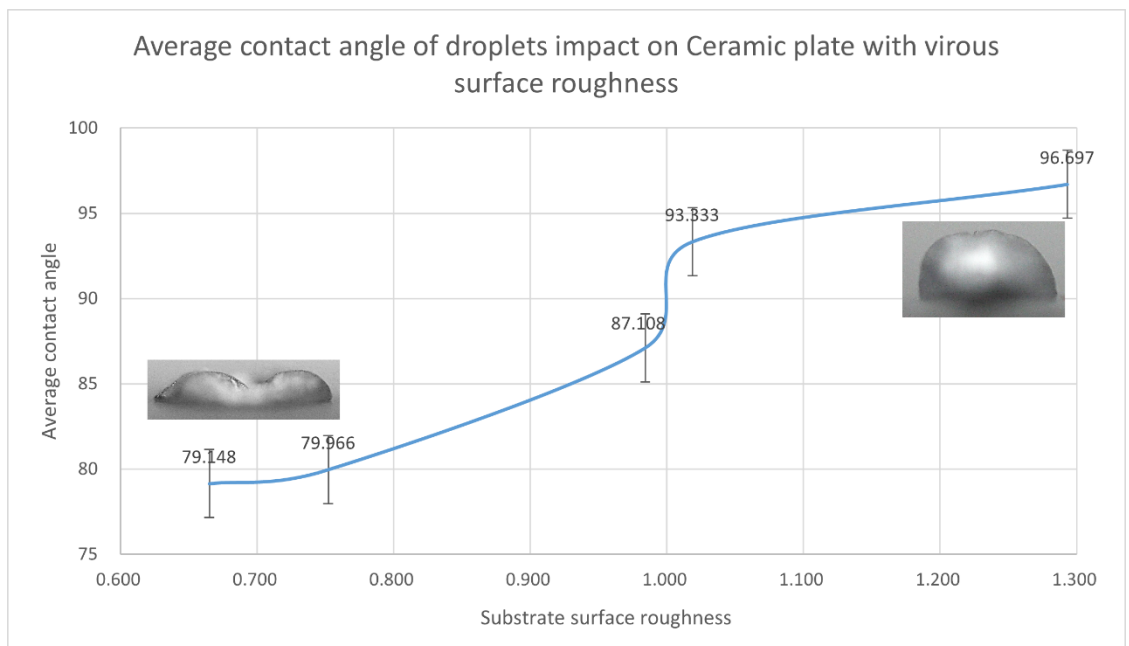


Figure 59: Average contact angles of droplets on a ceramic plate change by different surface roughness.

As seen in the graphs, the contact angle of the droplets increases with the

rise of the surface roughness, which follows QI et al. [144]. The stainless steel plate has a contact angle of over  $120^\circ$  even though it is on the smoothest surface, whose surface roughness is 0.164. Also, the rebound of some droplets was observed at this roughness. However, with the increase of the surface roughness, the rebound disappears, and the droplets will grasp the plate harder, which can be felt during the picking up of the droplets. Also, the bottom surface of the droplets becomes rougher at bigger surface roughness, which can be seen in the graphs of both copper and stainless steel. It seems proven the impact of the droplet was more in the Wenzel model [139] that the droplet will fill the space on the surface caused by roughness, especially in high roughness. But, this does not fit the findings of Xiong and Cheng [142], that higher surface roughness will decrease the bubbles on the substrate face of the droplet.

The copper plate has the same appearance, and the swell is more evident in the picture of the high-roughness copper plate. This means the higher roughness of the plates may not help improve the product's surface quality because the liquid metal will fill the plate's hole and create a tuber, especially with a sandblasted surface. However, there are small holes at the bottom of the droplet from the smooth surface, which confirms the theory of Xiong and Cheng [142].

Thus, the surface roughness of the plate should be carefully considered when using sandblasting to change it. There might be a range of surface roughness that can have a flat bottom surface of the droplets.

Meanwhile, the stainless steel plate is consistent with the Wenzel equation [139] when the contact angle is bigger than  $90^\circ$ , the contact angle increases as the surface roughness increases. But, as for the copper and ceramic plate, the range under  $90^\circ$  is opposite to the Wenzel equation [139]. This is because the impact droplet has extra energy from gravity and the initial

velocity, which helps break the droplet's surface tension and adhesion. However, the sessile bubble is more commonly used to measure the static contact angle, at which the droplet will have no initial velocity. The roughness factor  $r$  has been calculated using the contact angle of droplets on the smooth plate as the equilibrium contact angle assumed by Vaikuntanathan and Sivakumar [128], which is demonstrated in Table 12 and can be used as a present for further study.

Table 12: Surface roughness, the measured contact angle and the roughness factor  $r$

Material	Post-process	Roughness	Measured contact angle	Cos value	$r$
Copper	12	12.909	137.582	-0.738	-2.393
	20	8.511	130.598	-0.651	-2.109
	60	4.096	118.603	-0.479	-1.552
	100	2.069	96.085	-0.106	-0.344
	Polish	0.085	72.030	0.309	1.000
Stainless steel	12	8.759	148.401	-0.852	1.351
	20	5.686	148.693	-0.854	1.356
	60	3.546	147.210	-0.841	1.334
	100	1.489	135.154	-0.709	1.125
	Polish	0.164	129.070	-0.630	1.000
Ceramic	Normal	1.293	96.697	-0.117	-0.619
	60	1.019	93.333	-0.058	-0.309
	180	0.984	87.108	0.050	0.268
	600	0.752	79.966	0.174	0.925
	3000	0.665	79.148	0.188	1.000

The  $90^\circ$  contact angle will appear at the surface roughness around  $1.8\mu\text{m}$  for the copper plate and  $1\mu\text{m}$  for the ceramic plate. However, more experiment is required to find a suitable group of parameters since these results are under the open air, 45mm distance,  $800^\circ\text{C}$  initial droplet temperature and room temperature of the surface temperature.

## 4.5. Conclusion

Among all three experiments and the temperature test, 304 stainless steel is the worst choice of substrate material for metal droplet extrusion because the contact angle of droplets on stainless steel is always larger than  $120^\circ$  based on the experimental situation. Meanwhile, increasing temperature could help reduce the contact angle value, but it will also cause oxidation on the surface, limiting the temperature range.

T2 copper performs better than stainless steel; 150 degrees of plate temperature and  $1.8\mu\text{m}$  surface roughness will bring  $90^\circ$  of the droplet's contact angle. However, low plate temperature is still a restriction of the material since droplets cannot remelt and combine with each other well at this temperature.

Compared to these two materials, 95 aluminium oxide ceramic is the best choice for now because it can reach the highest temperature at  $534.3^\circ\text{C}$  without oxidation. Besides, the  $90^\circ$  contact angle can be achieved when the temperature is 165 degrees with a roughness of  $1.241\mu\text{m}$  and  $1\mu\text{m}$  of the roughness when the temperature is room temperature.

Although the maximum temperature of this substrate is  $534.3^\circ\text{C}$ , not the expected  $550^\circ\text{C}$ . The substrate system can be regarded as successful. Because the  $550^\circ\text{C}$  is designed for testing product printing and future droplet remelting experiments. The experiments in this thesis do not have the substrate to be this hot since the droplets have been mostly splashed at a temperature of  $320^\circ\text{C}$  and a distance of 45mm, which are not the conditions needed for this thesis.

# Chapter 5 Conclusion

## 5.1. Conclusion

In conclusion, the three objectives illustrated in the introduction section have been completed. The literature on additive manufacturing, metal 3D printing and the morphology of the impacting droplets has been reviewed and concluded to guide the design of the substrate and the arrangement of the experiments.

The development of the substrate design has been shown. The substrate system was developed by conducting the temperature test. Finally, the mica cover with different insert plates was selected since this group can purchase higher surface temperatures. The printer prototype has been tested by printing simple, flat products. The quality of the products is not perfect, but the droplets combine well, and the strength of the structure is good. This represents a significant improvement as the prototype of a metal droplet extrusion printer capable of printing products has been built.

Three experiments have been carried out, and the results have been used to analyse the relationship between contact angle and the different parameters – distance, surface temperature, surface roughness and the plate material. 95 aluminium oxide ceramic has been chosen as the best plate material for the prototype because the contact angle of the droplet can reach  $90^\circ$  with specific temperature, surface roughness, and distance values. Also, the upper-temperature limit and non-oxidation surface at high temperatures are essential in the decision. Although the surface roughness change is hard and small for ceramic, it is enough for printing a simple, flat product.

## 5.2. Future Expectations

Although the prototype is a good achievement, there are some drawbacks, and the field needs further research and development.

As for the hardware, the printhead needs to be improved to avoid the influence of the coil's magnetic field on the droplet. A glove box is required to provide a stable environment and eliminate the effect of oxidation. A better temperature feedback control loop is needed to increase the accuracy of the surface temperature. Induction heating can be considered and may also help improve the droplet quality. Higher maximum temperatures should be achieved for studying the droplet remelting and the product printing.

As for further study, the smaller distance and higher temperature should be considered when researching the remelt behaviour of two droplets. More kinds of droplet materials, as well as substrate material, should also be studied since there are many types of ceramic, and the change of the prototype causes differences in the morphology of the droplets. Multiple types of droplets can also be studied in this prototype because this prototype can print simple objects.

After all, the MDE technique still has many fields and problems to be researched and solved. But its future looks promising, and this approach's goal could be achieved.

## Chapter 6 References

[1] C. Weller, R. Kleer, and F. T. Piller, “Economic implications of 3D printing: Market structure models in light of additive manufacturing revisited,” *Int J Prod Econ*, vol. 164, pp. 43–56, Jun. 2015, doi: 10.1016/J.IJPE.2015.02.020.

[2] M. D. Monzón, Z. Ortega, A. Martínez, and F. Ortega, “Standardization in additive manufacturing: activities carried out by international organizations and projects,” *International Journal of Advanced Manufacturing Technology*, vol. 76, no. 5–8, pp. 1111–1121, Feb. 2015, doi: 10.1007/S00170-014-6334-1/METRICS.

[3] S. A. M. Tofail, E. P. Koumoulos, A. Bandyopadhyay, S. Bose, L. O’Donoghue, and C. Charitidis, “Additive manufacturing: scientific and technological challenges, market uptake and opportunities,” Jan. 01, 2018, *Elsevier B.V.* doi: 10.1016/j.mattod.2017.07.001.

[4] C. Bai, P. Dallasega, G. Orzes, and J. Sarkis, “Industry 4.0 technologies assessment: A sustainability perspective,” *Int J Prod Econ*, vol. 229, p. 107776, Nov. 2020, doi: 10.1016/J.IJPE.2020.107776.

[5] J. C. Vasco, “Additive manufacturing for the automotive industry,” *Addit Manuf*, pp. 505–530, Jan. 2021, doi: 10.1016/B978-0-12-818411-0.00010-0.

[6] B. Blakey-Milner *et al.*, “Metal additive manufacturing in aerospace: A review,” *Mater Des*, vol. 209, p. 110008, Nov. 2021, doi: 10.1016/J.MATDES.2021.110008.

[7] A. Leticia Braz and I. Ahmed, “Manufacturing processes for polymeric micro and nanoparticles and their biomedical applications,” *AIMS Bioeng*, vol. 4, no. 1, pp. 46–72, 2017, doi:

10.3934/bioeng.2017.1.46.

[8] A. Goyanes, F. Fina, A. Martorana, D. Sedough, S. Gaisford, and A. W. Basit, “Development of modified release 3D printed tablets (printlets) with pharmaceutical excipients using additive manufacturing,” *Int J Pharm*, vol. 527, no. 1–2, pp. 21–30, Jul. 2017, doi: 10.1016/J.IJPHARM.2017.05.021.

[9] D. Beiderbeck, H. Krüger, and T. Minshall, “The Future of Additive Manufacturing in Sports,” pp. 111–132, 2020, doi: 10.1007/978-3-030-50801-2\_7.

[10] A. Paolini, S. Kollmannsberger, and E. Rank, “Additive manufacturing in construction: A review on processes, applications, and digital planning methods,” *Addit Manuf*, vol. 30, p. 100894, Dec. 2019, doi: 10.1016/J.ADDMA.2019.100894.

[11] H. A. Colorado, E. I. Gutierrez-Velasquez, L. D. Gil, and I. L. de Camargo, “Exploring the advantages and applications of nanocomposites produced via vat photopolymerization in additive manufacturing: A review,” *Advanced Composites and Hybrid Materials 2023 7:1*, vol. 7, no. 1, pp. 1–19, Dec. 2023, doi: 10.1007/S42114-023-00808-Z.

[12] M. H. Mobarak *et al.*, “Recent advances of additive manufacturing in implant fabrication – A review,” *Applied Surface Science Advances*, vol. 18, p. 100462, Dec. 2023, doi: 10.1016/J.APSADV.2023.100462.

[13] M. A. Islam *et al.*, “Additive manufacturing in polymer research: Advances, synthesis, and applications,” *Polym Test*, vol. 132, p. 108364, Mar. 2024, doi: 10.1016/J.POLYMERTESTING.2024.108364.

[14] S. Bhasin, R. M. Singari, P. K. Arora, and H. Kumar, “Implications of Additive Manufacturing on Supply Chain Management,” *Journal of Industrial Integration and Management*, vol. 9, no. 1, pp. 117–131, Mar. 2024, doi: 10.1142/S2424862221500299/ASSET/IMAGES/LARGE/S2424862221500299FIGF12.JPEG.

[15] S. Ford and M. Despeisse, “Additive manufacturing and sustainability: an exploratory study of the advantages and challenges,” *J Clean Prod*, vol. 137, pp. 1573–1587, Nov. 2016, doi: 10.1016/J.JCLEPRO.2016.04.150.

[16] M. Attaran, “The rise of 3-D printing: The advantages of additive manufacturing over traditional manufacturing,” *Bus Horiz*, vol. 60, no. 5, pp. 677–688, Sep. 2017, doi: 10.1016/J.BUSHOR.2017.05.011.

[17] O. Abdulhameed, A. Al-Ahmari, W. Ameen, and S. H. Mian, “Additive manufacturing: Challenges, trends, and applications,” *Advances in Mechanical Engineering*, vol. 11, no. 2, Feb. 2019, doi: 10.1177/1687814018822880.

[18] M. Nazmul and H. Dipu, “An Overview on Additive Manufacturing Technology: Last Decade’s Literature, Components, Generic Process, Printing Categories, Associated Materials, Advantages, Disadvantages, and Research Gaps.”

[19] A. Bhatia and A. K. Sehgal, “Additive manufacturing materials, methods and applications: A review,” *Mater Today Proc*, vol. 81, no. 2, pp. 1060–1067, Jan. 2023, doi: 10.1016/J.MATPR.2021.04.379.

[20] G. Prashar, H. Vasudev, and D. Bhuddhi, “Additive

manufacturing: expanding 3D printing horizon in industry 4.0,” *International Journal on Interactive Design and Manufacturing*, vol. 17, no. 5, pp. 2221–2235, Oct. 2023, doi: 10.1007/s12008-022-00956-4.

[21] Formlabs, “How to Compare SLS 3D Printer Prices.” Accessed: Dec. 28, 2023. [Online]. Available: <https://formlabs.com/blog/selective-laser-sintering-sls-3d-printer-price/>

[22] R. Sreenivasan and D. L. Bourell, “Sustainability Study in Selective Laser Sintering-An Energy Perspective,” 2009.

[23] V. Gupta, P. Nesterenko, and B. Paull, “An Introduction to 3D Printing 1.1,” in *3D Printing in Chemical Sciences: Applications Across Chemistry*, 1st ed., London: Royal Society of Chemistry, 2019, ch. 1, pp. 1–21. doi: <https://doi.org/10.1007/s10337-019-03788-9>.

[24] T. Campbell, C. Williams, O. Ivanova, and B. Garrett, “Could 3D Printing Change the World?: Technologies, Potential, and Implications of Additive Manufacturing,” 2011. [Online]. Available: <http://www.jstor.com/stable/resrep03564>

[25] J. G. Zhou, D. Herscovici, and C. C. Chen, “Parametric process optimization to improve the accuracy of rapid prototyped stereolithography parts,” *Int J Mach Tools Manuf*, vol. 40, no. 3, pp. 363–379, Feb. 2000, doi: 10.1016/S0890-6955(99)00068-1.

[26] I. Gibson and D. Shi, “Material properties and fabrication parameters in selective laser sintering process,” *Rapid Prototyp J*, vol. 3, no. 4, pp. 129–136, 1997, doi: 10.1108/13552549710191836.

[27] N. Shahrubudin, T. C. Lee, and R. Ramlan, “An Overview on 3D Printing Technology: Technological, Materials, and

Applications,” *Procedia Manuf*, vol. 35, pp. 1286–1296, Jan. 2019, doi: 10.1016/J.PROMFG.2019.06.089.

[28] N. Kumar Naulakha, “Guidelines for increasing application of 3D Metal Printing-a case study at Equinor ASA,” 2021. Accessed: Aug. 14, 2024. [Online]. Available: <https://munin.uit.no/handle/10037/23365>

[29] N. Shahrubudin, T. C. Lee, and R. Ramlan, “An Overview on 3D Printing Technology: Technological, Materials, and Applications,” *Procedia Manuf*, vol. 35, pp. 1286–1296, Jan. 2019, doi: 10.1016/J.PROMFG.2019.06.089.

[30] M. R. Silva, A. M. Pereira, Á. M. Sampaio, and A. J. Pontes, “Assessment of the Dimensional and Geometric Precision of Micro-Details Produced by Material Jetting,” *Materials 2021, Vol. 14, Page 1989*, vol. 14, no. 8, p. 1989, Apr. 2021, doi: 10.3390/MA14081989.

[31] 3DEXPERIENCE MAKE, “Material jetting - MJ, NPJ, DOD | Make.” Accessed: Apr. 14, 2022. [Online]. Available: <https://make.3dexperience.3ds.com/processes/material-jetting>

[32] V. Korkut and H. Yavuz, “Comparison and Evaluation of Various Material Jetting Technologies in Terms of Additive Manufacturing,” *JOURNAL OF MATERIALS AND ELECTRONIC DEVICES*, vol. 1, no. 1, pp. 20–24, Nov. 2019.

[33] S. Tyagi, A. Yadav, and S. Deshmukh, “Review on mechanical characterization of 3D printed parts created using material jetting process,” in *Materials Today: Proceedings*, Elsevier Ltd, 2021, pp. 1012–1016. doi: 10.1016/j.matpr.2021.07.073.

[34] 3DEXPERIENCE MAKE, “Make : 3D printing CNC

Machine Injection Molding - Dassault Systèmes®.” Accessed: Aug. 14, 2024. [Online]. Available: <https://make.3dexperience.3ds.com/processes/material-jetting>

[35] Mikahila L, “Material Jetting vs. Binder Jetting: Which Jetting Process Should You Choose? - 3Dnatives.” Accessed: Aug. 14, 2024. [Online]. Available: <https://www.3dnatives.com/en/material-jetting-vs-binder-jetting-300920216/>

[36] “Bambu Lab A1 mini 3D Printer A1 mini Combo / In stock | Bambu Lab US.” Accessed: Jul. 26, 2024. [Online]. Available: <https://us.store.bambulab.com/products/a1-mini?variant=41416712716424>

[37] T. Y. Ansell, H. Wang, and J. Fuh, “Current Status of Liquid Metal Printing,” *Journal of Manufacturing and Materials Processing 2021, Vol. 5, Page 31*, vol. 5, no. 2, p. 31, Apr. 2021, doi: 10.3390/JMMP5020031.

[38] Alfred I. Tsung Pan, Mountain View, and Calif., “Monolithic thermal ink jet printhead with integral nozzle and ink feed,” US4894664A, Jan. 16, 1990 Accessed: Aug. 15, 2024. [Online]. Available: <https://patents.google.com/patent/US4894664A/en>

[39] R. Ghafouri-Azar, S. Shakeri, S. Chandra, and J. Mostaghimi, “Interactions between molten metal droplets impinging on a solid surface,” *Int J Heat Mass Transf*, vol. 46, no. 8, pp. 1395–1407, Apr. 2003, doi: 10.1016/S0017-9310(02)00403-9.

[40] Johannes F Gottwald, “Liquid metal recorder,” US3596285A, Jul. 11, 1969 Accessed: Aug. 14, 2024. [Online]. Available: <https://patents.google.com/patent/US3596285A/en>

[41] H. Hieber, “Method of applying small drop-shaped

quantities of melted solder from a nozzle to surfaces to be wetted and device for carrying out the method,” US4828886A, 1986 Accessed: Apr. 13, 2022. [Online]. Available: <https://patents.google.com/patent/US4828886A/en>

[42] M. Orme and R. F. Smith, “Enhanced Aluminum Properties by Means of Precise Droplet Deposition,” *J Manuf Sci Eng*, vol. 122, no. 3, pp. 484–493, Aug. 2000, doi: 10.1115/1.1285914.

[43] H.-Y. Kim, J.-P. Cherng, and J.-H. Chun, “Recent Progress in Droplet-Based Manufacturing Research,” 2002.

[44] X. S. Jiang, L. H. Qi, J. Luo, H. Huang, and J. M. Zhou, “Research on accurate droplet generation for micro-droplet deposition manufacture,” *International Journal of Advanced Manufacturing Technology*, vol. 49, no. 5–8, pp. 535–541, Jul. 2010, doi: 10.1007/s00170-009-2403-2.

[45] R. E. Marusak, *Picoliter Solder Droplet Dispensing*, First. Austin: The University of Texas at Austin, 1993. doi: 10.15781/T2H98ZX0J.

[46] M. V. Rasar. B. P. J. C. C. M. V. G. V. Kuznetsov, “Device for ejecting droplets of a fluid having a high temperature,” US8444028B2, 2008 Accessed: Apr. 14, 2022. [Online]. Available: <https://patents.google.com/patent/US8444028B2/en>

[47] V. Sukhotskiy, P. Vishnoi, I. H. Karamelas, S. Vader, Z. Vader, and E. P. Furlani, “Magnetohydrodynamic Drop-on-Demand Liquid Metal Additive Manufacturing: System Overview and Modelling,” Jun. 2018. doi: 10.11159/ffhmt18.155.

[48] Z. Luo, X. Wang, L. Wang, D. Sun, and Z. Li, “Drop-on-demand electromagnetic printing of metallic droplets,” *Mater Lett*, vol.

188, pp. 184–187, Feb. 2017, doi: 10.1016/J.MATLET.2016.11.021.

[49] C. Ladd, J. H. So, J. Muth, and M. D. Dickey, “3D Printing of Free Standing Liquid Metal Microstructures,” *Advanced Materials*, vol. 25, no. 36, pp. 5081–5085, Sep. 2013, doi: 10.1002/ADMA.201301400.

[50] L. Wang and J. Liu, “Liquid phase 3D printing for quickly manufacturing conductive metal objects with low melting point alloy ink,” *Science China Technological Sciences 2014 57:9*, vol. 57, no. 9, pp. 1721–1728, Jun. 2014, doi: 10.1007/S11431-014-5583-4.

[51] T. Metz, W. Streule, R. Zengerle, and P. Koltay, “StarTube: A tube with reduced contact line for minimized gas bubble resistance,” *Langmuir*, vol. 24, no. 17, pp. 9204–9206, Sep. 2008, doi: 10.1021/LA801194J/SUPPL\_FILE/LA801194J\_SI\_001.PDF.

[52] J. Luo, L. Qi, Y. Tao, Q. Ma, and C. W. Visser, “Impact-driven ejection of micro metal droplets on-demand,” *Int J Mach Tools Manuf*, vol. 106, pp. 67–74, Jul. 2016, doi: 10.1016/J.IJMACHTOOLS.2016.04.002.

[53] J. Bohandy, B. F. Kim, and F. J. Adrian, “Metal deposition from a supported metal film using an excimer laser,” *J Appl Phys*, vol. 60, no. 4, p. 1538, Jun. 1998, doi: 10.1063/1.337287.

[54] J. Bohandy, B. F. Kim, F. J. Adrian, and A. N. Jette, “Metal deposition at 532 nm using a laser transfer technique,” *J Appl Phys*, vol. 63, no. 4, p. 1158, Aug. 1998, doi: 10.1063/1.340023.

[55] M. Petch, “A new 3D printing technology, interview with Xjet’s Dror Danai - 3D Printing Industry,” 3D Printing Industry. Accessed: Apr. 13, 2022. [Online]. Available: <https://3dprintingindustry.com/news/new-3d-printing-technology->

interview-xjets-drdr-danai-94941/

[56] M. Simonelli *et al.*, “Towards digital metal additive manufacturing via high-temperature drop-on-demand jetting,” *Addit Manuf*, vol. 30, Dec. 2019, doi: 10.1016/j.addma.2019.100930.

[57] N. Gilani, N. T. Aboulkhair, M. Simonelli, M. East, I. Ashcroft, and R. J. M. Hague, “Insights into drop-on-demand metal additive manufacturing through an integrated experimental and computational study,” *Addit Manuf*, vol. 48, Dec. 2021, doi: 10.1016/j.addma.2021.102402.

[58] B. Himmel, D. Rumschoettel, and W. Volk, “Tensile properties of aluminium 4047A built in droplet-based metal printing,” *Rapid Prototyp J*, vol. 25, no. 2, pp. 427–432, Feb. 2019, doi: 10.1108/RPJ-02-2018-0039.

[59] J. Du and Z. Wei, “Numerical analysis of pileup process in metal microdroplet deposition manufacture,” *International Journal of Thermal Sciences*, vol. 96, pp. 35–44, Oct. 2015, doi: 10.1016/J.IJTHERMALSCI.2015.04.016.

[60] A. S. Haselhuhn *et al.*, “Substrate Release Mechanisms for Gas Metal Arc Weld 3D Aluminum Metal Printing,” *3D Print Addit Manuf*, vol. 1, no. 4, pp. 204–209, Dec. 2014, doi: 10.1089/3dp.2014.0015.

[61] V. Sukhotskiy, P. Vishnoi, I. H. Karampelas, S. Vader, Z. Vader, and E. P. Furlani, “Magnetohydrodynamic Drop-on-Demand Liquid Metal Additive Manufacturing: System Overview and Modelling,” Jun. 2018. doi: 10.11159/ffhmt18.155.

[62] J. Luo, L. H. Qi, S. Y. Zhong, J. M. Zhou, and H. J. Li, “Printing solder droplets for micro devices packages using pneumatic

drop-on-demand (DOD) technique,” *J Mater Process Technol*, vol. 212, no. 10, pp. 2066–2073, Oct. 2012, doi: 10.1016/J.JMATPROTEC.2012.05.007.

[63] H. K. Jayant and M. Arora, “Droplet-on-demand metal additive manufacturing using a magnetostrictive actuator,” *J Manuf Process*, vol. 83, pp. 86–96, Nov. 2022, doi: 10.1016/J.JMAPRO.2022.08.012.

[64] H. Li, P. Wang, L. Qi, H. Zuo, S. Zhong, and X. Hou, “3D numerical simulation of successive deposition of uniform molten Al droplets on a moving substrate and experimental validation,” *Comput Mater Sci*, vol. 65, pp. 291–301, Dec. 2012, doi: 10.1016/J.COMMATSCI.2012.07.034.

[65] S. I. Moqadam, L. Mädler, and N. Ellendt, “A High Temperature Drop-On-Demand Droplet Generator for Metallic Melts,” *Micromachines 2019, Vol. 10, Page 477*, vol. 10, no. 7, p. 477, Jul. 2019, doi: 10.3390/MI10070477.

[66] S. Zhong, L. Qi, J. Luo, and Y. Xiao, “Parameters study on generation of uniform copper droplet by Pneumatic Drop-on-Demand technology,” in *Advanced Materials Research*, 2012, pp. 781–784. doi: 10.4028/www.scientific.net/AMR.430-432.781.

[67] S. X. Cheng, T. Li, and S. Chandra, “Producing molten metal droplets with a pneumatic droplet-on-demand generator,” *J Mater Process Technol*, vol. 159, no. 3, pp. 295–302, Feb. 2005, doi: 10.1016/j.jmatprotec.2004.05.016.

[68] J. Luo, W. Wang, W. Xiong, H. Shen, and L. Qi, “Formation of uniform metal traces using alternate droplet printing,” *Int J Mach Tools Manuf*, vol. 122, pp. 47–54, Nov. 2017, doi:

10.1016/j.ijmachtools.2017.05.004.

[69] J. Huang, L. Qi, J. Luo, and X. Hou, “Insights into the impact and solidification of metal droplets in ground-based investigation of droplet deposition 3D printing under microgravity,” *Appl Therm Eng*, vol. 183, p. 116176, Jan. 2021, doi: 10.1016/J.APPLTHERMALENG.2020.116176.

[70] M. Liu, H. Yi, H. Cao, R. Huang, and L. Jia, “Heat accumulation effect in metal droplet-based 3D printing: Evolution mechanism and elimination Strategy,” *Addit Manuf*, vol. 48, p. 102413, Dec. 2021, doi: 10.1016/J.ADDMA.2021.102413.

[71] H. P. Li, H. J. Li, L. H. Qi, J. Luo, and H. S. Zuo, “Simulation on deposition and solidification processes of 7075 Al alloy droplets in 3D printing technology,” *Transactions of Nonferrous Metals Society of China*, vol. 24, no. 6, pp. 1836–1843, Jun. 2014, doi: 10.1016/S1003-6326(14)63261-1.

[72] S. Shakeri and S. Chandra, “Splashing of molten tin droplets on a rough steel surface,” *Int J Heat Mass Transf*, vol. 45, no. 23, pp. 4561–4575, Nov. 2002, doi: 10.1016/S0017-9310(02)00170-9.

[73] B. Gerdes, R. Zengerle, P. Koltay, and L. Riegger, “Direct printing of miniscule aluminum alloy droplets and 3D structures by StarJet technology,” *Journal of Micromechanics and Microengineering*, vol. 28, no. 7, p. 074003, Apr. 2018, doi: 10.1088/1361-6439/AAB928.

[74] H. Yi, L. Qi, J. Luo, and N. Li, “Hole-defects in soluble core assisted aluminum droplet printing: Metallurgical mechanisms and elimination methods,” *Appl Therm Eng*, vol. 148, pp. 1183–1193, Feb. 2019, doi: 10.1016/J.APPLTHERMALENG.2018.12.013.

[75] J. Huang, L. Qi, J. Luo, K. Zhang, and L. Yang, “A ground-based work of droplet deposition manufacturing toward microgravity: Fine pileup of horizontally ejected metal droplets on vertical substrates,” *J Manuf Process*, vol. 66, pp. 293–301, Jun. 2021, doi: 10.1016/J.JMAPRO.2021.03.062.

[76] R. Sun, Y. Shi, Z. Bing, Q. Li, and R. Wang, “Metal transfer and thermal characteristics in drop-on-demand deposition using ultra-high frequency induction heating technology,” *Appl Therm Eng*, vol. 149, pp. 731–744, Feb. 2019, doi: 10.1016/J.APPLTHERMALENG.2018.12.095.

[77] H. Yi, L. Qi, J. Luo, D. Zhang, and N. Li, “Direct fabrication of metal tubes with high-quality inner surfaces via droplet deposition over soluble cores,” *J Mater Process Technol*, vol. 264, pp. 145–154, Feb. 2019, doi: 10.1016/J.JMATPROTEC.2018.09.004.

[78] S. Y. Zhong, L. H. Qi, W. Xiong, J. Luo, and Q. X. Xu, “Research on mechanism of generating aluminum droplets smaller than the nozzle diameter by pneumatic drop-on-demand technology,” *International Journal of Advanced Manufacturing Technology*, vol. 93, no. 5–8, pp. 1771–1780, Nov. 2017, doi: 10.1007/S00170-017-0484-X/METRICS.

[79] J. Huang, L. Qi, J. Luo, L. Zhao, and H. Yi, “Suppression of gravity effects on metal droplet deposition manufacturing by an anti-gravity electric field,” *Int J Mach Tools Manuf*, vol. 148, p. 103474, Jan. 2020, doi: 10.1016/J.IJMACHTOOLS.2019.103474.

[80] H. Yi, L. Qi, J. Luo, D. Zhang, H. Li, and X. Hou, “Effect of the surface morphology of solidified droplet on remelting between neighboring aluminum droplets,” *Int J Mach Tools Manuf*, vol. 130–

131, pp. 1–11, Aug. 2018, doi: 10.1016/j.ijmachtools.2018.03.006.

[81] H. Yi, L. H. Qi, J. Luo, Y. Jiang, and W. Deng, “Pinhole formation from liquid metal microdroplets impact on solid surfaces,” *Appl Phys Lett*, vol. 108, no. 4, Jan. 2016, doi: 10.1063/1.4940404.

[82] Y. P. Chao, L. H. Qi, H. S. Zuo, J. Luo, X. H. Hou, and H. J. Li, “Remelting and bonding of deposited aluminum alloy droplets under different droplet and substrate temperatures in metal droplet deposition manufacture,” *Int J Mach Tools Manuf*, vol. 69, pp. 38–47, Jun. 2013, doi: 10.1016/J.IJMACHTOOLS.2013.03.004.

[83] C. Chen, J. Huang, H. Yi, and Y. Zhang, “Research on the solidified morphologies of successive pileup metal droplets,” *Journal of Mechanical Science and Technology*, vol. 34, no. 8, pp. 3197–3205, Aug. 2020, doi: 10.1007/S12206-020-0711-5/METRICS.

[84] Y. Heichal and S. Chandra, “Predicting thermal contact resistance between molten metal droplets and a solid surface,” *J Heat Transfer*, vol. 127, no. 11, pp. 1269–1275, Nov. 2005, doi: 10.1115/1.2039114.

[85] J. M. Waldvogelt and D. Poulikakoss, “Solidification phenomena in picoliter size solder droplet deposition on a composite substrate,” 1997.

[86] W. Liu, G. X. Wang, and E. F. Matthyst, “Thermal analysis and measurements for a molten metal drop impacting on a substrate : cooling, solidification and heat transfer coefficient,” 1995.

[87] P. Liu, Y. Guo, Y. Wu, J. Chen, and Y. Yang, “A low-cost electrochemical metal 3d printer based on a microfluidic system for printing mesoscale objects,” Apr. 01, 2020, *MDPI AG*. doi: 10.3390/cryst10040257.

[88] A. C. O. Jensen, H. Harboe, A. Brostrøm, K. A. Jensen, and A. S. Fonseca, “Nanoparticle Exposure and Workplace Measurements During Processes Related to 3D Printing of a Metal Object,” *Front Public Health*, vol. 8, Nov. 2020, doi: 10.3389/fpubh.2020.608718.

[89] S. K. Seol, D. Kim, S. Lee, J. H. Kim, W. S. Chang, and J. T. Kim, “Electrodeposition-based 3D Printing of Metallic Microarchitectures with Controlled Internal Structures,” *Small*, vol. 11, no. 32, pp. 3896–3902, Aug. 2015, doi: 10.1002/sml.201500177.

[90] N. Gilani, N. T. Aboulkhair, M. Simonelli, M. East, I. A. Ashcroft, and R. J. M. Hague, “From impact to solidification in drop-on-demand metal additive manufacturing using MetalJet,” *Addit Manuf*, vol. 55, p. 102827, Jul. 2022, doi: 10.1016/J.ADDMA.2022.102827.

[91] D. Attinger, Z. Zhao, and D. Poulikakos, “An Experimental Study of Molten Microdroplet Surface Deposition and Solidification: Transient Behavior and Wetting Angle Dynamics,” *J Heat Transfer*, vol. 122, no. 3, pp. 544–556, Aug. 2000, doi: 10.1115/1.1287587.

[92] M. Pasandideh-Fard, Y. M. Qiao, S. Chandra, and J. Mostaghimi, “Capillary effects during droplet impact on a solid surface,” *Physics of Fluids*, vol. 8, no. 3, pp. 650–659, 1996, doi: 10.1063/1.868850.

[93] A. Bejan and D. Gobin, “Constructal theory of droplet impact geometry,” *Int J Heat Mass Transf*, vol. 49, no. 15–16, pp. 2412–2419, Jul. 2006, doi: 10.1016/j.ijheatmasstransfer.2006.02.001.

[94] Chr. Mundo, M. Sommerfeld, and C. Tropea, “Droplet-wall collisions: Experimental studies of the deformation and breakup

process,” *International Journal of Multiphase Flow*, vol. 21, no. 2, pp. 151–173, Apr. 1995, doi: 10.1016/0301-9322(94)00069-V.

[95] D. C. Vadillo, A. Soucemarianadin, C. Delattre, and D. C. D. Roux, “Dynamic contact angle effects onto the maximum drop impact spreading on solid surfaces,” *Physics of Fluids*, vol. 21, no. 12, pp. 1–8, 2009, doi: 10.1063/1.3276259.

[96] R. G. Azar, Z. Yang, S. Chandra, and J. Mostaghimi, “Impact of molten metal droplets on the tip of a pin projecting from a flat surface,” *Int J Heat Fluid Flow*, vol. 26, no. 2, pp. 334–347, Apr. 2005, doi: 10.1016/j.ijheatfluidflow.2004.08.004.

[97] D. Zhang, L. Qi, J. Luo, H. Yi, W. Xiong, and Y. Mo, “Parametric mapping of linear deposition morphology in uniform metal droplet deposition technique,” *J Mater Process Technol*, vol. 264, pp. 234–239, Feb. 2019, doi: 10.1016/J.JMATPROTEC.2018.08.048.

[98] V. Butty, D. Poulikakos, and J. Giannakouros, “Three-dimensional presolidification heat transfer and fluid dynamics in molten microdroplet deposition,” *Int J Heat Fluid Flow*, vol. 23, no. 3, pp. 232–241, Jun. 2002, doi: 10.1016/S0142-727X(02)00171-6.

[99] C. Tang *et al.*, “Dynamics of droplet impact on solid surface with different roughness,” *International Journal of Multiphase Flow*, vol. 96, pp. 56–69, Nov. 2017, doi: 10.1016/J.IJMULTIPHASEFLOW.2017.07.002.

[100] S. D. Aziz and S. Chandra, “Impact, recoil and splashing of molten metal droplets,” *Int J Heat Mass Transf*, vol. 43, no. 16, pp. 2841–2857, Aug. 2000, doi: 10.1016/S0017-9310(99)00350-6.

[101] M. Pasandideh-Fard, R. Bhola, S. Chandra, and J. Mostaghimi, “Deposition of tin droplets on a steel plate: simulations

and experiments,” *Int J Heat Mass Transf*, vol. 41, no. 19, pp. 2929–2945, Oct. 1998, doi: 10.1016/S0017-9310(98)00023-4.

[102] N. Z. Mehdizadeh, M. Raessi, S. Chandra, and J. Mostaghimi, “Effect of substrate temperature on splashing molten tin droplets,” *J Heat Transfer*, vol. 126, no. 3, pp. 445–452, Jun. 2004, doi: 10.1115/1.1737778.

[103] W. Yang, R. Yang, Y. Yao, Z. Gao, and H. Zhang, “Effects of surface oxide layer on the impact dynamic behavior of molten aluminum droplets,” *Physics of Fluids*, vol. 35, no. 1, Jan. 2023, doi: 10.1063/5.0136117.

[104] W. H. Walton and W. C. Prewett, “The Production of Sprays and Mists of Uniform Drop Size by Means of Spinning Disc Type Sprayers,” *Proceedings of the Physical Society. Section B*, vol. 62, no. 6, pp. 341–350, Jun. 1949, doi: 10.1088/0370-1301/62/6/301.

[105] T. Bennett and D. Poulikakos, “Splat-quench solidification: estimating the maximum spreading of a droplet impacting a solid surface,” *J Mater Sci*, vol. 28, no. 4, pp. 963–970, Feb. 1993, doi: 10.1007/BF00400880.

[106] H. Jones, “Cooling, freezing and substrate impact of droplets formed by rotary atomization,” *J Phys D Appl Phys*, vol. 4, no. 11, p. 206, Nov. 1971, doi: 10.1088/0022-3727/4/11/206.

[107] E. W. Collings, A. J. Markworth, J. K. McCoy, and J. H. Saunders, “Splat-quench solidification of freely falling liquid-metal drops by impact on a planar substrate,” *J Mater Sci*, vol. 25, no. 8, pp. 3677–3682, Aug. 1990, doi: 10.1007/BF00575404.

[108] J. Madejski, “Solidification of droplets on a cold surface,” *Int J Heat Mass Transf*, vol. 19, no. 9, pp. 1009–1013, Sep. 1976, doi:

10.1016/0017-9310(76)90183-6.

[109] R. McGuan, R. N. Candler, and H. P. Kavehpour, “Spreading and contact-line arrest dynamics of impacting oxidized liquid-metal droplets,” *Phys Rev Fluids*, vol. 6, no. 11, p. L111601, Nov. 2021, doi: 10.1103/PHYSREVFLUIDS.6.L111601/FIGURES/6/MEDIUM.

[110] C. Tang *et al.*, “Dynamics of droplet impact on solid surface with different roughness,” *International Journal of Multiphase Flow*, vol. 96, pp. 56–69, 2017, doi: 10.1016/j.ijmultiphaseflow.2017.07.002.

[111] R. Rioboo, C. Tropea, and M. Marengo, “OUTCOMES FROM A DROP IMPACT ON SOLID SURFACES,” *Atomization and Sprays*, vol. 11, no. 2, p. 12, 2001, doi: 10.1615/AtomizSpr.v11.i2.40.

[112] I. V. Roisman, A. Lembach, and C. Tropea, “Drop splashing induced by target roughness and porosity: The size plays no role,” *Adv Colloid Interface Sci*, vol. 222, pp. 615–621, Aug. 2015, doi: 10.1016/J.CIS.2015.02.004.

[113] C. Wang, A. Janssen, A. Prakash, R. Cracknell, and H. Xu, “Splash blended ethanol in a spark ignition engine – Effect of RON, octane sensitivity and charge cooling,” *Fuel*, vol. 196, pp. 21–31, May 2017, doi: 10.1016/J.FUEL.2017.01.075.

[114] H. yu Zhang *et al.*, “Splash involved deposition behavior and erosion mechanism of long laminar plasma sprayed NiCrBSi coatings,” *Surf Coat Technol*, vol. 395, p. 125939, Aug. 2020, doi: 10.1016/J.SURFCOAT.2020.125939.

[115] C. Escure, M. Vardelle, and P. Fauchais, “Experimental and Theoretical Study of the Impact of Alumina Droplets on Cold and

Hot Substrates,” *Plasma Chemistry and Plasma Processing*, vol. 23, no. 2, pp. 185–221, Jun. 2003, doi: 10.1023/A:1022976914185/METRICS.

[116] G. Lavergne and B. Platet, “Study of the impact of droplets on a heated wall (in French),” *Nbl/2401/CERT/DERMES*, 1991.

[117] C. D. Stow, M. G. Hadfield, and J. M. Ziman, “An experimental investigation of fluid flow resulting from the impact of a water drop with an unyielding dry surface,” *Proceedings of the Royal Society of London. A. Mathematical and Physical Sciences*, vol. 373, no. 1755, pp. 419–441, 1981, doi: 10.1098/rspa.1981.0002.

[118] G. E. Cossali, A. Coghe, and M. Marengo, “The impact of a single drop on a wetted solid surface,” *Exp Fluids*, vol. 22, no. 6, pp. 463–472, 1997, doi: 10.1007/S003480050073.

[119] K. Range and F. Feuillebois, “Influence of Surface Roughness on Liquid Drop Impact,” *J Colloid Interface Sci*, vol. 203, no. 1, pp. 16–30, Jul. 1998, doi: 10.1006/JCIS.1998.5518.

[120] S. Lin, L. Zhou, B. Liu, Q. Xu, L. Chen, and Z. Li, “The roles of surface temperature and roughness in droplet splashing,” *Int J Heat Mass Transf*, vol. 220, Mar. 2024, doi: 10.1016/j.ijheatmasstransfer.2023.124959.

[121] J. Hao, “Effect of surface roughness on droplet splashing,” *Physics of Fluids*, vol. 29, no. 12, Dec. 2017, doi: 10.1063/1.5005990.

[122] T. De Goede, K. De Bruin, N. Shahidzadeh, and D. Bonn, “Droplet splashing on rough surfaces,” *Phys Rev Fluids*, vol. 6, no. 4, Apr. 2021, doi: 10.1103/PhysRevFluids.6.043604.

[123] T. Young, “III. An essay on the cohesion of fluids,” *Philos Trans R Soc Lond*, vol. 95, pp. 65–87, Dec. 1805, doi:

10.1098/rstl.1805.0005.

[124] J. Wang, Y. Wu, Y. Cao, G. Li, and Y. Liao, “Influence of surface roughness on contact angle hysteresis and spreading work”, doi: 10.1007/s00396-020-04680-x/Published.

[125] J. W. Song and L. W. Fan, “Understanding the effects of surface roughness on the temperature and pressure relevancy of water contact angles,” *Colloids Surf A Physicochem Eng Asp*, vol. 656, Jan. 2023, doi: 10.1016/j.colsurfa.2022.130391.

[126] J. W. Song and L. W. Fan, “Temperature dependence of the contact angle of water: A review of research progress, theoretical understanding, and implications for boiling heat transfer,” *Adv Colloid Interface Sci*, vol. 288, p. 102339, Feb. 2021, doi: 10.1016/J.CIS.2020.102339.

[127] J. D. Bernardin, I. Mudawar, C. B. Walsh, and E. I. Franses, “Contact angle temperature dependence for water droplets on practical aluminum surfaces,” *Int J Heat Mass Transf*, vol. 40, no. 5, pp. 1017–1033, Mar. 1997, doi: 10.1016/0017-9310(96)00184-6.

[128] V. Vaikuntanathan and D. Sivakumar, “Transition from Cassie to impaled state during drop impact on groove-textured solid surfaces,” *Soft Matter*, vol. 10, no. 17, pp. 2991–3002, May 2014, doi: 10.1039/c4sm00050a.

[129] S. Bao, K. Tang, A. Kvithyld, T. Engh, and M. Tangstad, “Wetting of pure aluminium on graphite, SiC and Al<sub>2</sub>O<sub>3</sub> in aluminium filtration,” *Transactions of Nonferrous Metals Society of China (English Edition)*, vol. 22, no. 8, pp. 1930–1938, 2012, doi: 10.1016/S1003-6326(11)61410-6.

[130] K. C. Mills and Y. C. Su, “Review of surface tension data

for metallic elements and alloys: Part 1 – Pure metals,” *International Materials Reviews*, vol. 51, no. 6, pp. 329–351, Dec. 2006, doi: 10.1179/174328006X102510.

[131] N. Eustathopoulos, M.G. Nicholas, and B. D. M.G. Nicholas, *Wettability at High Temperatures* -, 1st ed. Elsevier, 1999.

[132] S. TAKEMATSU, T. MIZUGUCHI, H. NAKASHIMA, K. IKEDA, and H. ABE, “Evaluation of Surface Energy by Molecular Dynamics Simulation and Discussion about Cleavage Fracture in .ALPHA.-Al<sub>2</sub>O<sub>3</sub>,” *Journal of the Ceramic Society of Japan*, vol. 112, no. 1301, pp. 46–49, 2004, doi: 10.2109/jcersj.112.46.

[133] L. A. Girifalco and R. J. Good, “A Theory for the Estimation of Surface and Interfacial Energies. I. Derivation and Application to Interfacial Tension,” *J Phys Chem*, vol. 61, no. 7, pp. 904–909, Jul. 1957, doi: 10.1021/j150553a013.

[134] P. Nikolopoulos, S. Agathopoulos, and A. Tsoga, “A method for the calculation of interfacial energies in Al<sub>2</sub>O<sub>3</sub> and ZrO<sub>2</sub>/liquid-metal and liquid-alloy systems,” *J Mater Sci*, vol. 29, no. 16, pp. 4393–4398, Jan. 1994, doi: 10.1007/BF00414227/METRICS.

[135] R. Li, N. Ashgriz, S. Chandra, and J. R. Andrews, “Solidification contact angles of molten droplets deposited on solid surfaces,” in *Journal of Materials Science*, Dec. 2007, pp. 9511–9523. doi: 10.1007/s10853-007-1757-9.

[136] J. Venkatesan, S. Rajasekaran, A. Das, and S. Ganesan, “Effects of temperature-dependent contact angle on the flow dynamics of an impinging droplet on a hot solid substrate,” *Int J Heat Fluid Flow*, vol. 62, pp. 282–298, Dec. 2016, doi: 10.1016/J.IJHEATFLUIDFLOW.2016.10.003.

[137] F. Villa, M. Marengo, and J. De Coninck, “A new model to predict the influence of surface temperature on contact angle,” *Sci Rep*, vol. 8, no. 1, Dec. 2018, doi: 10.1038/s41598-018-24828-8.

[138] S. Zhang *et al.*, “Investigation of Al droplet wetting behavior on highly-oriented SiC,” *RSC Adv*, vol. 13, no. 38, p. 26869, Sep. 2023, doi: 10.1039/D3RA03335J.

[139] R. N. Wenzel, “RESISTANCE OF SOLID SURFACES TO WETTING BY WATER,” *Ind Eng Chem*, vol. 28, no. 8, pp. 988–994, Aug. 1936, doi: 10.1021/ie50320a024.

[140] A. B. D. Cassie and S. Baxter, “Wettability of porous surfaces,” *Transactions of the Faraday Society*, vol. 40, p. 546, 1944, doi: 10.1039/tf94444000546.

[141] M. S. Bell and A. Borhan, “A Volume-Corrected Wenzel Model,” *ACS Omega*, vol. 5, no. 15, pp. 8875–8884, Apr. 2020, doi: 10.1021/ACSOMEGA.0C00495/SUPPL\_FILE/AO0C00495\_SI\_002.ZIP.

[142] W. Xiong and P. Cheng, “Mesoscale simulation of a molten droplet impacting and solidifying on a cold rough substrate,” *International Communications in Heat and Mass Transfer*, vol. 98, pp. 248–257, Nov. 2018, doi: 10.1016/J.ICHEATMASSTRANSFER.2018.09.001.

[143] M. A. Quetzeri-Santiago, A. A. Castrejón-Pita, and J. R. Castrejón-Pita, “The Effect of Surface Roughness on the Contact Line and Splashing Dynamics of Impacting Droplets,” *Scientific Reports 2019 9:1*, vol. 9, no. 1, pp. 1–10, Oct. 2019, doi: 10.1038/s41598-019-51490-5.

[144] Z. QI, L. LIAO, R. yue WANG, Y. gang ZHANG, and Z.

fu YUAN, “Roughness-dependent wetting and surface tension of molten lead on alumina,” *Transactions of Nonferrous Metals Society of China (English Edition)*, vol. 31, no. 8, pp. 2511–2521, Aug. 2021, doi: 10.1016/S1003-6326(21)65671-6.

[145] D. A. Champion, B. D. Keene, and . M Sillwood, “Wetting of Aluminium Oxide by Molten Aluminium and Other Metals,” 1969.

[146] S. W. Ip, M. Kucharski, and J. M. Toguri, “Wetting behaviour of aluminium and aluminium alloys on Al<sub>2</sub>O<sub>3</sub> and CaO,” *J Mater Sci Lett*, vol. 12, no. 21, pp. 1699–1702, 1993, doi: 10.1007/BF00418836.

[147] Q. Lin, F. Li, P. Jin, and W. Zhong, “Wetting of T2 Cu by molten 4043 and 6061 Al alloys at 923–1023 K,” *J Alloys Compd*, vol. 734, pp. 144–151, Feb. 2018, doi: 10.1016/j.jallcom.2017.11.026.

[148] Q. Lin, P. Jin, R. Cao, and J. Chen, “Reactive wetting of low carbon steel by Al 4043 and 6061 alloys at 600-750 °C,” *Surf Coat Technol*, vol. 302, pp. 166–172, Sep. 2016, doi: 10.1016/j.surfcoat.2016.06.005.

[149] H. cheng LIAO, Y. GAO, Q. gui WANG, and D. WILSON, “Development of viscosity model for aluminum alloys using BP neural network,” *Transactions of Nonferrous Metals Society of China (English Edition)*, vol. 31, no. 10, pp. 2978–2985, Oct. 2021, doi: 10.1016/S1003-6326(21)65707-2.

[150] N. Srivastava and G. P. Chaudhari, “Strengthening in Al alloy nano composites fabricated by ultrasound assisted solidification technique,” *Materials Science and Engineering: A*, vol. 651, pp. 241–247, Jan. 2016, doi: 10.1016/J.MSEA.2015.10.118.

[151] D. Sparks *et al.*, “Dynamic and kinematic viscosity

measurements with a resonating microtube,” *Sens Actuators A Phys*, vol. 149, no. 1, pp. 38–41, Jan. 2009, doi: 10.1016/J.SNA.2008.09.013.

[152] “Understanding TP2, T2, TU1 Copper Tubes - Ningbo Jintian Copper (Group) Co., Ltd.” Accessed: Mar. 31, 2025. [Online]. Available: <https://jtcopper.com/understanding-tp2-t2-tu1-copper-tubes-provided-by-the-customer-with-one-article.html>

## Chapter 7 Appendix

Appendix 1: A brief review of the articles which study the spreading factor of different metal droplets

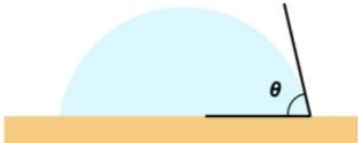
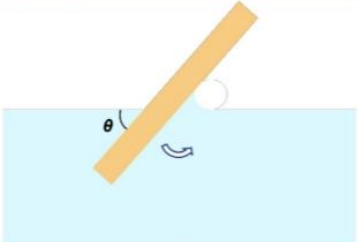
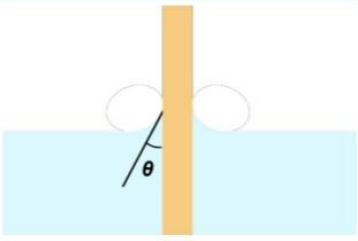
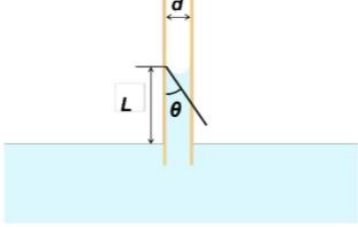
	Material	Substrate	Method or Expression
<b>Attinge et al.</b> [91] (2018)	Solder	Wafer slide	$\beta$ was measured by the image analysis
<b>Aziz and Chandra</b> [100] (2000)	Tin	Stainless steel	$\xi_{max} = \frac{D_{max}}{D} = \sqrt{\frac{We+12}{\frac{8}{3}We s^* + 3(1-\cos \beta_a) + 4\frac{We}{\sqrt{Re}}}}$ $\xi_{max} = \sqrt{\frac{We+12}{3(1-\cos \theta_a) + 4\left(\frac{We}{\sqrt{Re}}\right)}}$ when there is isothermal droplet impact $\xi_{max} = \frac{D_{max}}{D} = \sqrt{\frac{We+12}{We Ste \sqrt{\frac{3\gamma_w}{2\pi Pe \gamma_d}} + 3(1-\cos \beta_a) + 4\frac{We}{\sqrt{Re}}}}$ when consider the growing thickness of the solidified layer $\xi_{max} = \frac{Re^{1/4}}{2}$ when $\frac{We}{\sqrt{Re}} \gg 1$ and if $We \gg 12$
<b>Zhang et al.</b> [97] (2019)	Sn63Pb37 AlSi12	Copper	$\eta = \frac{D_{max}}{D} = \sqrt{\frac{We+12}{\frac{8}{3}We s^* + 3(1-\cos \beta_a) + 4\frac{We}{\sqrt{Re}}}}$ where "s*" is dimensionless solidification thickness of solid layer,
<b>Gilan et al.</b> [90] (2022)	Sn	Cu Zn Sn	$S_{max} = D_{max}/D_0$ by measuring each droplet after the experiment

---

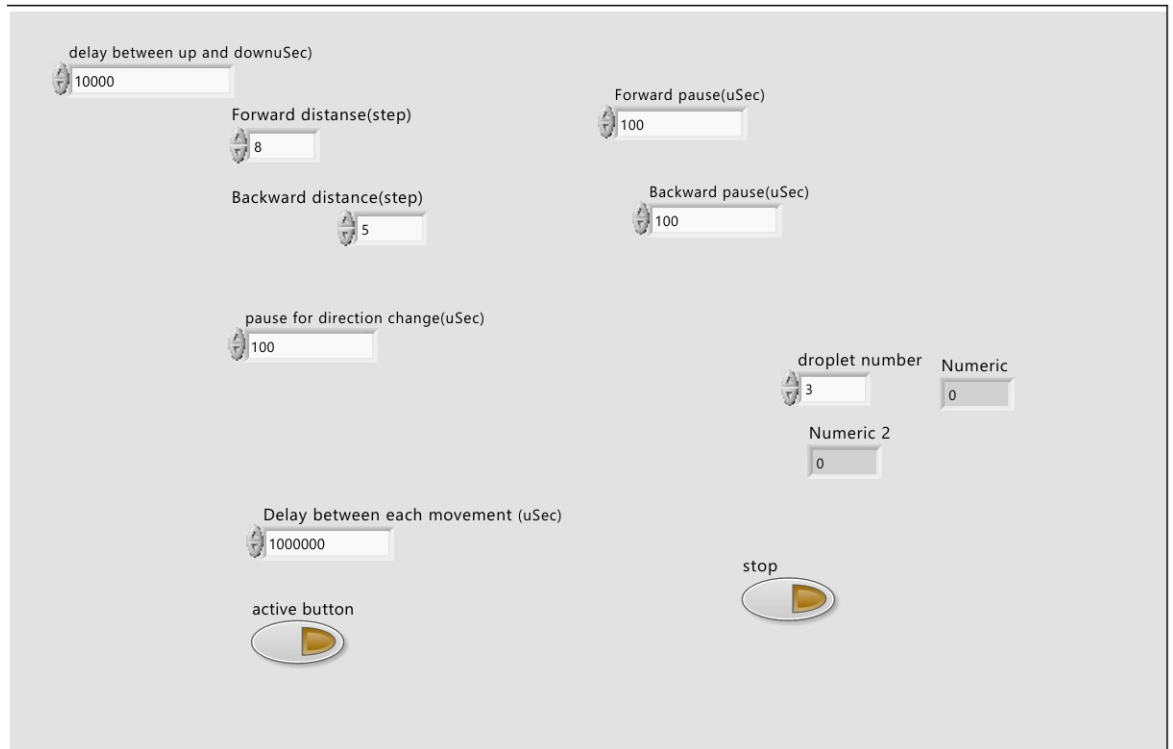
<b>Yang et al.</b> [103] (2023)	Aluminum	Polytetrafluoroethylene (Teflon)	Pasandideh-Fard model: $\xi_{max} = \frac{D_{max}}{D} =$
			$\sqrt{\frac{We+12}{3(1-\cos\theta_a)+4\left(\frac{We}{\sqrt{Re}}\right)}} \text{ or } \xi_{max} \sim Re^{1/4} \text{ or } \xi_{max} \sim V^{1/4}$
			when $We \gg \sqrt{Re}$ and if $We \gg 12$ ;
			Ryan model: $\xi_{max} \sim We^{1/2}$ or $\xi_{max} \sim V$ compared with experimental results

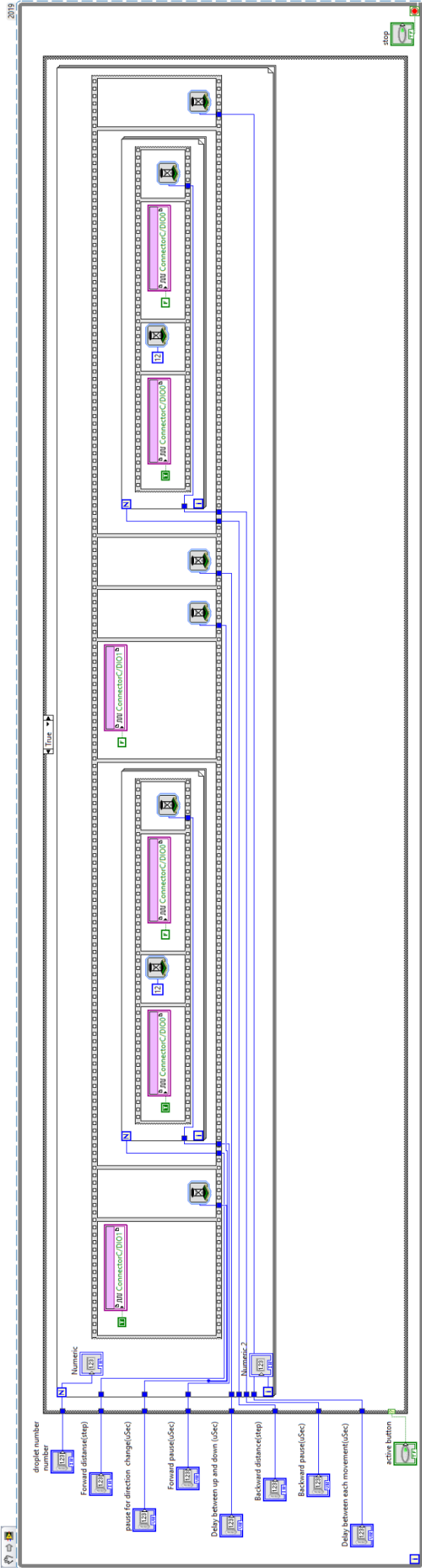
---

Appendix 2: The method to measure the contact angles from Song and Fan [126]

No.	Category	Method	Schematic	Descriptions
1	Direct	Sessile drop		Based on optical imaging techniques, the contact angle is directly determined by measuring the tangent angle at the tri-phase contact point of a sessile drop contour and a solid surface.
2		Captive bubble		In addition to depositing a sessile drop on the solid surface, instead, a gas bubble is captive beneath the solid surface. The contact angle at the intersection of the three interfaces is also directly measured according to the bubble profile.
3		Tilting plate		In this method, one end of a rectangle solid plate is fixed above the test liquid, while the other end is rotated toward the liquid surface until it is immersed in the liquid, which will form two menisci on both sides of the plate. Then the solid plate continues slowly rotating until one of the menisci becomes horizontal. Then the angle between the solid surface and the liquid surface is the corresponding contact angle.
4	Indirect	Wilhelmy balance		When a thin, smooth, and vertical solid plate is immersed in a probe liquid, the contact angle can be calculated by measuring force change, $F$ . The equation is $F = p\gamma_{lv}\cos\theta - V\Delta\rho g$ , where $p$ , $V$ , $\Delta\rho$ , and $g$ are the perimeter of the plate, the volume of the displaced liquid, the difference in the density between the liquid and vapor, and the acceleration of gravity, respectively.
5		Capillary rise		Similarly, a capillary tube with a small enough diameter, $d$ , contacts with a probe liquid. The meniscus confined in the tube can be considered to be spherical. The contact angle can be calculated from measuring the capillary height, $L$ , based on the equation, $\sin\theta = 1 - \Delta\rho g L^2 / 2\gamma_{lv}$ .

Appendix 3: The LabView program to control the printhead





Appendix 4: G code example for the 3D moving platform

G01 X-55 Y-50 Z28 F1500

G4 P10

G01 X-35 F2000

G4 P2

G01 X-30 F2000

G4 P2

G01 X-25 F2000

G4 P2

G01 X-20 F2000

G4 P2

G01 X-15 F2000

G4 P2

G01 X-10 F2000

G4 P2

G01 X-5 F2000

G4 P2

G01 X0 F2000

G4 P2

G01 X5 F2000

G4 P2

G01 X10 F2000

G4 P2

G01 X25 Y-40 F2000

G01 Z0 F1500

G4 P1

M2